

Electronic spectroscopy of cold ions in a radio-frequency trap

Inauguraldissertation

zur

Erlangung der Würde eines Doktors der Philosophie

vorgelegt der

Philosophisch-Naturwissenschaftlichen Fakultät

der Universität Basel

von

Vitaly S. Rudnev

aus Lesozavodsk, Russland

Basel, 2010

Genehmigt von der Philosophisch-Naturwissenschaftlichen Fakultät

auf Antrag von

Prof. Dr. John P. Maier und Prof. Dr. Stefan Willitsch

Basel, den 30.03.2010

Prof. Dr. Eberhard Parlow

Dekan

To my mother

Acknowledgments

I am grateful to Professor Dr. John P. Maier for providing me with excellent experimental instruments and financial support to carry out this PhD effort. I would like to thank Prof. Dr. Stefan Willitsch for his agreement to be my co-referee. Your critical review concerning my thesis was exceptionally helpful and taken into deep consideration.

During my PhD studies I had a pleasure to work with a great deal of brilliant people. Dr. Dmitry Khoroshev introduced me to the group and guided me in the completely foreign country at the beginning. Many thanks go to Dr. Anatoly Johnson who presented for me the world of ion traps and electronic spectroscopy. Dr. Anton Batalov, Dr. Alexey Denisov, Dr. Egor Chasovskikh, Dr. Ivan Shnitko and Dr. Andrey Boguslavskiy were the great opponents and referees during many interesting and heated discussions. I would also like to thank Ivana Petkovic, your support inspired me during my writing time and ceased me of a chance to give up.

I am greatly thankful to Prof. Dieter Gerlich for valuable remarks concerning rf-devices. Thanks to Dr. Fabio J. Mazzotti who introduced to me the world of ab-initio calculations. I kindly thank Dr. Ramya Nagarajan and Dr. Corey A. Rice for sharing their deep knowledge, continuous willingness to help and for critical advices. I am grateful to Dr. Marek Tulej for our talks. Satrajit Chakrabarty and Dr. Rainer Dietsche are thanked for their help during the long hours in lab. My appreciations are addressed to all former and present group fellows.

This work could not be done without help of Dieter Wild, Grischa Martin from the mechanical workshop. Georg Holderied and his excellent knowledge of the electronics were truly irreplaceable; Jacques Lecoultre is thanked for synthesizing the necessary chemicals. I am deeply thankful to Ester Stalder, Daniela Tischhauser and Maya Greuter from secretary office for taking care of bureaucratic matters and making my life easier in foreign county. And finally, I'd like to address my thanks to the city of Basel.

Vitaly

TABLE OF CONTENTS

CHAPTER 1	INTRODUCTION.....	8
1.1	Interstellar medium.....	8
1.2	Diffuse interstellar bands.....	14
CHAPTER 2	THEORY OF LINEAR RF TRAPS.....	16
2.1	Adiabatic approximation and effective potential.....	16
2.1.1	Laplace equation for electrostatics.....	18
2.1.2	Safe operating conditions.....	20
2.1.3	Space-charge limit in adiabatic approximation.....	21
2.2	Oscillating quadrupole field.....	22
2.3	Ion temperature and phase space density.....	29
2.3.1	Liouville's theorem.....	29
2.3.2	Action diagrams, emittance and acceptance.....	30
2.3.3	Time evolution of action diagrams.....	32
2.3.4	Ion temperature and ion cloud.....	34
2.3.5	RF heating of macromotion.....	36
2.4	Inelastic collision of two particles.....	38
2.4.1	Relative speed between an ion and buffer gas, HS1 model.....	38
2.4.2	Probability of a collision.....	39
2.4.3	Collision of two bodies.....	39
2.5	Ion mobility.....	42
CHAPTER 3	ELECTRONIC SPECTROSCOPY.....	44
3.1	Electronic spectroscopy (Born-Openheimer approximation)	44
3.2	Vibration.....	45

3.3	Rotation.....	45
3.3.1	Linear molecules.....	46
3.3.2	Symmetric tops.....	47
3.3.3	Asymmetric tops.....	49
CHAPTER 4	EXPERIMENTAL SETUP.....	51
4.1	First chamber (Source chamber).....	52
4.1.1	Electron impact ion source.....	53
4.1.2	Magnetic bender.....	56
4.1.3	Hexapole.....	57
4.2	Second chamber (Mass filter).....	58
4.3	Third chamber (22- pole ion trap).....	59
4.3.1	22-pole ion trap.....	60
4.3.2	Cryostat.....	61
4.3.3	Pulsed valve.....	62
4.4	Fourth chamber (Mass filter).....	62
4.5	Fifth chamber (Daly detector).....	63
CHAPTER 5	ORGANIZATION OF EXPERIMENT.....	65
5.1	Automation of experiment.....	65
5.2	Laser beam alignment.....	68
5.3	Photofragmentation experiments.....	69
CHAPTER 6	RESULTS AND DISCUSSION.....	72
6.1	1_0^2 band of $A^2\Sigma^+ \leftarrow X^2\Pi_{3/2}$ transition , N_2O^+	72
6.2	Electronic transitions of polyacetylene cations.....	74
6.2.1	Introduction.....	74
6.2.2	Motivation.....	74
6.2.3	Experimental.....	79

6.2.4	$A^2\Pi_g - X^2\Pi_u$ transition of $C_{10}H_2^+$	80
6.2.5	$E^2\Pi_g - X^2\Pi_u$ transition of $C_{10}H_2^+$	83
6.2.6	$B^2\Pi_g - X^2\Pi_u$ transition of $C_{10}H_2^+$	85
6.2.7	Origin bands of electronic transitions: $C^2\Pi_g - X^2\Pi_u$ ($C_{10}H_2^+$), $B^2\Pi_g - X^2\Pi_u$ ($C_8H_2^+$) and $D^2\Pi_g - X^2\Pi_u$ ($C_{12}H_2^+$)	86
6.2.8	$C^2\Pi_g - X^2\Pi_u$ transition of $C_8H_2^+$	87
6.2.9	Cooling dynamics.....	88
6.2.10	Conclusion.....	90
6.3	$C_4H_3Cl^+$ cation.....	93
6.3.1	Rotational analysis.....	95
6.4	Anthracene and naphthalene radical cations.....	100
6.5	$B^2\Sigma_u^+ \leftarrow X^2\Pi_g$ electronic spectrum of $NCCN^+$ in the gas phase.....	105
6.6	$D^2\Pi_u, C^2\Pi_u \leftarrow X^2\Pi_g$ Electronic Transitions of $NCCN^+$	110
CONSLUSIONS.....		115
 APPENDIX		
	Time delay generator based on PCI-CTR20HD card.....	117
BIBLIOGRAPHY.....		121
	Curriculum vitae.....	129

CHAPTER 1

Introduction

1.1 Interstellar medium

Basically, direct ways of interstellar investigation are limited by our solar system. Some attempts to analyze the surfaces of Mars, Venus, and Moon were undertaken and others are still in progress [1]. However, the most powerful methods of investigation are given by spectroscopic measurements of space. To understand processes going on in the interstellar medium, one should think about a physical model of the evolution of the universe and model possible chemical reactions occurring in space. Knowledge of these models allows experiments on specific molecules of interest to be designed. A comparison of spectroscopic data from space and laboratories give insight into which molecules can exist in the interstellar medium. Obtained data are used to make cosmological models more exact [2].

According to modern cosmology theory the observed universe appeared 13.73 billions years ago from the beginning „singular“ state with a temperature about 10^{32} K (Planck temperature) and a density of approximately $10^{96} \text{ kg} \cdot \text{m}^{-3}$ (Planck density) and from that time the universe permanently expanded and cooled down [3]. The early universe was uniform and isotropic with the unusual energy density, temperature and pressure. As a result of expansion and cooling, the universe passed through several phase transitions. Approximately 380 000 years after the Big Bang, the universe consisted mainly of two particles, helium and hydrogen. These two elements are still the most abundant elements in the interstellar medium (*Figure 1.1.1*) [1]. All particles heavier than helium are produced in stars which can be named the factories of material.

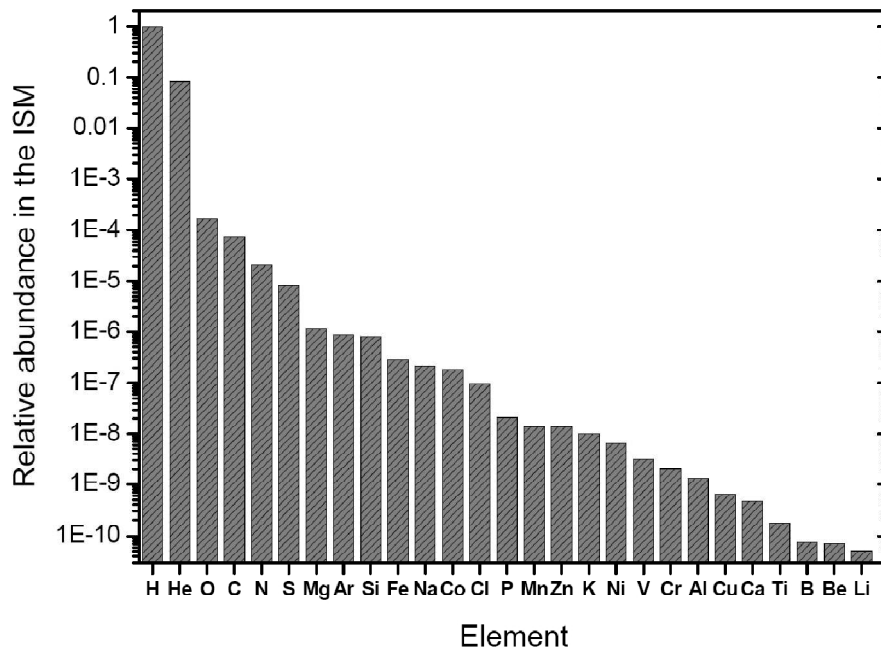


Figure 1.1.I. Relative abundances of elements in ISM.

Interstellar gas and stars coexist in a dynamical equilibrium. Stars condense from a rotating collapsing cloud of dust and gas with a density of about 10^4 atoms or molecules per cm^3 and a temperature of 10–50 K. The elements heavier than helium were formed in the stars of previous generations. The collapse of a cloud is initiated perhaps by a shock wave emanating from a nearby supernova explosion. The original mass of a cloud must be thousands of solar masses to exceed the *Jeans mass*. The condensation of gas into a star is accompanied by a considerable temperature increase and continues until the balance between the gravitational attraction and the hot gas pressure is reached. All our information about the physical properties of stars comes more or less directly from studies of the stellar spectral signatures. Stellar classification is based on spectral characteristics and physically, the classes indicate the temperature of the star's atmosphere [4-5]. In Figure 1.1.II the Harvard classification system is depicted with decreasing temperature towards the left.

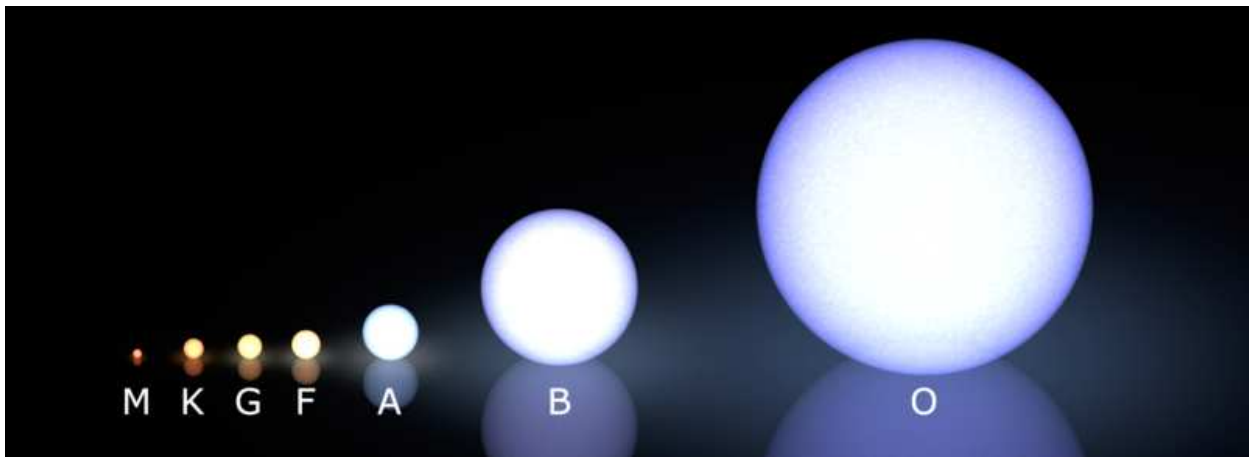


Figure 1.1.II. Illustration to the stellar classification system.

There are additional notations where Q is for novae, P for planetary nebulae and W for Wolf-Rayet stars. The class C consists of the earlier types R and N. The spectral classes C and S differ with respect to surface chemical composition and represent parallel branches to types G–M. The recent additions are spectral classes L and T, representing *brown dwarfs* and continuing the sequence beyond M. Spectral classes are divided into subclasses denoted by the numbers 0 . . . 9. The characteristics of stars depend on the classes presented:

Class O - Blue stars, with surface temperatures in the range of 20 000–35 000 K. Spectrum contains lines from multiply ionized atoms, e.g. HeII, CIII, NIII, OIII, SiV. HeI visible, HI lines weak.

Class B - Blue-white stars, surface temperature is about 15 000 K. HeI (403 nm) lines are strongest at B2, then get weaker and have disappeared at type B9. The K line of CaII becomes visible at type B3. HI lines getting stronger. OII, SiII and MgII lines are visible.

Class A - White stars, surface temperature is about 9000 K. The HI lines are very strong at A0 and dominate the whole spectrum, then get weaker. H and K lines of CaII are getting stronger. Neutral metal lines begin to appear.

Class F - Yellow-white stars, surface temperature is about 7000 K. HI lines are getting weaker, H and K of CaII getting stronger. Spectrum contains many metal lines, e. g. FeI, FeII, CrII, TiII.

Class G - Yellow stars (Sun), surface temperature is about 5500 K. The HI lines are weak, H and K lines are very strong. Metal lines are getting stronger.

Class K - Orange-yellow stars, surface temperature is about 4000 K. Spectrum dominated by metal lines. HI lines are insignificant. CaI 422.7 nm is clearly visible.

Class M - Red stars, surface temperature is about 3000 K. TiO bands are getting stronger. CaI 422.7 nm band is very strong. There are many neutral metal lines.

Class L - Brown (dark red) stars, surface temperature is about 2000 K. The TiO and VO bands disappear for early L class. Spectrum contains very strong and broad lines of NaI and KI.

Class T - Brown dwarfs, surface temperature is about 1000 K. Spectrum contains very strong molecular absorption bands of CH₄ and H₂O.

Class C - Carbon stars, previously R and N. Very red stars, surface temperature is about 3000 K. There are strong molecular bands, e. g. C₂, CN and CH. TiO bands do not exist. Line spectrum is similar to the types K and M.

Class S - Surface temperature is about 3000 K. There are very clear ZrO bands. Also other molecular bands, e. g. YO, LaO and TiO can be present.

Some stars have spectra which are not the same as their spectral basis differing in temperature and luminosity. These stars are called *peculiar*.

In 1867 Wolf - Rayet stars were discovered by *C. Wolf* and *G. Rayet*. The surface of these stars is very hot and many of them are members of binary star systems.

There are additional classifications for the O and B stars which have weak emission component of the hydrogen absorption lines either at the line centre or in its wings. These stars are called *Be* and *shell stars*. The emission lines are formed in a rotationally flattened gas shell around the star. The *shell* and *Be* stars spectra present irregular variations which is related to structural changes in their shell.

PCygni star spectra have the strongest emission lines with one or more sharp absorption lines on the short wavelength side of the emission line.

The peculiar *A* stars or *Ap* stars are usually strongly magnetic stars with lines split into several components due to the Zeeman effect.

Am star (m=metallic) spectra contain anomalous element abundances. The lines of rare earth metals and the heaviest elements are strong in their spectra and lines of calcium and scandium are weak.

Barium stars spectra contain strong lines of barium, strontium, rare earths and some carbon compounds.

In 1904 some untypical absorption lines were observed in the spectra of certain binary stars which were not Doppler shifted by the motion of the stars by *Johannes Hartmann*. It was supposed that these absorption lines were formed in gas clouds in the space between the Earth and stars. Generally, interstellar medium (ISM) contains *gas* and *dust* in the form of both individual clouds and of a diffuse medium. Interstellar space typically contains about one gas atom per cubic centimetre and 100 dust particles per cubic kilometre. The main properties of interstellar gas and dust are shown in *Table 1.1.1* [1].

Property	Gas	Dust
Mass fraction	10%	0.1%
Composition	H I, H II, H ₂ (70%) He (28%) C, N, O, Ne, Na, Mg, Al, Si, S, ... (2%)	Solid particles $d \approx 0.1\text{--}1 \mu\text{m}$ H ₂ O (ice), silicates, graphite + impurities
Particle density	1 cm^{-3}	$10^{-13} \text{ cm}^{-3} = 100 \text{ km}^{-3}$
Mass density	$10^{-21} \text{ kgm}^{-3}$	$10^{-23} \text{ kg/m}^{-3}$
Temperature	100 K (H I), 104 K (H II) 50 K (H ₂)	10–20 K

Method of study	Absorption lines in stellar spectra. Optical: Ca I, Ca II, Na I KI, Ti II, Fe I CN, CH, CH ⁺ Ultraviolet: H ₂ , CO, HD Radio lines: hydrogen 21 cm emission and absorption; H II, He II, C II recombination lines; molecular emission and absorption lines OH, H ₂ CO, NH ₃ , H ₂ O, CO, H ₂ C ₂ HCN, C ₂ H ₅ OH	Absorption and scattering of starlight. Interstellar reddening Interstellar polarization Thermal infrared emission
-----------------	--	---

Table 1.1.I. Main properties of interstellar gas and dust.

Almost 30 years had passed when the first *interstellar molecules* were discovered by their molecular absorption lines which were found in the spectra of some stars. Three simple diatomic molecules were detected: *methylidyne* CH, cation CH⁺ and *cyanogen* CN. The *molecular hydrogen* H₂ and *carbon monoxide* were discovered in the early 1970s by radio observations. Some discovered ISM molecules with the years and methods of discovery are illustrated in Table 1.1.II.

Molecule	Name	Year of discovery
<i>Discovered in the optical and ultraviolet region:</i>		
CH	methylidyne	1937
CH ⁺	methylidyne ion	1937
CN	cyanogen	1938
H ₂	hydrogen molecule	1970
CO	carbon monoxide	1971
<i>Discovered in the radio region:</i>		
OH	hydroxyl radical	1963
CO	carbon monoxide	1970
CS	carbon monosulfide	1971
SiO	silicon monoxide	1971
SO	sulfur monoxide	1973
H ₂ O	water	1969
HCN	hydrogen cyanide	1970
NH ₃	ammonia	1968

H ₂ CO	formaldehyde	1969
HCOOH	formic acid	1975
HCCNC	isocyanoacetylene	1991
C ₂ H ₄ O	vinyl alcohol	2001
H ₂ CCCC	cumulene carbene	1991
(CH ₃) ₂ O	dimethyl ether	1974
HC ₁₁ N	cyanopentacetylene	1981

Table 1.1.II. Some molecules observed in the interstellar medium.

1.2 Diffuse interstellar bands

In spite of the fact that significant progress in interstellar chemistry was achieved and many interstellar molecules were discovered, a new spectroscopic problem appeared early in the 20th century which is still not solved [6-7]. Along with the identified atomic and molecular electronic absorptions since then, more than 300 of such bands, whose origin remains unclear, were discovered which are called the Diffuse Interstellar Bands (DIBs). These bands are broad compared to sharp lines arising from atomic and diatomic species in space (*Figure 1.2.I*) [8-10].

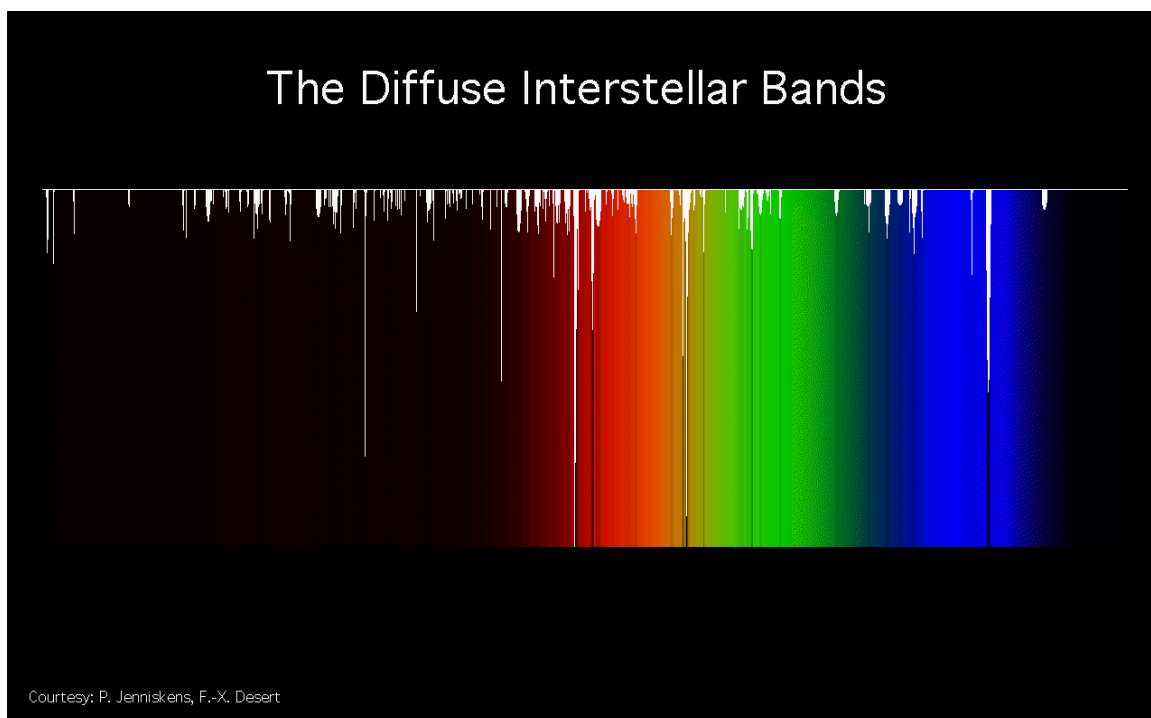


Figure 1.2.I. The Diffuse Interstellar Bands [11].

A large number of the molecular carriers were suggested, such as CO₂, O⁻, C⁻, H⁻, CH₄⁺ but all of them were disproven after careful laboratory studies. The problem is that DIBs central wavelengths do not correspond to any known spectral lines of any ion or molecule, and thus the

material, which is responsible for the absorption features, still needs to be found. There are a lot of theories which try to explain the DIB problem but the question of determining the nature of the absorbing material (the ‘carrier’ or ‘carriers’) is still open.

Two main features appear from the DIB study thus far. The *strengths* of most DIBs are not correlated with each other. Thus, it is believed that there are many carriers which are responsible for all DIBs instead of one. There are many spectroscopic results which show the strong correlation of DIBs and the interstellar *extinction curve* [8, 12] and it is supposed that DIBs can be somehow related to the interstellar dust. Generally, there are four trends in the carriers search. One trend is related to solid particles and interstellar dust as solid oxygen O₂ [13-14], defects in dust grains [15], impurity centres in grains [16], metallic ions in oxide grains [17], etc. Since carbon containing molecules are abundant in the ISM, Douglas proposed that carbon chains could be potential carriers of DIBs [18]. G. F. Mitchell, et al. [19], J. Fulara, et al. [20] and P. Freivogel, et al. [21] extended this idea to the whole class of linear, unsaturated hydrocarbons. Polycyclic aromatic hydrocarbons [22-23] and fullerenes [24-25] are among the most promising candidates due to their bands’ structures and positions. In 1971 Herzberg proposed a model that pre-dissociative transitions of the certain molecules can satisfy all DIB features [26]. Sorokin et al. [27] developed a non-linear theory, where inter-Rydberg transitions in gas-phase molecular hydrogen would cause DIBs. The UV photon to initiate this process is absorbed from the surrounding region of the hot stars. This is an elegant theory especially taking into account the abundance of molecular hydrogen in interstellar space. Over 187 DIBs are claimed to be assigned using this theory [23, 28]. However, their work was criticized by T. Snow [29].

Spectroscopy of molecular ions can be performed in many ways, either by trapping mass selected species in low temperature matrices or in the gas-phase including methods such as laser induced fluorescence (LIF) [30], cavity ring-down spectroscopy (CRDS) [31] and resonance enhanced multiphoton fragmentation techniques [32]. By coupling some of the gas-phase experimental techniques with pulsed supersonic jets, rotationally cold spectra are recorded in which fewer numbers of rotational states are populated than at room temperature. Another way to make a cold ensemble of ions is to confine them within an ion trap and collisionally cool them with cryogenic helium. By using action spectroscopy for means of detection, “cold” spectra are obtained. Within the present work, the latter is used with resonance two-color photofragmentation (R2CPF) [33-35] or multiphoton dissociation techniques to record the electronic transitions of positive species of astrophysical relevance.

CHAPTER 2

Theory of Linear RF Traps

The components used in the present experimental setup are: 22-pole ion trap, two quadrupoles and hexapole, so called linear radio-frequency (rf) devices. In 1989 W. Paul [36] from the University of Bonn and H. Dehmelt [37] from the University of Washington were awarded the Nobel Prize in physics [38]. They were awarded "for the development of the ion trap technique., which has made it possible to study a single electron or single ion with extreme precision". A popular introduction of their contributions is given elsewhere [39-41]. The award has brought recognition of the ion trap technique which started to be widely used since the advent of the commercial version of the ion trap as a mass spectrometer in 1983 [42]. The most popular schemes were introduced by Paul and Steinwedel in 1953 [36]. Ideally, the surfaces of electrodes are hyperboloids. In reality, more simple shapes are often used, resulting in small deviations from a pure quadrupole potential. The technique used is related to the Paul trap because it uses inhomogeneous rf-fields. However, field structures are more complicated and have quite different features [43-44]. These traps have a field free region much wider than conventional Paul traps and are thus well-suited for general low-temperature applications [44]. The 22-pole ion trap based on the design of Gerlich becomes a standard tool for the spectroscopic and reaction characterization of cold ions [33, 45-51].

2.1 Adiabatic approximation and effective potential

The standard equation of motion of a charge particle q and mass m moving in external electromagnetic field $\vec{E}(r, t)$ and $\vec{B}(r, t)$ is:

$$m\vec{\ddot{r}} = q\vec{E}(r, t) + q\vec{r} \times q\vec{B}(r, t) \quad (2.1.1)$$

Consider the magnetic field free problem, i.e. $\vec{B}(r, t) = 0$. Following the previous work of Gerlich [44], the electric field is composed of a static field \vec{E}_s and a time dependant part $\vec{E}_o(r) \cos(\Omega t)$ where $\vec{E}_o(r)$ is the field amplitude. Motion is then described by the differential equation

$$m\ddot{\vec{r}} = q\vec{E}_o(r)\cos(\Omega t) + q\vec{E}_s(r) \quad (2.1.2)$$

Assume the smooth field variation as a function of the coordinate r , and the frequency is high enough to keep the amplitude $a(t)$ small. Thus the solution vector r can be presented in superimposed form; a smooth drift term is $R_o(t)$ and rapidly oscillating motion is $R_1(t)$.

$$\vec{r}(t) = \vec{R}_o(t) + \vec{R}_1(t) \quad (2.1.3)$$

with

$$\vec{R}_1(t) = -\vec{a}(t)\cos(\Omega t) \quad (2.1.4)$$

presuming slow spatial variation of $\vec{E}_o(r)$ and expand the expression $\vec{E}_o(\vec{R}_o(t) - \vec{a}(t)\cos(\Omega t))$ by argument and keep only the first two terms in the expansion

$$\vec{E}_o(\vec{R}_o(t) - \vec{a}(t)\cos(\Omega t)) = \vec{E}_o(\vec{R}_o(t)) - (\vec{a}\nabla)\vec{E}_o(\vec{R}_o(t))\cos(\Omega t) + .. \quad (2.1.5)$$

and the slow time variation of a and R_o which leads to two inequalities $\dot{a} \ll \Omega a$ and $\ddot{R}_o \ll \Omega \dot{R}_o$ from which the following equation can be obtained

$$m\ddot{R}_o = -\frac{q^2}{4m\Omega^2}\nabla E_o^2 \quad (2.1.6)$$

Define time-independent part as potential V^*

$$V^* = \frac{q^2}{4m\Omega^2}E_o^2 + q\Phi_s \quad (2.1.7)$$

With this definition the equation of motion describing the smooth trajectory is

$$m\ddot{R}_o = -\nabla V^*(R_o). \quad (2.1.8)$$

The slowly varying amplitude of the superimposed sinusoidal oscillation is then

$$R_1(t) = -\frac{qE_o(R_o)}{m\Omega^2} \cos(\Omega t). \quad (2.1.9)$$

2.1.1 Laplace equation for electrostatics

Both fields E_s and E_o are derived from the potentials Φ_s and Φ_o , respectively. Because of the superposition principle $\Phi = \Phi_s + \Phi_o$ and the problem is therefore reduced to the solution of the Laplace equation under the inclusion of an appropriate boundary condition and space charge $\rho(r)$ is

$$\Delta\Phi(x, y, z) = -4\pi\rho(x, y, z) \quad (2.1.1.1)$$

In a space-charge-free limit the Laplace equation is

$$\Delta\Phi(x, y, z) = 0 \quad (2.1.1.2)$$

Boundary conditions are imposed by the geometrical structure of a manifold of electrodes, which are assumed to be equipotential surfaces and by the static and rf-voltages applied to each.

Functions which satisfy the Laplace equation may be found by applying the theory of complex variables. If the complex variable $z=x+iy$ is raised to an integral power n , then the result can be expressed as the sum of two functions, a real $U_n(x, y)$ and imaginary $V_n(x, y)$ part.

$$(x + iy)^n = U_n(x, y) + iV_n(x, y) \quad (2.1.1.3)$$

The integer n defines the order of the multiple fields. From complex variable theory, z^n is known to be analytic so the Cauchy-Riemann equations are applicable :

$$\left\{ \begin{array}{l} \frac{\partial U_n(x,y)}{\partial x} = \frac{\partial V_n(x,y)}{\partial y} \\ \frac{\partial U_n(x,y)}{\partial y} = -\frac{\partial V_n(x,y)}{\partial x} \end{array} \right. \quad (2.1.1.4)$$

The sum of the partial derivative of the first of these equations with respect to x and the partial derivative of the second of these equations with respect to y gives

$$\frac{\partial^2 U_n(x,y)}{\partial^2 x} + \frac{\partial^2 U_n(x,y)}{\partial^2 y} = 0 \quad (2.1.1.5)$$

Thus, the function $U_n(x,y)$ satisfies the Laplace equation.

The equipotential conductor surfaces are constructed so that they fall on the locus of points in the (x,y) plan defined by $U_n(x,y) = \pm \text{constant}$. The separation between opposite electrodes is chosen to be $2r_0$ to ensure that, for the case of the quadrupole, the standard quadrupole geometry is reproduced. Geometrically, adjacent conductors are arbitrarily chosen to have applied potentials of $\Phi_i = \frac{\Phi_0}{2}$ and $\Phi_i = -\frac{\Phi_0}{2}$, where Φ_0 is allowed to vary with the time [52].

In spherical coordinates

$$\Phi(r, \varphi) = \frac{\Phi_0}{2} \left(\frac{r}{r_0}\right)^n \cos(n\varphi). \quad (2.1.1.6)$$

Electric fields are gradient by definition and the corresponding potentials are

$$\vec{E} = (E_r, E_\varphi) = -\left(\frac{\partial}{\partial r} \Phi, \frac{1}{r} \frac{\partial}{\partial \varphi} \Phi\right) \quad \text{and} \quad (2.1.1.7)$$

$$\vec{E} = \frac{\Phi_0}{2r_0} n \left(\frac{r}{r_0}\right)^{n-1} (-\cos(n\varphi), \sin(n\varphi)). \quad (2.1.1.8)$$

In Cartesian coordinates

$$(E_x, E_y) = \frac{\Phi_0}{2r_0} n \left(\frac{r}{r_0}\right)^{n-1} (-\cos((n-1)\varphi), \sin((n-1)\varphi)), \quad (2.1.1.9)$$

where
$$\hat{r} = \frac{r}{r_0}. \quad (2.1.1.10)$$

In general, equations of motion of an ion can be written as:

$$\ddot{\hat{r}} - F(t)\hat{r}^{n-1}(-\cos((n-1)\varphi), \sin((n-1)\varphi)) = 0 \quad (2.1.1.11)$$

where
$$F(t) = \frac{nqU_0}{2mr_0^2} - \frac{nqV_0}{2mr_0^2} \cos(\omega t) \quad (2.1.1.12)$$

and

$$\Phi_0(t) = U_0 - V_0 \cos(\omega t). \quad (2.1.1.13)$$

The module of the electric field has only radial part

$$|E_0| = \frac{V_0}{2r_0} n \hat{r}^{n-1}. \quad (2.1.1.14)$$

Substitute Eq. (2.1.1.14) in Eq. (2.1.1.7) and the effective potential for multipole is obtained

$$V^* = \frac{n^2}{16} \frac{e^2}{m\omega^2} \frac{V_0^2}{r_0^2} \hat{r}^{2n-2} + q \frac{U_0}{2} \hat{r}^n \cos(n\varphi). \quad (2.1.1.15)$$

Figure 2.1.1.I depicts an effective potential Eq. (2.1.1.15) with U_0 equal to zero depending on different multipole traps

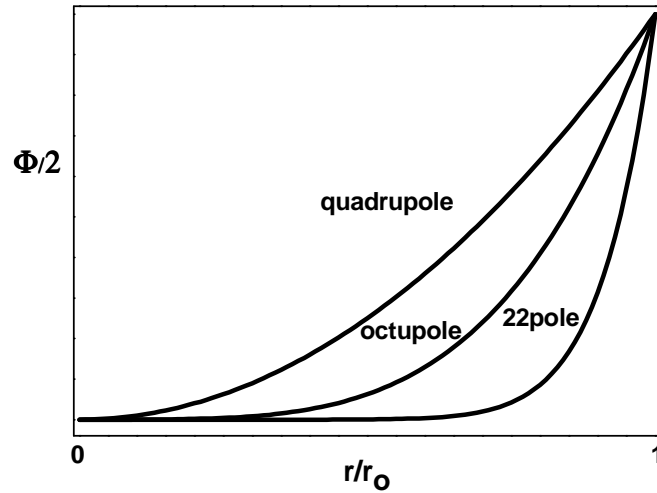


Figure 2.1.1.I. An effective potential dependence on multipole traps. The field free region for a 22 pole is larger than that for a quadrupole.

2.1.2 Safe operating conditions

Except for a quadrupole there is no diagram of stability for multipole fields $n > 2$ [53]. Related attempts to characterize the complete family of multipoles with $n > 2$ were unsuccessful [52, 54-56]. There is only an adiabatic way of characterization the family of multipoles [44].

The requirement of adiabatic approximation is that over the full distance of the oscillation, that is, over $2a$, the change of the field should be much smaller than the field itself

$$|2(a\nabla)E_o| < |E_o|. \quad (2.1.2.1)$$

Using this relation the characteristic parameter η is defined as

$$\eta = \frac{2q|\nabla E_o|}{m\Omega^2} \quad (2.1.2.2)$$

Because the vector E_o has only a radial component for ideal multipoles, see Eq. (2.1.1.14) one obtains final equation for the adiabatic parameter

$$\eta = 2n(n-1) \frac{qV_o}{m\Omega^2 r_o^2} \left(\frac{r}{r_o}\right)^{n-2} 1/2. \quad (2.1.2.3)$$

For safe operating conditions according to Gerlich [44], the adiabatic parameter is required to be

$$\eta\left(\frac{r}{r_o} = 0.8\right) < 0.3. \quad (2.1.2.4)$$

2.1.3 Space-charge limit in adiabatic approximation

The model of ion trapping in an adiabatic pseudopotential well is somewhat artificial in that the potential does not actually exist until an ion is held in a stable trajectory within an ion trap. Estimation can be done using the fact that adiabatic potential is balanced by a repulsive effective potential. For simplification, the direct current (dc) potential is assumed to be zero. The Gauss law Eq. (2.1.3.1) gives the possibility to estimate the coulombic repulsive field Eq. (2.1.3.2) in a trap [41].

$$\Phi_{\vec{E}} = \oint \vec{E} d\vec{S} = 4\pi Q \quad (2.1.3.1)$$

$$\vec{E} = 2\pi n_i r_o e \quad (2.1.3.2)$$

This coulombic repulsive field is balanced by a repulsive effective potential of a trap (2.2.15) [41]. Thus, the density of ions in a trap can be estimated by following formula

$$n_i = (n - 1)n^2 \frac{1}{16} \frac{V_0^2}{m\omega^2 r_0^4}. \quad (2.1.3.3)$$

The dependence of the trap capacity of a multipole is depicted in *Figure 2.1.3.I*. As it can be seen with the same dimensions the trap capacity of a 22-pole trap is more than 100 times the capacity of the linear quadrupole.

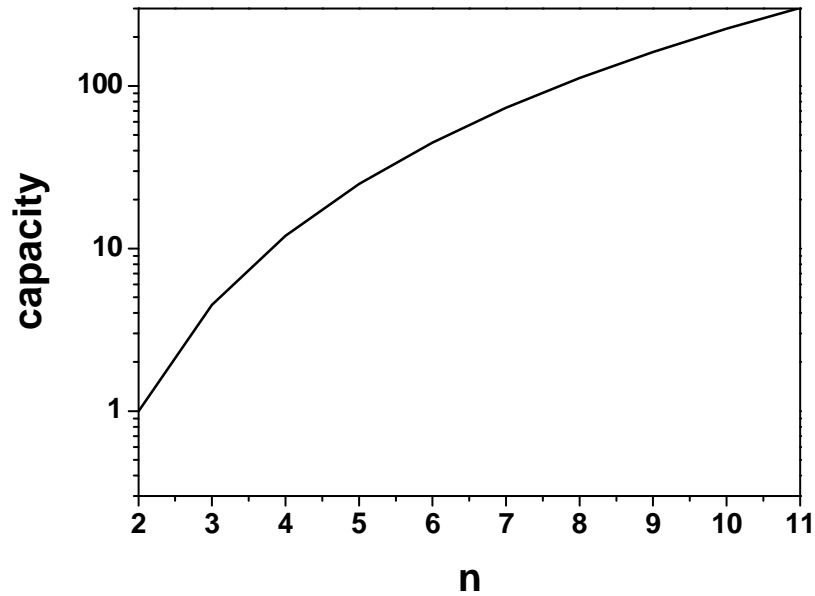


Figure 2.1.3.I Dependence of the trap capacity on multipoles.

The estimated number of ions which can be trapped in a 22-pole trap when the apparatus is operated under usual conditions is ca. 10^8 ions due to space-charge limit.

2.2 Oscillating quadrupole field

The potential for a quadrupole is given [36]

$$\varphi(x, y) = \frac{\varphi_0}{2r_0^2} (x^2 - y^2) \quad \text{and} \quad (2.2.1)$$

the equations of motion in Cartesian representation can be obtained simply substituting Eq. (2.2.1) in Eq. (2.1.1.11):

$$\begin{cases} m \frac{d^2x}{dt^2} + \frac{e}{r_0^2} (U_0 + V_0 \cos(\omega t)) x = 0 \\ m \frac{d^2y}{dt^2} - \frac{e}{r_0^2} (U_0 + V_0 \cos(\omega t)) y = 0 \end{cases} \quad (2.2.2)$$

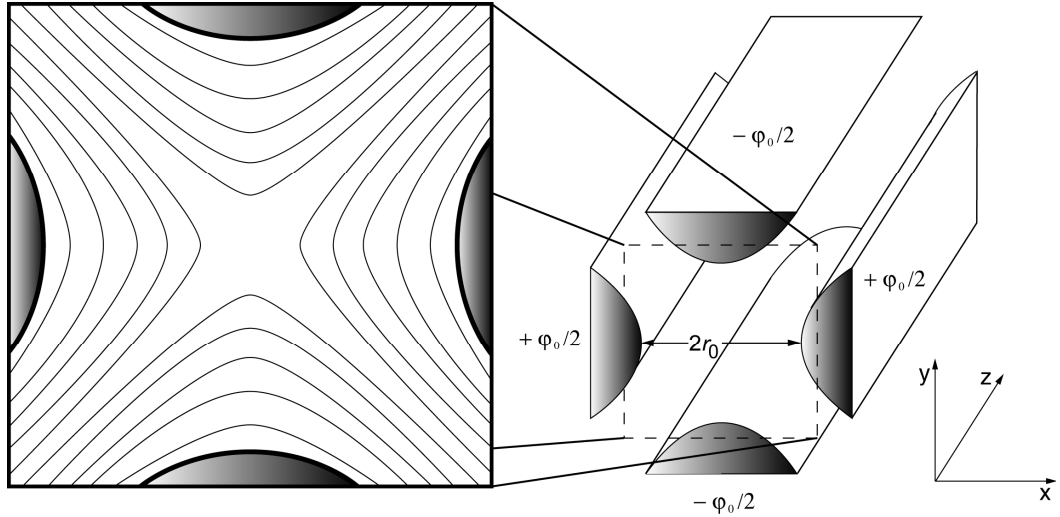


Figure 2.2.I Hyperbolic electrode structures required to generate the quadrupolar field. The equipotential field lines for such a configuration are shown in the inset.

For the confinement of ions in a beam, the electric field must be an axiperiodic quadrupole which, ideally, is created by four long vanes with surfaces conforming to $x^2 - y^2 = r_0^2$ and $y^2 - x^2 = r_0^2$ for the two sets. The geometry of such a set of vanes is shown in Figure 2.2.I. In practice however, hyperbolic rod surfaces are not easily manufactured and so purely cylindrical rods are used instead. The difficulty of machining an ideal vane structure has led to most such structures being formed from rods. Studies have shown that the closest approximation to a quadrupole field with such a structure is achieved when the rod diameter is 1.148 times the separation of opposite rods [57]. However, it should be noted that the effective r_0 to calculate the q from a voltage amplitude V between the rods is no longer exactly the actual distance of the inner surfaces of the rods from the centre.

Performing a change of variables by defining two dimensionless quantities

$$a_u = a_x = -a_y = \frac{4eU}{m\omega^2 r_0^2} \quad (2.2.2)$$

$$q_u = q_x = -q_y = \frac{2eV}{m\omega^2 r_0^2} \quad (2.2.3)$$

and expressing time in terms of a dimensionless quantity $\zeta = \frac{\omega t}{2}$, the equation now takes the form

$$\frac{d^2u}{d\zeta^2} + (a_u - 2q_u \cos(2\zeta))u = 0 \quad (2.2.4)$$

where u is either the x or y coordinate. Equation (2.2.4) is known as the Mathieu equation as expressed in its canonical form [58]. The stable solutions, i.e. solutions for which the particle trajectory remains bounded (trapped), can be expressed in terms of the two, independent ‘‘Floquet solutions:’’

$$u_1 = e^{\mu\xi} \phi_1(\xi) \quad (2.2.5)$$

$$u_2 = e^{-\mu\xi} \phi_2(\xi) \quad (2.2.6)$$

where $\phi_1(\xi)$ and $\phi_2(\xi) \equiv \phi_1(-\xi)$ are periodic functions of ξ with the same period as the coefficient in the Mathieu equation. This means that the Mathieu equation contains the term $\cos(2\xi)$ and ϕ_i is of period π . For bound solutions of the Mathieu equation, $\mu = \alpha + i\beta$ must be purely imaginary, i.e. $\alpha = 0$. The Fourier expansion of ϕ_1 and ϕ_2 gives the most general (bounded) solution of the Mathieu equation in the form [59]

$$u = A \sum_{n=-\infty}^{\infty} C_{2n} e^{i(2n+\beta)\xi} + B \sum_{n=-\infty}^{\infty} C_{2n} e^{-i(2n+\beta)\xi} \quad (2.2.7)$$

where A and B are integration constants which depend on the initial conditions, and C_{2n} are Fourier coefficients in the expansion of ϕ . Using Euler’s Theorem, the expression can be written in an alternative way

$$u = A' \sum_{n=-\infty}^{\infty} C_{2n} \cos(2n + \beta)\xi + B' \sum_{n=-\infty}^{\infty} C_{2n} \sin(2n + \beta)\xi \quad (2.2.8)$$

where $A' = A + B$ and $B' = A - B$. Inspection of Equation (2.2.8) gives the lowest frequency motion, that for which $n = 0$, is given by $\omega_0 = \frac{1}{2}\beta\omega$, where the next-highest frequency motion is at $\omega_0 \pm \omega$. To determine the characteristic frequency β , Equation (2.2.8) is substituted into the Mathieu equation (2.2.4) which gives

$$\sum_{n=-\infty}^{\infty} (C_{2n} [a - (2n + \beta)^2] - qC_{2n-2} - qC_{2n+2}) \cos[(2n + \beta)\xi] = 0 \quad (2.2.9)$$

By defining $D_{2n} = \frac{a - (2n + \beta)^2}{q}$, Eq. (2.2.9) can be rewritten as

$$-D_{2n}C_{2n} + C_{2n-2} + C_{2n+2} = 0 \quad (2.2.10)$$

and for $n=0$

$$D_0C_0 = \frac{a - \beta^2}{q} C_0 = C_{-2} + C_2. \quad (2.2.11)$$

From Eq. (2.2.10) D_{2n} can be obtained

$$D_{2n} = \frac{C_{2n-2} + C_{2n+2}}{C_{2n}} \quad (2.2.12)$$

After rewriting, the continued fraction can be concluded:

$$\frac{C_{2n}}{C_{2n-2}} = \frac{1}{D_{2n} - \frac{1}{D_{2n+2} - \frac{1}{\dots}}} \quad (2.2.13)$$

and similarly,

$$\frac{C_{-2n}}{C_{-2n-2}} = \frac{1}{D_{-2n-2} - \frac{1}{D_{-2n-4} - \frac{1}{\dots}}} \quad (2.2.14)$$

By substituting these formulae back into Eq. (2.2.10) and expressing D_{2n} , the solution for β of the desired order can be obtained. The lowest order is

$$\beta = \sqrt{a + \frac{q^2}{2}} \quad (2.2.15)$$

If the static potential is zero so that $a = 0$, then $\beta = \frac{q}{\sqrt{2}}$ and lowest-frequency is $\omega_0 = \frac{2\sqrt{2}eV}{mr_0^2\omega}$. The next-highest order in q for β is

$$\beta = \sqrt{\frac{a + q^2\left(\frac{1}{2} + \frac{a}{8}\right) + \frac{q^4}{128}}{1 - q^2\left(\frac{3}{8} + \frac{5a}{16}\right)}} \quad (2.2.16)$$

Ion motion in the exact treatment has the frequency components at $(2n \pm \beta)\omega/2$. The lowest frequency motion, which is identified with the secular frequency ω_0 , occurs at a frequency lower than the drive frequency ω . Other motions occur around the drive frequency or higher. In an ideal situation there is no component of the ion's motion at ω . Thus, rf-fields at ω of the trap do not couple energy into secular motion of particle. If there are fields at frequency $\omega \pm \omega_0$ which are due to noise from the rf producing the trapping potential, this can produce rf-heating of the secular motion. As the spectral purity of a typical rf-source is very high, this is usually not a problem.

The constants C_{2n} and μ , however, depend only on the values of a and q and do not depend on the initial conditions. Thus, the nature of ion motion is determined only on the basis of its (a, q) values, regardless of initial conditions (*Figure 2.2.II*). The solutions represented by Eq. (2.2.5 and 2.2.6) can further be divided into two subcategories: stable and unstable, depending on the behaviour of μ , which can be real, imaginary or complex. Stable solutions arise only when μ is purely imaginary such that $\mu = i\beta$ and β is not an integer. Integer values of β form a series of solutions which are periodic but unstable. Called the Mathieu functions of integral order they form the boundaries in (a, q) space between the stable and unstable regions. In practice, only the first stability region ($0 < \beta < 1$) is used for ion beam guides (*Figure 2.2.III*).

Mathieu Stability Diagram

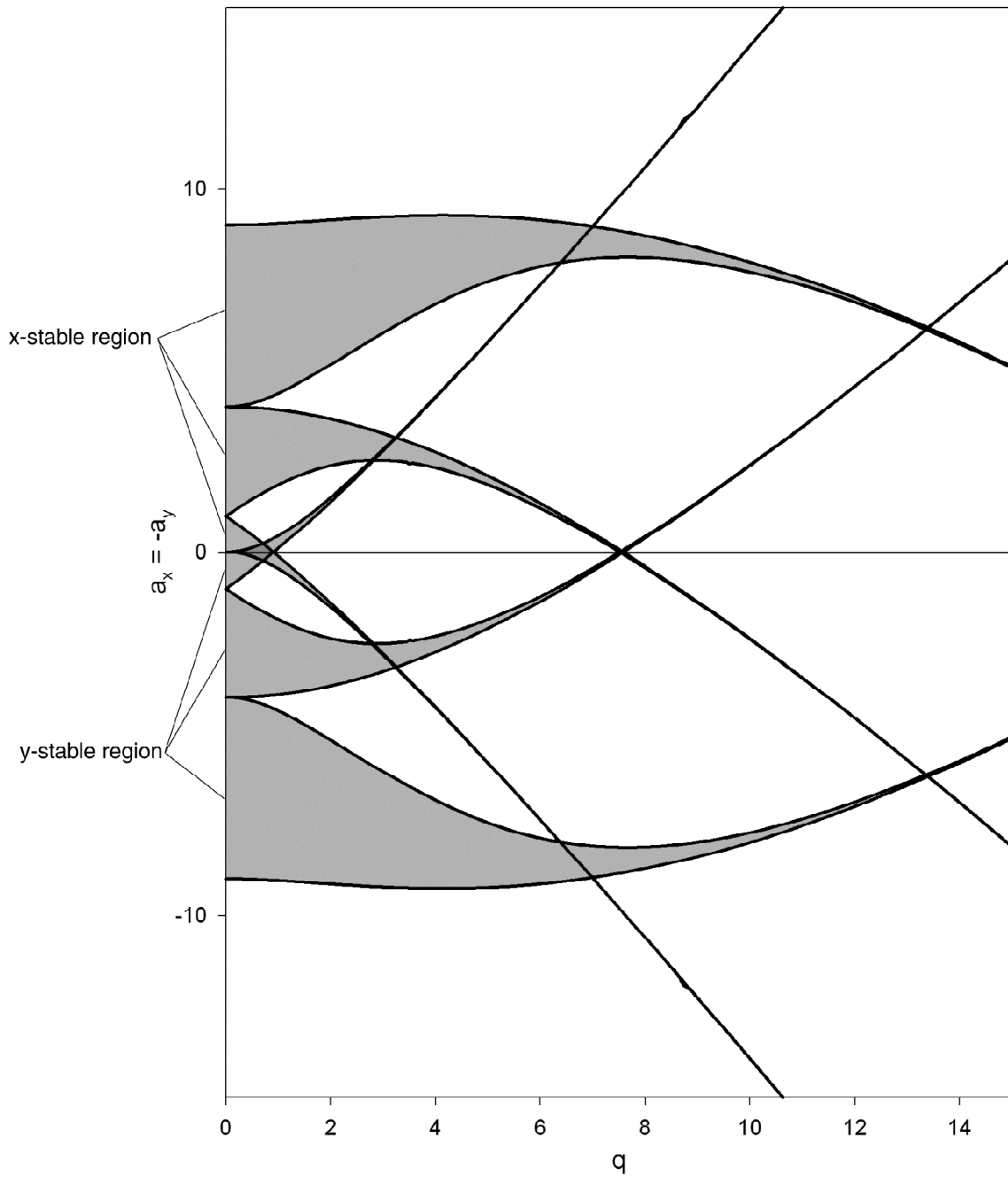


Figure 2.2.II. The Mathieu stability diagram for an ion beam guide, showing the regions of stability in the x and y directions. Areas of overlapping gray represent simultaneous stability in both directions.

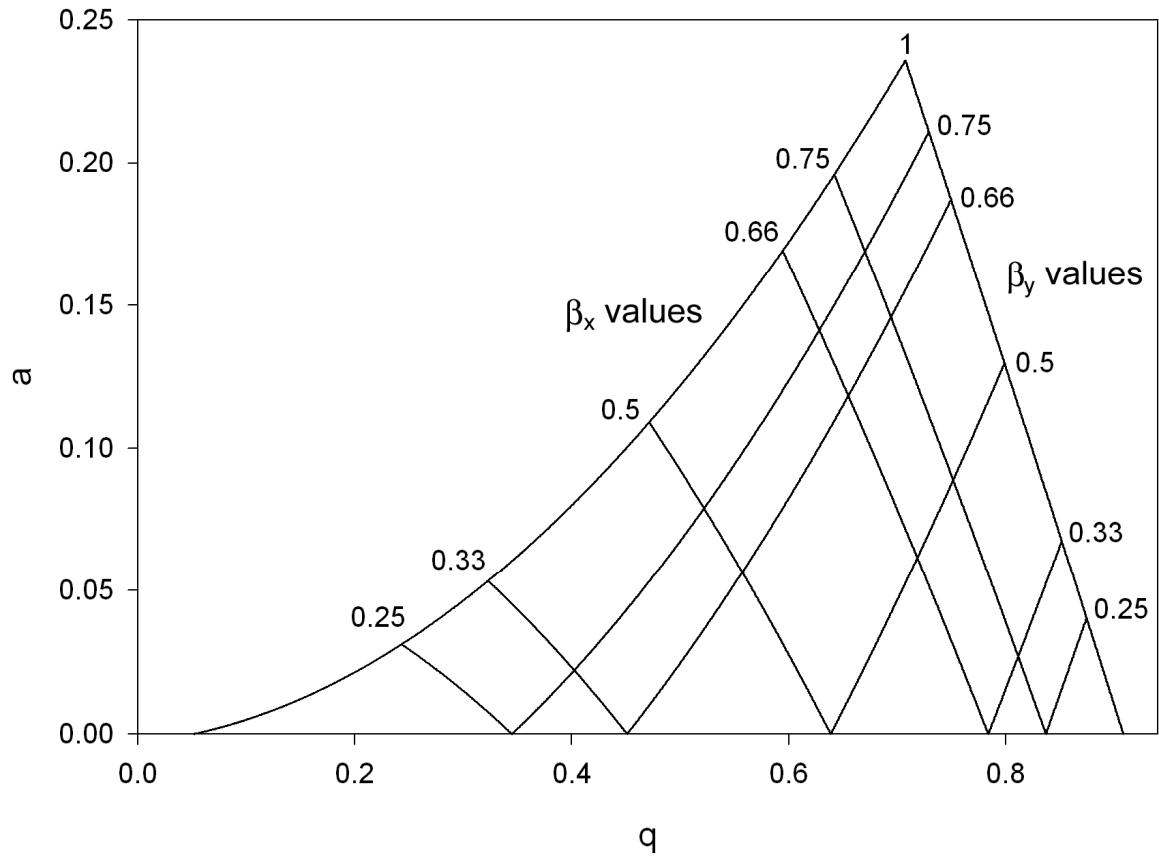


Figure 2.2.III. First stability region of the Mathieu diagram.

As the macromotion is simply harmonic, this motion can be explained in terms of a “pseudopotential well”. In this “well”, the macromotion energy is conserved, where it can be thought of as an oscillation in a potential well created by the rf-guide. The higher frequency oscillations (micro-motion) can be considered as perturbations on top of this large-scale motion of an ion.

Figure 2.2.IV demonstrates the simulated trajectories of ions in a linear quadrupole performed in *MatLab* [60] depending on parameter η .

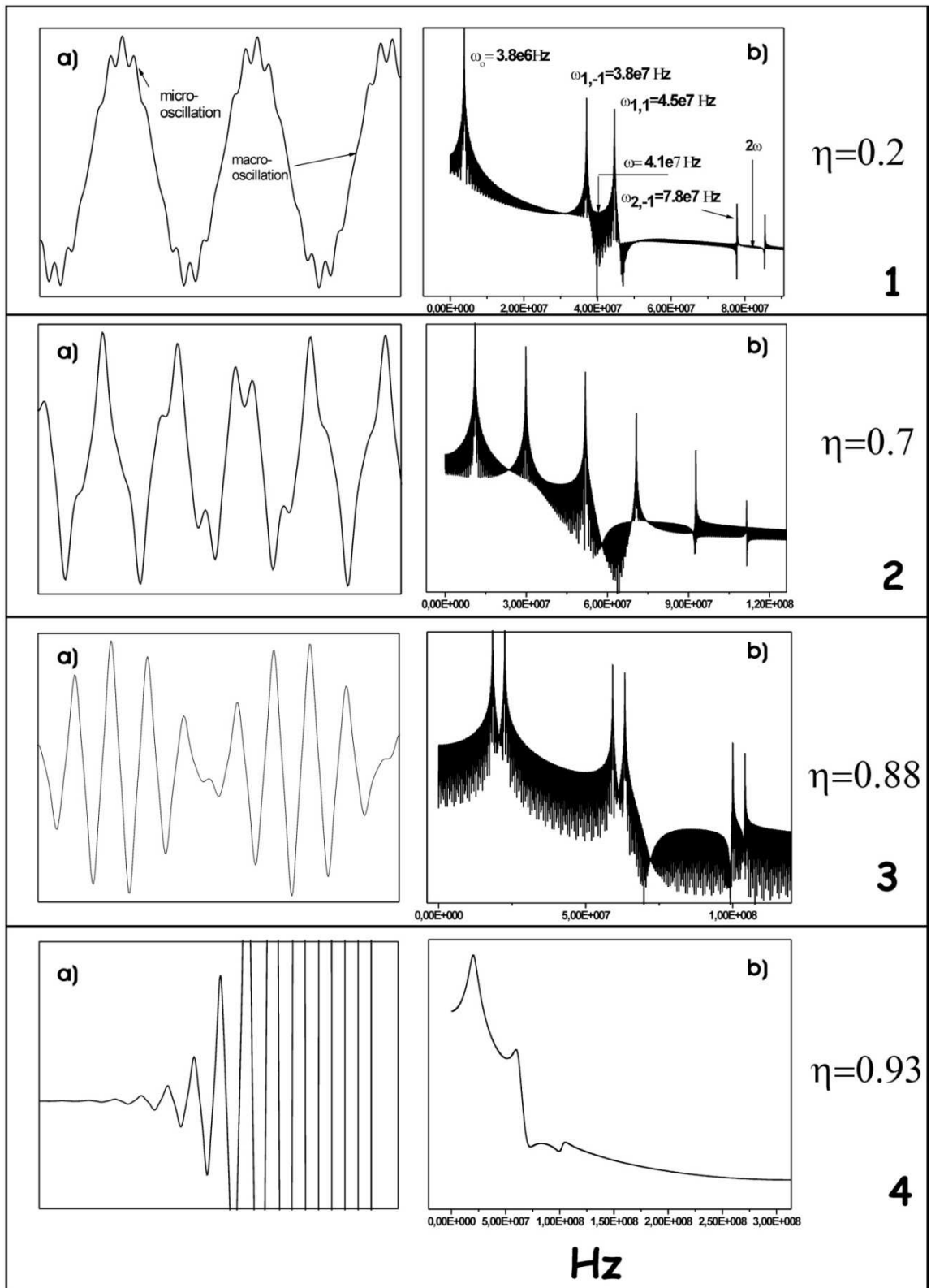


Figure 2.2.IV. Calculated trajectories a) of ions and Fourier transformation of their motions b) in a linear quadrupole trap, depending on the stability parameter η , where ω_0 is a secular motion of an ion. The y-scale of the Fourier transformation is in \log_{10} . Calculated trajectories are observed in the motion of an ion, becoming unstable when the magnitude of macromotion is comparable to the micromotion.

2.3 Ion temperature and phase space density

Phase-space dynamics technique is widely used for the description of an ensemble of ions in ion beam guides and traps [61]. This technique allows to visualize the time evolution of an ensemble of particles in which each particle has a different trajectory. The description of individual trajectories in terms of position (x, y, z) and momentum (p_x, p_y, p_z) coordinates at any point in time, i.e. these six coordinates (x, y, z, p_x, p_y, p_z) is known as the coordinates of particles in six-dimensional phase-space.

2.3.1 Liouville's theorem

Each particle determines the certain point in phase-space and each point represents a unique time and space evolution. All trajectories of particles in principle can be obtained from the Hamiltonian of the force field if the initial condition for each particle is known. For an ensemble of particles in six dimensional phase-space, it is possible to determine the infinitesimal volume surrounding them. At the border of this volume, there are boundary particles which can be moving with time. The number of points inside this volume is constant which means that points can never escape the boundary of a volume in phase-space, *Figure 2.3.1.1*. Similarly, the particle initially outside of the certain volume in phase-space can never enter inside of it.

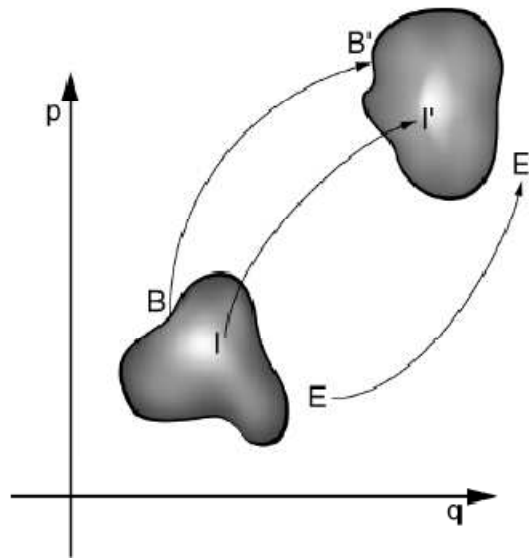


Figure 2.3.1.1. Liouville's theorem: Boundary points (represented by \mathbf{B}) define a volume in phase space as it evolves in time (\mathbf{B}'). Interior points (\mathbf{I}) must always stay within the volume (\mathbf{I}'), while points exterior to the volume (\mathbf{E}) remain outside (\mathbf{E}').

Thus, the number of points in an infinitesimal region dN and volume dV are constants, and the density $D = dN/dV$ must also be constant. This is a well-known statement of the Liouville's theorem

"The particles in phase-space form an incompressible gas. The shape of the surface surrounding a group of particles may change, but the density of particles remains constant. This property is the origin of the term 'water bag' ... the analogy is made with incompressible water contained in a hypothetical elastic bag which has zero elasticity so that it exerts no force on the fluid."

For the central potential all three canonical pairs of coordinates in phase space can be uncoupled, and thus, Liouville's theorem can be applied to each of the associated *action areas* (momentum displacement) separately.

$$\left\{ \begin{array}{l} \iint_{V_1} dx dp_x = C_x \\ \iint_{V_2} dy dp_y = C_y \\ \iint_{V_3} dz dp_z = C_z \end{array} \right. \quad (2.3.1.1)$$

where V_1 , V_2 and V_3 are the regions containing the ensemble of particles in x - p_x , y - p_y and z - p_z spaces, respectively.

2.3.2 Action diagrams, emittance and acceptance

In the central potential, phase space dynamics of particles can be decoupled in three pairs of coordinates and momentum $(p_x, x), (p_y, y), (p_z, z)$. In this case the entire system is presented by a boundary ellipse whose area contains all the paths of individual particles. In (q, p) coordinates a boundary ellipse can be expressed as $q^2 + 2\alpha qp + \beta p^2 = \varepsilon$.

$$\begin{aligned}\varepsilon &= \frac{\text{area of the ellipse}}{\pi} \\ &= q_{max} \times p_{int} \\ &= q_{int} \times p_{max}\end{aligned}\tag{2.3.2.1}$$

The angle θ , the major axis of the ellipse, forms with q axes is given by $\tan(2\theta) = \frac{-2\alpha}{\beta-\gamma}$ (Figure 2.3.2.I).

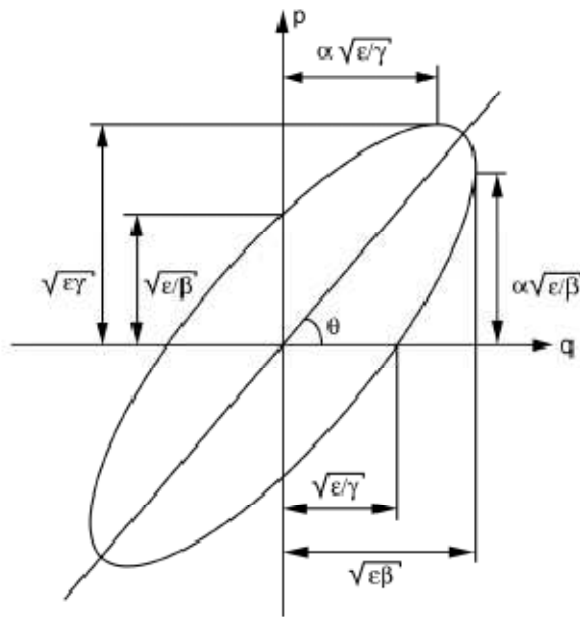


Figure 2.3.2.I. General action diagram ellipse showing critical values.

This area of the boundary ellipse can be treated in two ways. In a beam transport system, three orthogonal action diagrams represent the boundaries of an ensemble of particles which are called *emittance* ellipses of the system. Thus, the area of the ellipse or ε is used to characterize the emergent beam or pulse of the transport system.

From the other side, p and q values of the boundary ellipses are treated as limiting values for which a transport system transmits incoming particles. If particles do not satisfy the boundary values, then particles have either momenta p_x or coordinates that are too large or small to have entered the system. These ellipses then define the total phase-space volume accepted by the system and are named *acceptance* ellipses.

Using these two ellipses (the ellipse of acceptance and emittance), it is possible to determine the performance of ion transport system. Knowing the emittance and acceptance ellipses between two systems, it is possible to know exactly how many particles are admitted to the system undisturbed and with what positions and momenta, *Figure 2.3.2.II*.

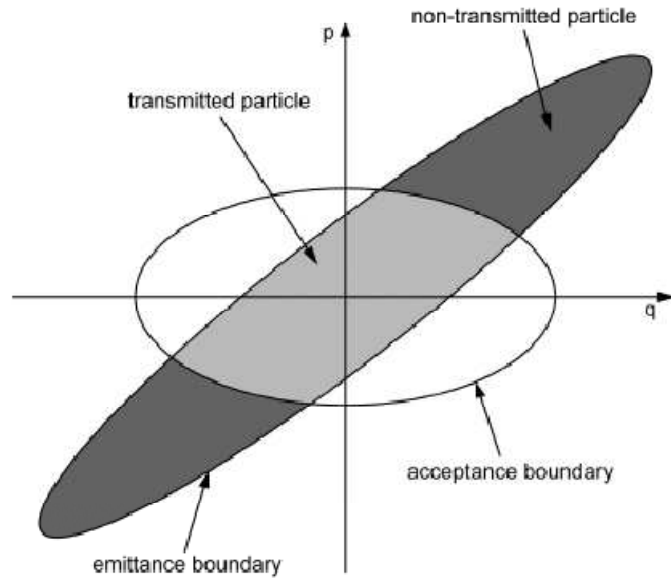


Figure 2.3.2.II. Emittance and acceptance ellipses.

2.3.3 Time evolution of action diagrams

For the field free situation, the evolution of the phase-space for particles is relatively simple. If an ensemble of identical particles occupies a rectangular region in phase-space with a width Δq and a height Δp , the time evolution of each particle can be expressed by the following equation

$$q(t) = q_i + \frac{p_i}{m}t \text{ and } p(t) = p_i \quad (2.3.3.1)$$

where q_i and p_i are the initial position and momentum coordinates at time $t=0$.

As can be seen in Eq (2.3.3.1), the original rectangular area is transformed into a parallelogram with time t . The spread of momentum Δp remains the same, as it should in the absence of any force and the spatial spread increases linearly with Δp (*Figure 2.3.3.I*).

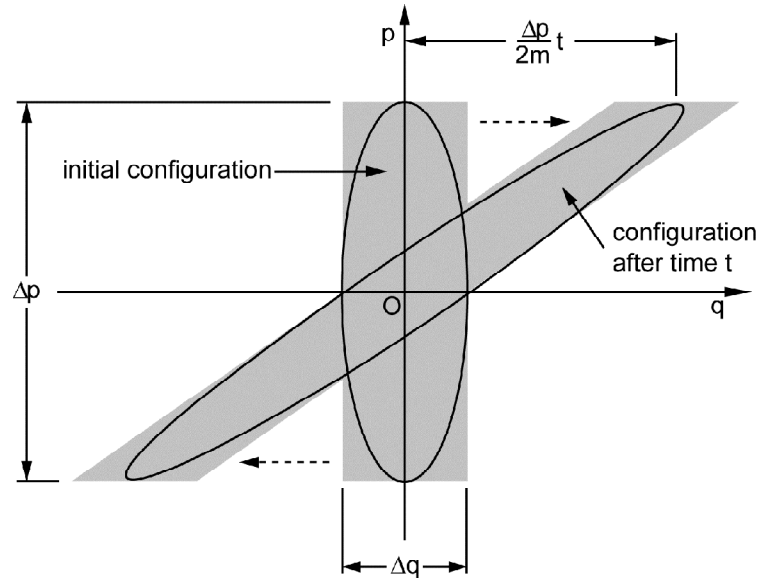


Figure 2.3.3.I. Action diagram of the time evolution of particles travelling in a field free region.

For the second situation under the influence of a uniform electric field, the ensemble will experience a change in momentum and coordinates. Furthermore if the system of identical particles occupy a rectangular area in phase-space with width Δq , and a height Δp and a force $F = eE$ acts in the positive q direction, the time evolution can be expressed by the following equation

$$q(t) = q_i + \frac{p_i}{m}t + \frac{e|E|}{2m}t^2 \quad (2.3.3.2)$$

and

$$p(t) = p_i + e|E|t. \quad (2.3.3.3)$$

Inspection of these equations gives information that the initial rectangular action area is transformed into a parallelogram (Figure 2.3.3.II). Also, because a force eE was introduced, the centre of the ensemble is shifted by $dq = eEt^2/2m$ and $dp = eEt$.

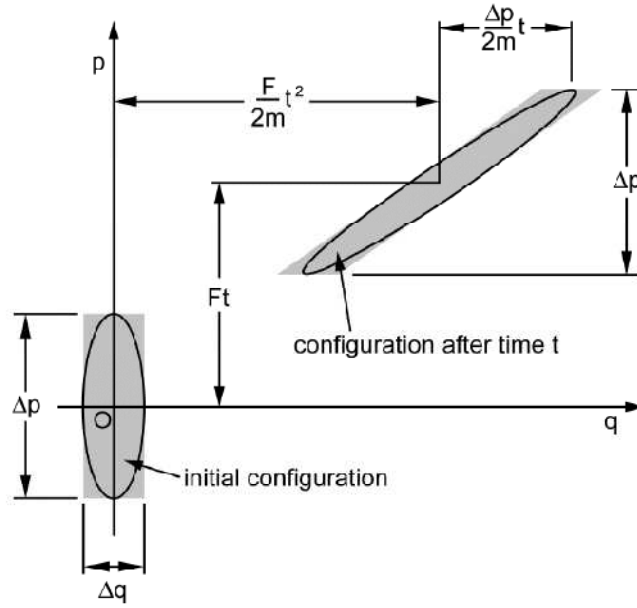


Figure 2.3.3.II. Action diagram of the time evolution of particles travelling in a constant field region.

2.3.4 Ion temperature and ion cloud

Consider an ensemble of particles of the ion cloud consisting from n particles in phase space in a pseudopotential well model of the rf n -poles ion beam guide. The Gibb's distribution by definition for these particles of temperature T , the number of particles N that occupy a volume S in phase-space can be written as

$$\frac{d^6N}{dS} = C e^{-\frac{E}{k_B T}} \quad (2.3.4.1)$$

where k_B is the Boltzmann constant.

For a simple harmonic oscillator, the motion, mentioned before, can be decoupled and it is possible to take into account each canonical pair of coordinates separately. For one dimension, the total energy E is

$$E = \frac{p^2}{2m} + \frac{1}{2}m\omega^2 q^2. \quad (2.3.4.2)$$

Replacing Eq.(2.3.4.2) into Eq.(2.3.4.1) and perform an integration over the two other pairs of canonical coordinates, the distribution can then be written as

$$\frac{d^2N}{dqdp} = \frac{N_0 \omega}{2\pi k_B T} e^{-\frac{m\omega^2}{2k_B T} \left(q^2 + \left(\frac{p}{m\omega} \right)^2 \right)}, \quad (2.3.4.3)$$

where N_o is the total number of particles in the ensemble.

Performing an integration over dq from $-\infty$ to $+\infty$ gives

$$\frac{dN}{dp} = \frac{N_o}{\sqrt{2\pi mk_B T}} e^{-\frac{p^2}{2k_B T}}. \quad (2.3.4.4)$$

and for dp gives

$$\frac{dN}{dq} = N_o \sqrt{\frac{m\omega^2}{2\pi k_B T}} e^{-\frac{m\omega^2 q^2}{2k_B T}}. \quad (2.3.4.5)$$

The Eq (2.3.4.5) gives the particle distributions in both position and momentum are Gaussian with standard deviations σ_p and σ_q equal to

$$\sigma_q = \frac{1}{\omega} \sqrt{\frac{k_B T}{m}} \quad (2.3.4.6)$$

$$\sigma_p = \sqrt{mk_B T} \quad (2.3.4.7)$$

An estimation of the effective size of an ion ensemble is possible to do through the integration of Eq. (2.3.4.5) to particular values of the amplitude A , resulting in the number N'

$$N' = N \left(1 - e^{-\frac{A^2}{2\sigma^2}}\right) \quad (2.3.4.8)$$

This is an ellipse which is corresponding to one sigma encompassing about 40% of the particles, an ellipse of two sigma about 87% and an ellipse of three sigma about 99% [61] (*Figure 2.3.4.I*).

For an ellipse of $\sqrt{6}\sigma$ macromotion of frequency ω_m , the area S , i.e. an action area, is

$$S = 6\pi \frac{k_B T}{\omega_m} \quad (2.3.4.9)$$

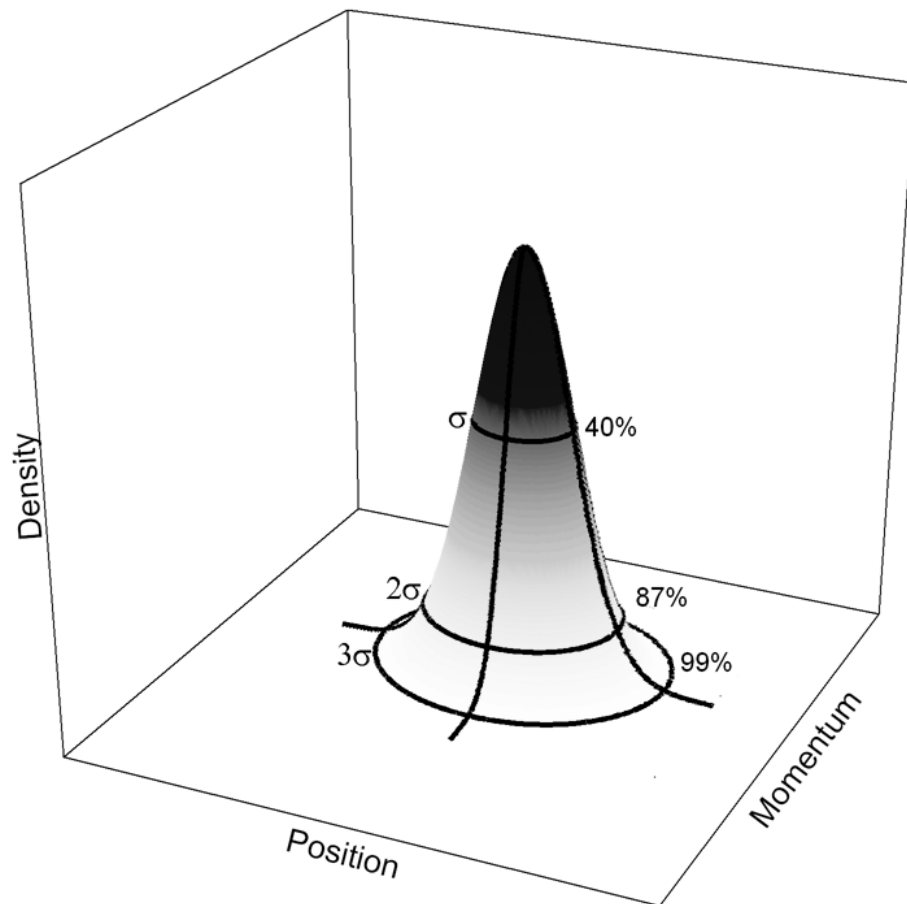


Figure 2.3.4.I Density distribution as a projection in an action diagram for a particular direction in phase space. The distribution represents particles in a simple harmonic oscillator at thermal equilibrium.

Thus, phase-space distributions of confined ions are critically dependent on the temperature of the system.

2.3.5 RF heating of macromotion

An ideal rf-field of an ideal ion trap does not heat the ions [43]. The rf-heating happens only in real ion traps by imperfections of the trap or by direct heating of the trap by the Ohmic losses of the rf-power. If the rf-amplitude is increasing, the effective potential becomes to be

steeper and the ions are confined to a smaller region. Usually, the number of ions in a typical 22-pole ion trap is about a few thousand ions which are necessary to avoid space charge effect. When the number of ions is high enough the space charge effect starts to influence. Coulomb repulsion forces push the ions towards the rf-electrodes and cause heating. The performed simulation for a linear 22-pole ion trap [43, 62] shows that linear ion densities in the range of about 10^3 per cm length are acceptable to have cryogenic temperatures, but when the ion number exceeds about 10^5 per cm, the heating becomes critical, and the simulated temperature for a density of 10^6 per cm approaches about 150 K. The electrostatic field of the end electrodes has components in longitudinal as well as in radial direction. The radial direction component pushes the ions into the rf-field and leads to a heating effect.

2.4 Inelastic collision of two particles

2.4.1 Relative speed between an ion and buffer gas, HS1 model

For simulations the HS1 model of collisions was used [63]. In this model the mean relative speed c between an ion and background gas has a form of

$$c = \iiint_V |v_{ion} - v_{gas}| f(v_{gas}) dv_{gas} \quad (2.4.1.1)$$

where $|v_{ion} - v_{gas}|$ is the relative speed between an ion and a gas particle of velocity v_{gas} , and $f(v_{gas})$ represents the probability density of gas particles with that velocity. Here, f is the three-dimensional Maxwell distribution given by

$$f(v_{gas}) = (A/\pi)^{3/2} \exp(-Av_{gas}^2) \quad (2.4.1.2)$$

where $A = m_{gas}/2kT$

This leads to the following equation

$$c = \bar{c}_{gas} \left((s + (2s)^{-1}) \frac{\sqrt{\pi}}{2} \operatorname{erf}(s) + \frac{1}{2} \exp(-s^2) \right), \quad (2.4.1.3)$$

where

$$\bar{c}_{gas} = \sqrt{\frac{8kT}{\pi m}} = \frac{2}{\sqrt{A\pi}}. \quad (2.4.1.4)$$

The mean gas speed is

$$c_{gas}^* = \sqrt{\frac{2kT}{m}} = \frac{1}{\sqrt{A}}. \quad (2.4.1.5)$$

The median gas speed is

$$s = \frac{c_{ion}}{c_{gas}^*} = a\sqrt{A} \quad (2.4.1.6)$$

where

$$a = |v_{ion}|. \quad (2.4.1.7)$$

2.4.2 Probability of a collision

In order to obtain the probability of a collision, the next model based on [64] was chosen. The probability of a collision $P(z)$ is given by following equation

$$P(z, t) = 1 - e^{-\sigma n z} = 1 - e^{-(v_z/\lambda)dt}, \quad (2.4.2.1)$$

where n is the density, σ is the cross section and z is the position of the ion. When an ion with velocity v_z moves a distance z in a time dt , the displacement of a ion in the buffer gas is $z = v_z dt$. The mean free path λ and the cross-section σ are related by $\sigma = \lambda n$.

2.4.3 Collision of two bodies

The particles which have a “0” label are related to the system of inertia. The model of inelastic collision based on [65] was chosen:

$$v = v_1 - v_2 \quad (2.4.3.1)$$

$$v_{10} = \frac{m_2}{m_1 + m_2} v \quad (2.4.3.2)$$

$$v_{20} = -\frac{m_1}{m_1 + m_2} v \quad (2.4.3.3)$$

$$v'_{10} = \frac{m_2}{m_1 + m_2} v \mathbf{n}_0 \quad (2.4.3.4)$$

$$v'_{20} = -\frac{m_1}{m_1 + m_2} v \mathbf{n}_0 \quad (2.4.3.5)$$

$$v'_1 = \frac{m_2}{m_1 + m_2} v \mathbf{n}_0 + \frac{m_1 v_1 + m_2 v_2}{m_1 + m_2} \quad (2.4.3.6)$$

$$v_2' = -\frac{m_1}{m_1+m_2} v n_o + \frac{m_1 v_1 + m_2 v_2}{m_1+m_2}, \quad (2.4.3.7)$$

where n_o is the normal unit vector in the centre-of-mass system (CMS), v_1, v_2 are the velocities of each particle before collision in the laboratory system of coordinates and m_1, m_2 are their respective masses. v_1', v_2' are the velocities of each particle after collision. The relationship between laboratory and center-of-mass systems is illustrated in *Figure 2.4.3.I*.

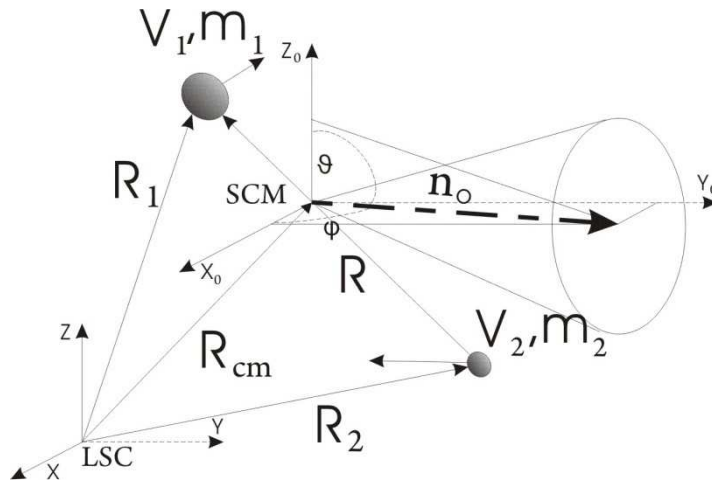


Figure 2.4.3.I. Scheme of collision of two bodies.

For hard sphere collisions, the scattering is isotropic in the center-of-mass system; therefore, the probability of scattering into the spherical polar element of solid angle $d\Omega = d\theta \sin\theta d\phi$ at angles (θ, ϕ) is

$$P(\theta, \phi) = \frac{d\theta \sin\theta d\phi}{4\pi}. \quad (2.4.3.8)$$

Integrating over ϕ yields the probability of scattering through angle θ :

$$P'(\theta) d\theta = \frac{\sin\theta}{2} d\theta. \quad (2.4.3.9)$$

For the application of the Monte Carlo method, a standard procedure is followed, where

$$\zeta_1 = \int_0^\theta P'(\theta) d\theta = \frac{1 - \cos(\theta)}{2} \quad (2.4.3.10)$$

and $\zeta_2 = \frac{\phi}{2\pi} \cdot \zeta_1$ and ζ_2 are random numbers between 0 and 1.

Using the equations above it was possible to simulate the heating or cooling processes. The simulations were performed in *MatLab* [60] program with an ensemble of 1000 particles (*Figure 2.4.3.II*).

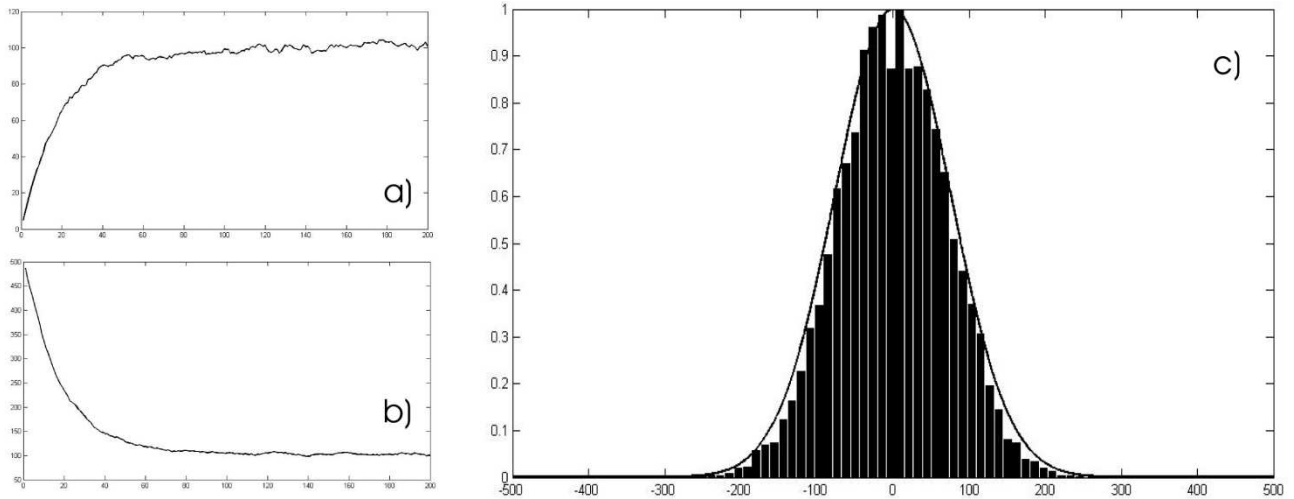


Figure 2.4.3.II. Illustrations of a) heating and b) cooling processes by collision with buffer gas. Each temperature point on a) and b) graphs is the analysis product of the ensemble of 1000 particles. c) An ensemble of particles has Maxwell-Boltzmann distribution.

2.5 Ion mobility

Ion mobility derives from the fact that the collision rate of an ion with gas molecules, while an applied electric field causes it to drift slowly through a gas, does not depend on its own drift velocity. The average collision rate is constant and the average rate of loss of momentum in the field direction is proportional to the ion momentum in that direction. In equilibrium this average rate of momentum loss is equal to the average rate of gain from the field, where the electric force on a particle and the average ion momentum in the field direction is proportional to the electric field. The relationship for drift velocity v_d of an ion in a gas is proportional to the electric field E in the gas [66-67]

$$v_d = KE, \quad (2.5.1)$$

where the proportionality constant K is referred to as the "ion mobility". Representative values for ions in gases at normal atmospheric pressure and room temperature are from 10 to 20 $\text{cm}^2\text{V}^{-1}\text{s}^{-1}$ for ions in helium and from 1 to 3 $\text{cm}^2\text{V}^{-1}\text{s}^{-1}$ for ions in nitrogen, where higher values being for light ions and the lower ones for heavy ions [61]. The ion mobility of any given gas is a particular characteristic of an ion and can sometimes be used to identify its presence in a gas by a technique referred to as Ion Mobility Spectrometry (IMS) [68-69]. At these drift velocities the ions should remain very nearly in thermal equilibrium with the gas. The effect of a background gas on the motion of a low velocity ion is to present a drag force F_d which is proportional to the velocity v , the proportionality constant is the ionic charge e divided by the ion mobility:

$$F_d = \frac{e}{K} v \quad (2.5.2)$$

The average rate of momentum loss of an ion is directly proportional to the collision rate with gas molecules. The ion mobility is therefore inversely proportion to this collision rate. If the molecular density N of the gas is decreased then the collision rate will decrease in proportion. As a consequence the ion mobility is inversely proportional to the gas density. Ion mobilities for specific ion-molecule systems are therefore quoted for standard gas temperature and pressure, meaning a density N_o of $2.69 \times 10^{19} \text{ cm}^{-3}$. Such mobilities are referred to as "reduced mobilities" and are designated K_o . The mobility at any other gas density N can then be obtained from

$$K = K_o \frac{N_o}{N} \quad (2.5.3)$$

The average motion under an applied electric field is approximated by integrating the equation of motion in presence of a frictional drag force [70]

$$m\ddot{x} = -\frac{e}{K}\dot{x} + eE. \quad (2.5.4)$$

The collision rate of ions which have an average velocity v and a cross section relative to molecules at a density N is Nv . Because the drag on an ion is proportional to this collision rate, the mobility is inversely proportional to the ion-molecule cross-section. Taking into account the geometrical and kinematic factors that determine the fraction of the field-direction momentum which is lost per collision, the following relationship is obtained (Mason-Schamp equation [71])

$$K = \frac{3e}{8N} \left(\frac{\pi}{2mkT_{eff}} \right) \frac{1}{\Omega(T_{eff})}, \quad (2.5.5)$$

where m and M are the masses of an ion and the molecules, respectively, k is the Boltzmann constant and $\Omega(T_{eff})$ represents the cross-section of ion-molecule collisions at the specific effective temperature T_{eff} of ion-molecular interactions defined by

$$\frac{3}{2}kT_{eff} = \frac{3}{2}kT + \frac{1}{2}Mv_d^2. \quad (2.5.6)$$

However, if the interaction potential is assumed to be given by the hard sphere limit, then $\Omega = \sigma$, where σ is the cross-section obtained when the individual atoms of a molecular ion and neutral collision partner are treated as hard spheres and is independent of temperature. As the final energy of cold ions should be in equilibrium with the gas, the corresponding room temperature energy is added to the acceleration term after each step; otherwise, the motion would be cooled to zero. This is done using the macromotion frequency ω_0 which represents the statistical motion of ions. This frequency is calculated from the operating parameters. The final acceleration term is therefore [72]:

$$\ddot{y} = \frac{e}{m} \left(E(x, t) - \dot{y}/K + \frac{v_{th}}{K_{th}} \cos(\omega_0 t) \right) \quad (2.5.7)$$

where v_{th} is the velocity of mass m corresponding to the chosen temperature (300 K) and K_{th} the mobility corresponding to v_{th} .

The cooling time of C_{60}^+ in 22-pole ion trap was obtained using collisional and ion mobility models. The initial temperature of ions was assumed ~ 1 eV. The temperature of the helium buffer gas in system was 8 K. The ion mobility parameter is $K_0 = 4.32 \cdot 10^{-4} \text{ m}^2/\text{V}\cdot\text{s}$ for C_{60}^+ in helium [73]. The estimated cross-section is $9.50 \cdot 10^{-19} \text{ m}^2$. The pressure of the buffer gas used in both models is 10^{-4} mbar and the number of particles is 1000. Collisional and ion mobility models lead to a cooling time $\sim 1.2 \cdot 10^{-5}$ and $5 \cdot 10^{-5}$ s, respectively. The simulations were performed using MatLab [60].

CHAPTER 3

Electronic Spectroscopy

3.1 Electronic spectroscopy (Born-Openheimer approximation)

In the first assumption the energy of the molecule can be presented as sum of three parts; an electronic, vibronic and rotational energy [74].

$$E = E_e + E_v + E_r$$

The probability of a transition induced by the oscillating electric field of a light wave is proportional to square of the transition moment integral,

$$M = \langle \psi'' | \hat{\mu} | \psi' \rangle^2$$

where the double prime denotes an excited state, single prime denotes ground state and $\hat{\mu}$ - dipole moment operator. This equation can be written out more completely as follow

$$M = \langle \psi_v'' | \psi_v' \rangle \langle \psi_e'' | \hat{\mu} | \psi_e' \rangle \langle \psi_s'' | \psi_s' \rangle$$

$$\langle \psi_v'' | \psi_v' \rangle - \text{basis of vibronic selection rules, Frank - Condon factor} \quad (3.1.1)$$

$$\langle \psi_e'' | \hat{\mu} | \psi_e' \rangle - \text{basis of orbital selection rules, pure electronic transition} \quad (3.1.2)$$

$$\langle \psi_s'' | \psi_s' \rangle - \text{basis of spin selection rules} \quad (3.1.3)$$

A transition will be orbitally allowed if the direct product of

$$\Gamma(\psi_e'') \otimes \Gamma(\mu_\alpha) \otimes \Gamma(\psi_e') \quad (3.1.4)$$

contains the totally symmetric irreducible representation of the point group of a molecule. The similar rule is applied for the $\langle \psi_v'' | \psi_v' \rangle$ integral. The Frank-Condon factor is non-zero, i.e. the transition is allowed, if the direct product

$$\Gamma(\psi_{vib}') \otimes \Gamma(\psi_{vib}'') \quad (3.1.5)$$

contains the totally symmetric irreducible representation of the point group of a molecule.

3.2 Vibration

Polyatomic molecules undergo complex vibrations. All these motions may be resolved into a superposition of a limited number of fundamental motions called normal modes of vibrations. In general, a molecule with n atoms has $3n-6$ modes of vibrations. A linear molecule has $3n-5$ modes of vibration. Each normal mode of vibration forms the basis for an irreducible representation of the point group of the molecule. Q is the normal coordinate along which the progress of a single normal mode of vibration can be followed. Mathematically, the normal coordinates are defined such that the potential energy of the molecule can be expressed as

$$V = \frac{1}{2} \sum_i \lambda_i q_i^2 \text{ and the kinetic energy as } K = \frac{1}{2} \sum_i \left(\frac{dq_i}{dt} \right)^2 \text{ where } \lambda_i \text{ is a constant.}$$

The symmetry for $\psi(0)$ vibronic wave function on the ground level is always transformed as totally symmetric irreducible representation. Generally, if q is nondegenerate irreducible representation then all the even wave functions are totally symmetric and odd wave functions have the symmetry of the vibrations. The rule to obtain the symmetry of a higher wave function is not so simple anymore. A recursion formula for the symmetry species of the ν th wave function of a doubly degenerate vibration is [75]

$$\chi_\nu(R) = \frac{1}{2} (\chi(R)\chi_{\nu-1}(R) + \chi(R^\nu)) \quad (3.2.1)$$

where

$\chi_\nu(R)$ – is the character under the operation R for the ν th energy level

$\chi(R)$ – is the character under R for the degenerate irreducible representation

$\chi_{\nu-1}(R)$ - is the character of the $(\nu-1)$ th energy level

$\chi(R^\nu)$ - is the character of the operation R^ν

$\chi(R) \equiv \chi_1(R)$

3.3 Rotation

In general, a molecule can rotate about three geometric axes and can have three different moments of inertia relative to these axes. The moment of inertia about an axis is defined as

$$I = \sum_i m_i r_i^2, \quad (3.3.1)$$

where r_i is a distance from the atom to the axis. The axes are chosen in such a way that the tensor of moment of inertia is diagonal. The three moments of inertia, I_x , I_y and I_z determine the layout of the rotational levels of molecule. The internal molecular axes are labelled as A , B , C so that $I_A \leq I_B \leq I_C$. Conventional classifications of molecules are:

linear molecules $I_A = 0, I_B = I_C$, for example HCN;

spherical tops, $I_A = I_B = I_C$, for example CH₄;

prolate symmetric tops, $I_A < I_B = I_C$, for example CH₃Cl;

oblate symmetric tops, $I_A = I_B < I_C$, for example BF₃;

asymmetric tops, $I_A < I_B < I_C$, for example H₂O.

3.3.1 Linear molecules

The rotational energy levels of a rigid linear molecule are given by $E_{rot} = BJ(J+1)$ where J is the rotational quantum number and B is the rotational constant defined as

$$B = \frac{h^2}{8\pi^2 I_B} \quad (3.3.1.1)$$

A real molecule is not a rigid rotor because the bond between atoms A and B can stretch at the same time as the molecule rotates. As rotation increases, the centrifugal force stretches the bond, increasing r and decreasing the effective B value. The bond length also depends, in an average sense, on the vibrational state v . The non-rigid rotor energy level equation for vibrational state v is

$$F_v(J) = B_v J(J+1) - D_v [J(J+1)]^2 + \dots, \quad (3.3.1.2)$$

where D_v and higher order terms are centrifugal distortion constants. The influence of a vibrational excitation is given as

$$B_v = B_e - \sum_i \alpha_i (v_i + 1/2) \quad (3.3.1.3)$$

neglecting higher order terms, where B_e is the rotational constant at the equilibrium geometry and α_i is the constant of rotation-vibration interaction.

The selection rules for rovibronic transitions (i.e. transitions that involve electronic excitation of molecule) are $\Delta J = 0, -1, +1$, giving rise to the *Q*-, *P*- and *R*-branches of the rotational structure, respectively.

3.3.2 Symmetric tops

A symmetric top rotor has the same moment of inertia about two principal axes. The three moments of inertia about these three principal axes are labelled I_a , I_b and I_c , with the convention that $I_c \geq I_b \geq I_a$. A symmetric top can have the two larger moments of inertia equal ($I_c = I_b > I_a$), which is called a prolate rotor, or it can have the two smallest moments of inertia equal ($I_c > I_b = I_a$), which is called an oblate rotor. If a molecule has a symmetry axis of three or more fold symmetry, it is always a symmetric top. Molecules of lower symmetry can be near-symmetric tops, having two rotational constants of close values and with a lack of spectral resolution they can behave like symmetric tops. Similar to linear molecules, a symmetric top has one of the principal axes along the molecular symmetry axis. In a prolate symmetric top, the *a*-axis lies along the symmetry and in an oblate symmetric top it is the *c*-axis. The rotational energy levels for the ground vibrational state of a rigid prolate symmetric top are represented as

$$E_{rot} = BJ(J+1) + (A-B)K^2 \quad (3.3.2.1)$$

where K is the projection of the total angular momentum, on the symmetry axis. For an oblate symmetric top,

$$E_{rot} = BJ(J+1) + (C-B)K^2, \quad (3.3.2.2)$$

where K must not be greater than J then as it represents the component of J . Because the energy does not depend on the sign of K , all states with the exception of $K = 0$ are doubly degenerate, corresponding to opposite directions of rotation around the symmetry axis. Figure 3.3.2.I shows the energy level diagram for symmetric top molecules. Every K stack has the structure rotational levels same as linear molecule but offset by $(A - B)K^2$ in energy.



Figure 3.3.2.I. Energy levels of prolate and oblate symmetric tops.

Spectra of linear and symmetric tops can generally be classified as parallel and perpendicular depending upon the direction of the electronic transition dipole moments. Parallel transitions occur when a transition moment is aligned along the axis of symmetry of the molecule within a given K stack.

$$\Delta K = 0 \text{ and } \Delta J = \pm 1 \text{ for } K = 0,$$

$$\Delta K = 0 \text{ and } \Delta J = 0 \pm 1 \text{ for } K \neq 0.$$

In the rigid rotator approximation, transitions in each stack will overlap each other and the resulting spectral lines will match those of linear molecule with the rotational constant B . If a transition dipole moment is perpendicular to the axis of symmetry, its interaction with the electromagnetic wave provides a torque around this axis, leading to

$$\Delta K = \pm 1 \text{ and } \Delta J = 0, \pm 1.$$

The spacing between two adjacent stacks, K and $K + 1$, is $(A - B)(2K + 1)$ that gives rise to a series of rotational progressions spaced by $2(A - B)$, so called K -structure. Figure 3.3.2.II shows the allowed transitions for a prolate top.

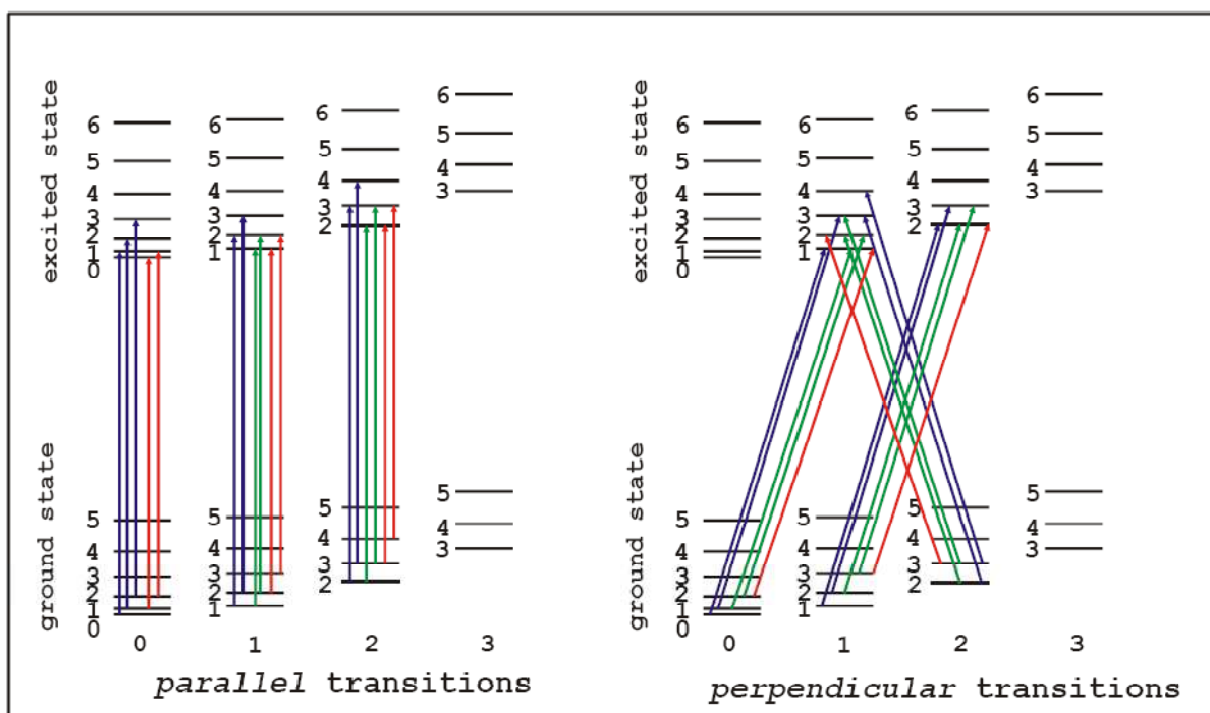


Figure 3.3.2.II. Allowed transitions for a prolate rotor and R-, Q- and P-branches marked with different colours.

3.3.3 Asymmetric tops

The majority of polyatomic molecules fall in the asymmetric-top category. When the three principal moments of inertia of a molecule differ, a molecule is classified as an asymmetric top. The energy level formulation for a rigid asymmetric top is considerably more complex than that for symmetric-tops or linear molecules. With the exception of low rotational levels, the rotational energy and transitions cannot be conveniently expressed in simple algebraic terms. Nonetheless, it is quite often that the moments of inertia about two axes are close in value and can be assumed to be a symmetric top rotor to a first order, with its levels split to remove the remaining degeneracy. Each level of the rotational quantum number J of an asymmetric rotor are split into $2J + 1$ levels which are specified by the quantum numbers K_a and K_c . The value K_a represents the projection of the angular momentum on the symmetry axis if the molecule is a prolate symmetric top rotor and the value K_c corresponds to the limiting case for an oblate

symmetric-top. In this way, the levels of an asymmetric rotor are labelled as $J_{K_a K_c}$. Ray's asymmetry parameter, κ , is often used to characterize the degree of asymmetry:

$$\kappa = \frac{2B - A - C}{A - C}$$

When $A \approx B$, κ approaches +1 for the oblate case and when $B \approx C$, κ approaches -1 for the prolate case. For asymmetric tops the rotational transitions can be classified as *a*-type, *b*-type and *c*-type depending upon the orientation of the electronic transition dipole moment to one of the rotational axes. For an asymmetric rotor the selection rules for

a-type transitions are:

$$\Delta J = 0, \pm 1; \Delta K_a = 0, \pm 2, \dots; \Delta K_c = \pm 1, \pm 3, \dots;$$

for *b*-type transitions:

$$\Delta J = 0, \pm 1; \Delta K_a = \pm 1, \pm 3, \dots; \Delta K_c = \pm 1, \pm 3, \dots;$$

for *c*-type transitions:

$$\Delta J = 0, \pm 1; \Delta K_a = \pm 1, \pm 3, \dots; \Delta K_c = 0, \pm 2, \dots;$$

CHAPTER 4

Experimental Setup

In this chapter the experimental setup is described. The 3D model of the machine is depicted in *Figure 4.I.*

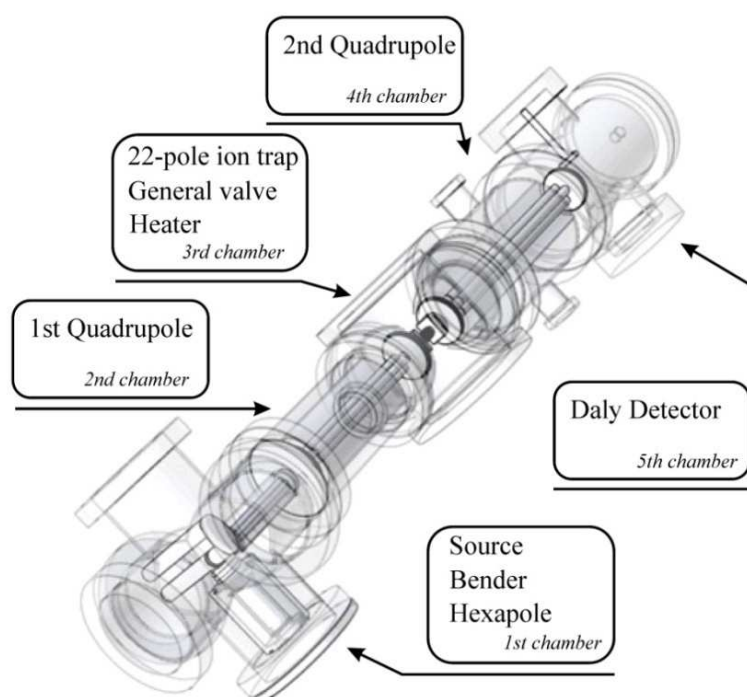


Figure 4.I. 3D model of the experimental setup.

The 22-pole ion trap experiment is composed of five vacuum chambers, mounted on a ball bearing track which consists of two (\varnothing 2.5 cm) stainless steel rods. This makes it convenient to open the chambers, alignment, cleaning and/or replacing components. The cold-head of the cryostat is supported on two rails track perpendicular to the main part of the experiment, making for simplicity in opening the ion trap chamber.

The system is evacuated by five turbo pumps. The source chamber is pumped by one turbopump Pfeiffer model TMU 521 (520 ls^{-1}) and by a membrane backing pump. The chamber is separated from the rest of the system by a differential wall. This is done to protect the quadrupole mass filters from being operated at relatively high pressure ($5 \cdot 10^{-5} \text{ mbar}$) and to avoid gas condensation on the cryogenically cold 22-pole ion trap.

The second, fourth and fifth chamber is equipped with TMU 261 (210 ls^{-1}) turbopump and the rest third chamber is equipped with TMU 521 (520 ls^{-1}) turbo pump. Exhaust lines of four turbopumps are combined using long stainless steel bellows, about 2.5 cm in diameter, which are then pumped out by a small turbo and membrane pump. A membrane pump is used to avoid oil contamination of the system. When one breaks vacuum, the apparatus is filled with argon gas to avoid water attachment to the inner walls and surfaces of the system. This procedure significantly shortens the subsequent pumping time.

The system is sealed by conflate (CF) flanges, with OFC gaskets. Upon evacuation, within one week the entire system reaches pressure as low as 10^{-9} mbar . Pressures inside the chambers are measured using Pfeiffer Vacuum Compact Cold Cathode Gauges (IKR261). The backing pressure is monitored using a Pirani Gauge. All electrical electrodes, ion sources, etc. are made of stainless steel, with the only exception being the 22-pole ion trap, which is made out of copper.

4.1 First Chamber (Source chamber)

The components of the first chamber are the electron impact source, magnetic bender and hexapole are depicted in *Figure 4.1.1*.

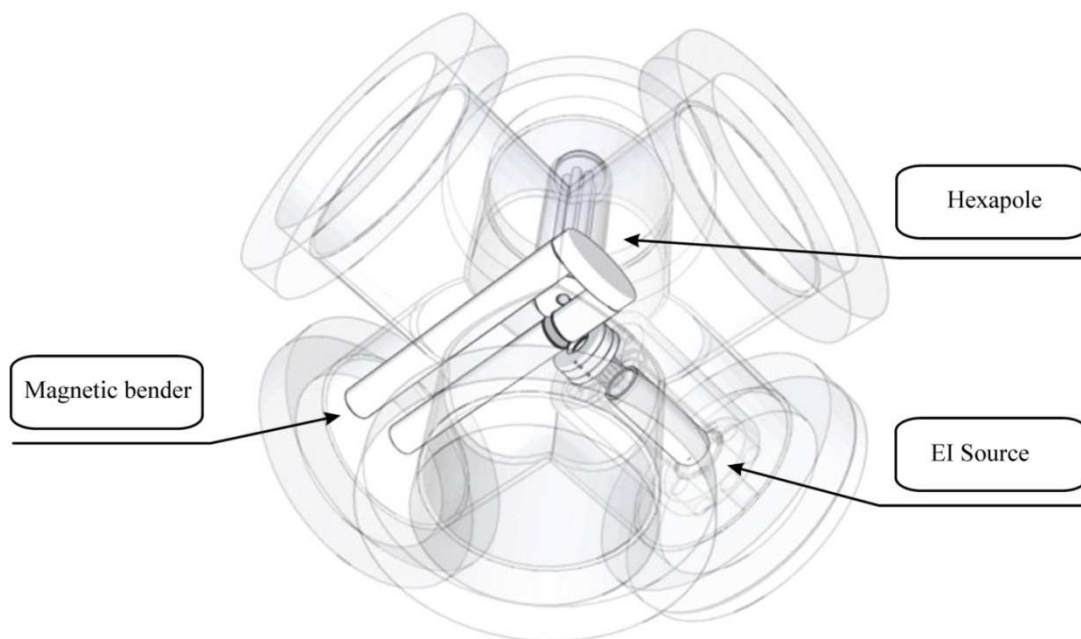


Figure 4.1.1 First vacuum chamber: magnetic bender, electron impact source and hexapole.

4.1.1 Electron Impact Ion Source

The source consists of an oven to vaporize the solid samples and a gas inlet, which introduces flow of vapours of volatile substances to an ionization region of the source. The oven, shown in *Figure 4.1.1.I*, is a stainless steel fixture, about 5.5 cm in length and 2.5 cm in diameter, that is threaded on the outside.



Figure 4.1.1.I. Oven of the source.

The oven is wrapped with a heating element that has a twin core heating element. This has the major advantage that when current flows through the heating element, it actually flows through each section of the element in both directions, thus cancelling out any magnetic field, generated by the electrical current. This is critical for creating a reproducible ion flux that is not disturbed by the generated magnetic field of a oven heater. A stainless steel sleeve slips over the heating element, minimizing heat loss and reaching a maximum temperature of 1000 K. The temperature is measured by a thermocouple through a hole drilled into the stainless steel fixture. The entire assembly is surrounded with a second stainless steel heat shield.

The ionizer contains a thin thorium doped tungsten wire (Goodfellow, 99.4 % W, 0.6 % Th, annealed, \varnothing 0.1 mm) mounted on four electrically isolated holders. Heated by 2.2 A electrical current, the filament emits electrons to the center of the ionizer. The electrons are additionally accelerated by a negative potential (10 – 30 V) applied to the filament with respect to the ground.

The principle electrical schematic of the ionizer is shown in *Figure 4.1.1.II*.

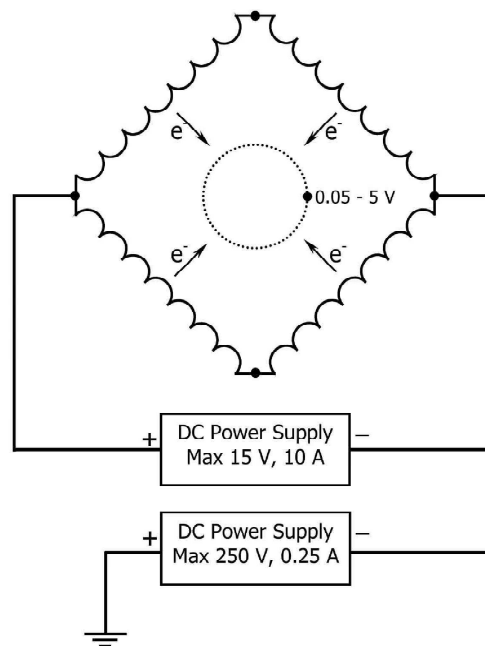


Figure 4.1.1.II. Schematic electrical connection of the ionizer.

Ions are created in a small cylindrical piece made of metal mesh (9 mm in diameter, 11 mm long). The cylindrical mesh is mounted only a few mm from the orifice of the oven. The mesh is held at a positive potential in the range of 0.05-5.0 V. This potential actually defines the translational energy of the charge particles. Ions created within the mesh can then escape through the mesh if they have more than 5.0 eV of kinetic energy. Otherwise, they will be trapped and can only escape through the extraction lenses into the hexapole. Ions created by an electron impact in the inner volume of the cylindrical mesh are then extracted by the electrode, which is usually at 15 V (*Figure 4.1.1.III*).

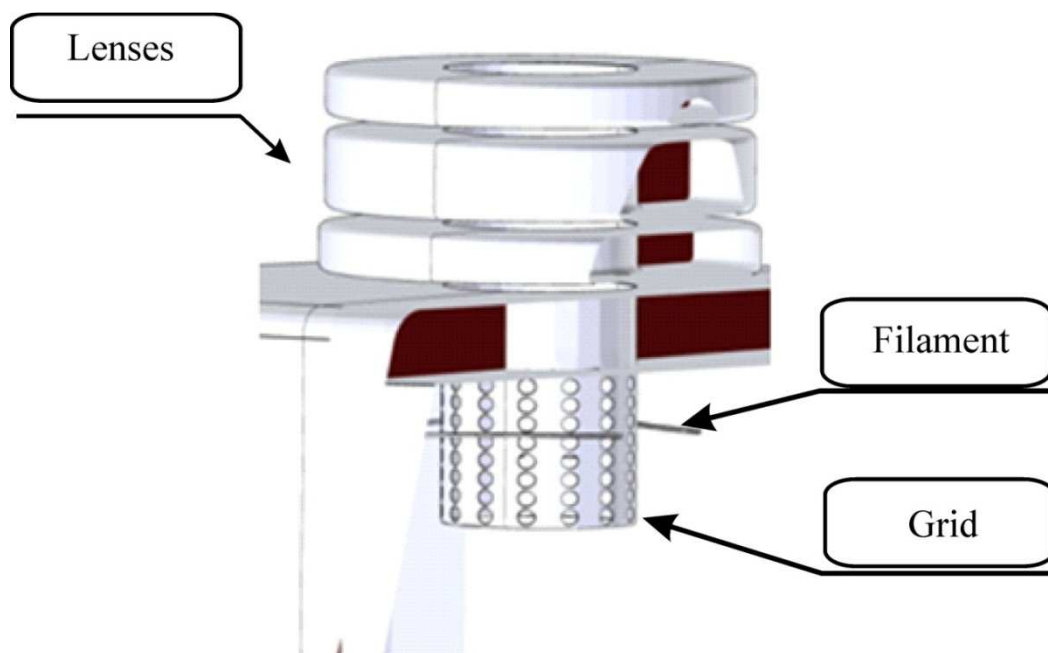


Figure.4.1.1.III. Electron impact source with the grid, filament and electrostatic extraction lenses.

The entire ionizer assembly mounts onto the outer heat shield of the oven, and the last element of the assembly, extraction lens, are perpendicularly oriented to the magnetic bender, *Figure 4.1.1.IV*.

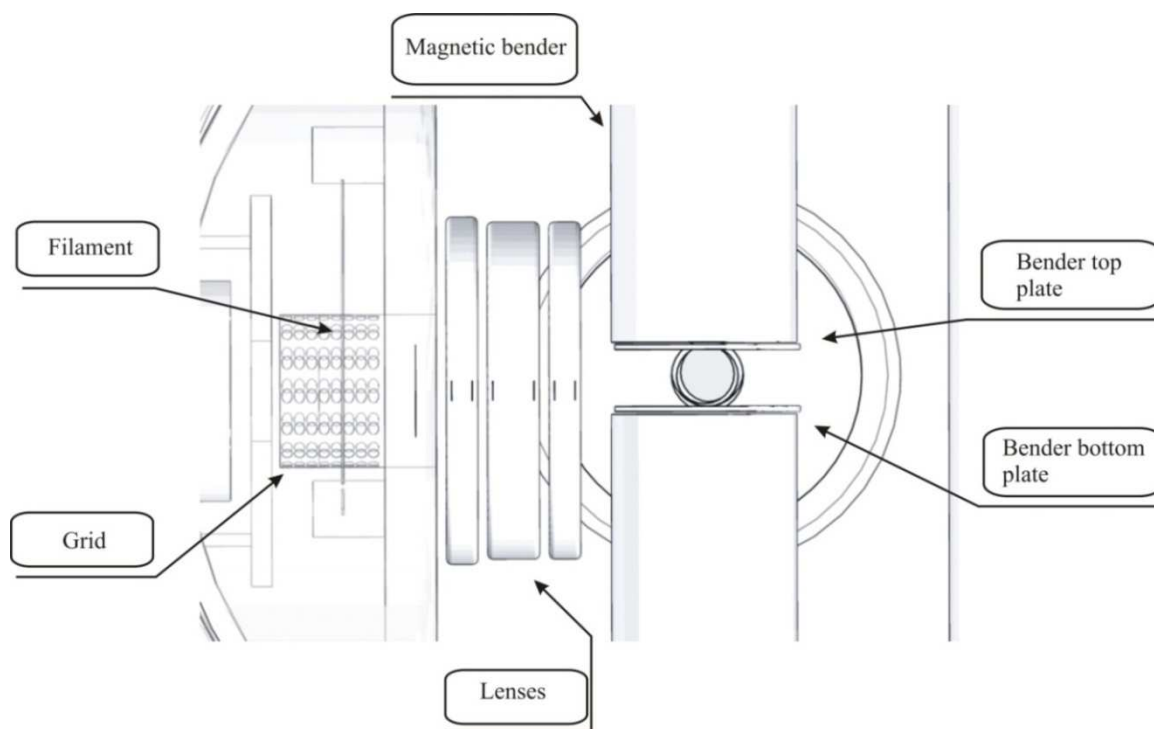


Figure.4.1.1.IV. Electron impact source and the rods of magnetic bender

4.1.2 Magnetic Bender

As can be seen in the above *Figure 4.1.1.IV*, ions generated in the source are then bent by a magnetic field. The magnetic bender is followed by a hexapole, which guides the ions into the first quadrupole mass spectrometer. With such a configuration most of the neutrals will end up in the turbopump of the source chamber, allowing only charged particles to enter the rest of the apparatus.

The design of the bender is depicted in *Figure 4.1.2.I*. It is simply two iron rods which are connected on top and one of the rods is surrounded by bear copper wire. The current flowing in copper wire causes a magnetic field which is perpendicularlly oriented to the flying ions, according to the Lorentz force of the magnetic field acting on the trajectory of ions. The electrical connections of the bender are connected to the power supply where the current can be changed and accordingly the force of the magnetic field is changing. Additionally, two electrostatic plates help to vary the deflection angle of ions and guide them through the first electrostatic lens of the hexapole.

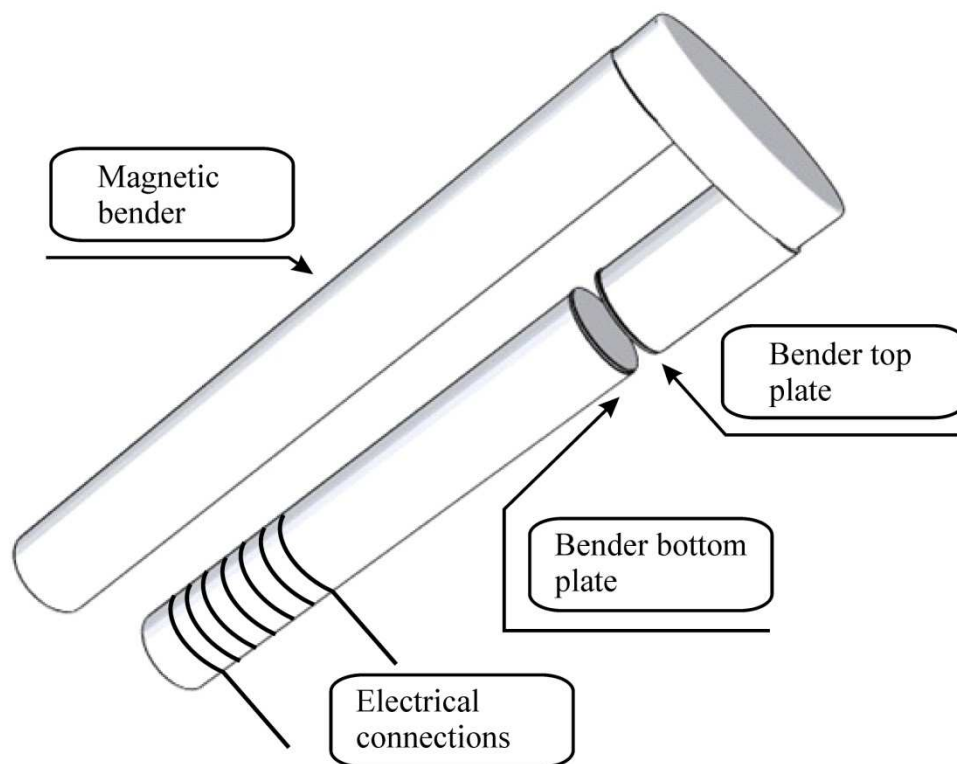


Figure 4.1.2.I. Magnetic Bender.

4.1.3 Hexapole

A hexapole, based on design by Gerlich [44], is an ion guide rf-device consisting of six rods that are connected to the two outputs of a rf-generator. The diameter of the hexapole rods is 5 mm with a length of 110.5 mm. The usual operation frequency is 3.3-3.7 MHz. The amplitude of rf-potential usually is about 200 Volts. Mostly for the ions of interest the adiabatic parameter for the masses up to 720 u is less than 0.3.

By filling the hexapole with room temperature helium buffer gas, ion velocities can be equilibrated, resulting in a better mass resolution of the first quadrupole. Additionally, ions can be trapped in the hexapole and probed by laser radiation. For example, under the influence of UV radiation, one can deprotonate ions, thereby combining the source and hexapole and use these two as an advanced ion source. From both sides of the hexapole two electrostatic lenses are attached for the focussing and defocussing of ions.

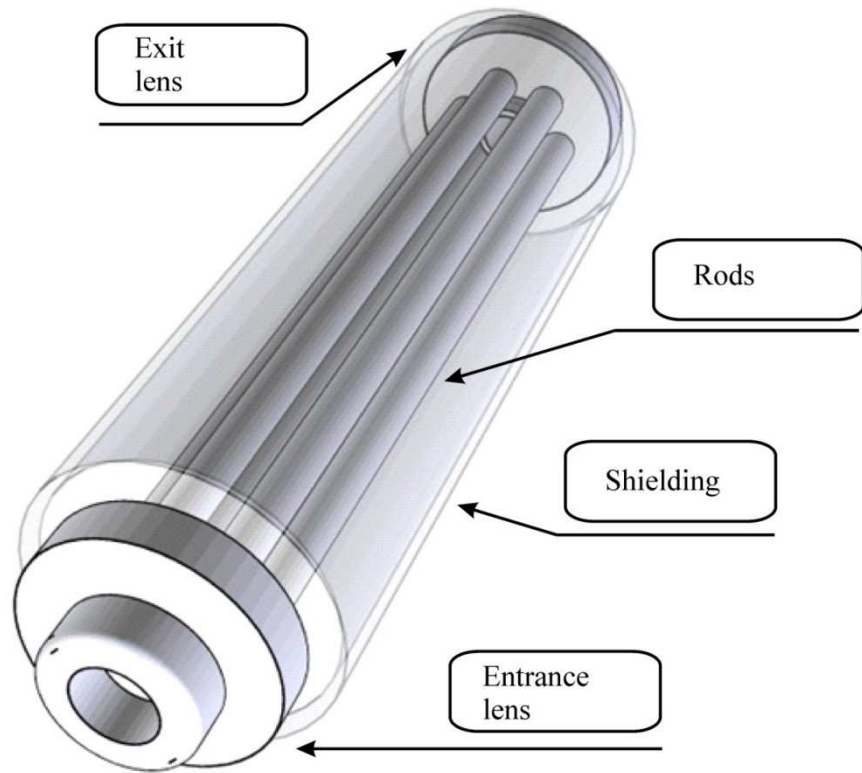


Figure 4.1.3.I. The hexapole with electrostatic lenses and shielding is depicted.

4.2 Second Chamber (Mass Filter)

The second chamber consists of a differential wall, four electrostatic lenses and a quadrupole mass filter. The principal scheme is depicted in *Figure 4.2.I*. The differential wall preserves the rest of setup from contamination by neutrals.

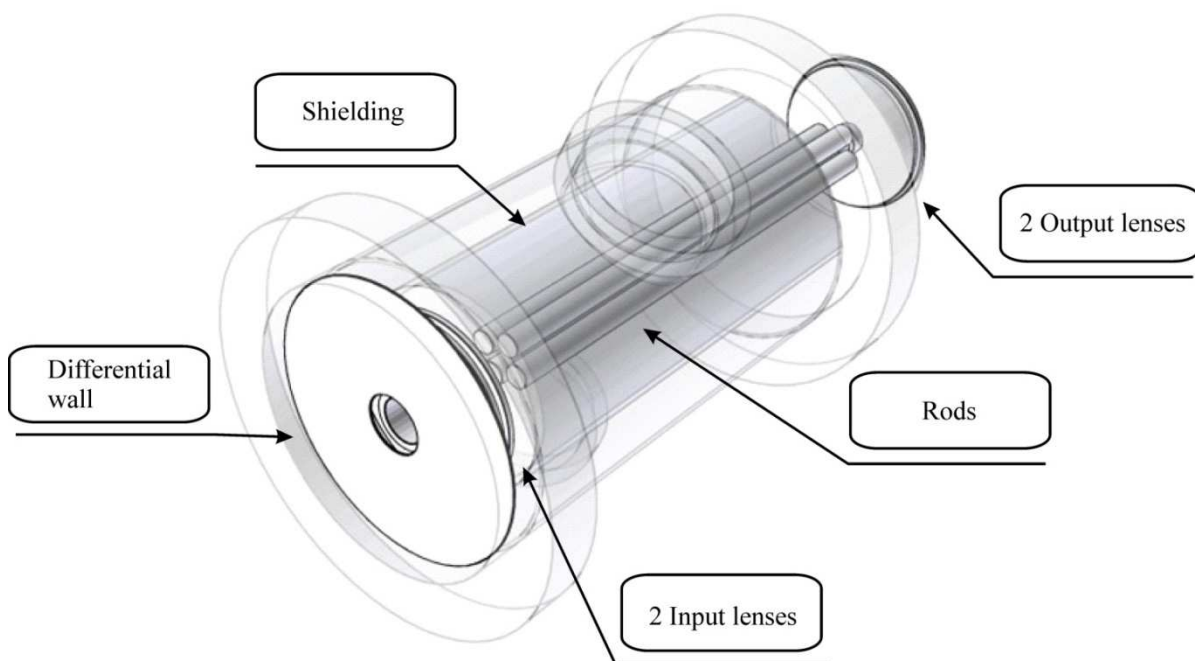


Figure 4.2.I. Second chamber: quadrupole, electrostatic lenses, shielding and differential wall.

The first mass filter in the apparatus is a home built quadrupole. It has 9.5 mm diameter rods with a length of 220.2 mm, and a rf-supply that provides 300 W of power at 1.2 MHz and a mass range of 2000 Daltons. The DC power supply is a model U-1272 and rf-power supply is model 150QC. Additional electrostatic lenses are attached from both sides of the quadrupole to help get a better signal of ions. This first mass quadrupole is used to mass-select ions coming from the source chamber.

4.3 Third Chamber (22-pole ion trap)

The third chamber is the central chamber of the machine. Mass-selected ions are guided to the ion trap where they can be stored up to minutes being trapped by rf-fields. The trap shielding is fastened onto the cold-head of a Leybold Cryostat. The cold head is surrounded by a flexible heater plate. The combination of a cold head and heater provides the possibility to vary the temperature in a wide range (7.5-300K). General Valve Series 99 is attached to opposite side of the cold-head. It gives the possibility to have short and intense pulses of neutral gases which are directed in to the trap to make complexes or for studying laser induced charge transfer processes. Trapped ions are probed by laser radiation. Products, which are produced by a laser,

are mass analysed by a quadrupole mounted in the fourth chamber. 3D plan of the trap in detail is depicted in *Figure 4.3.I*.

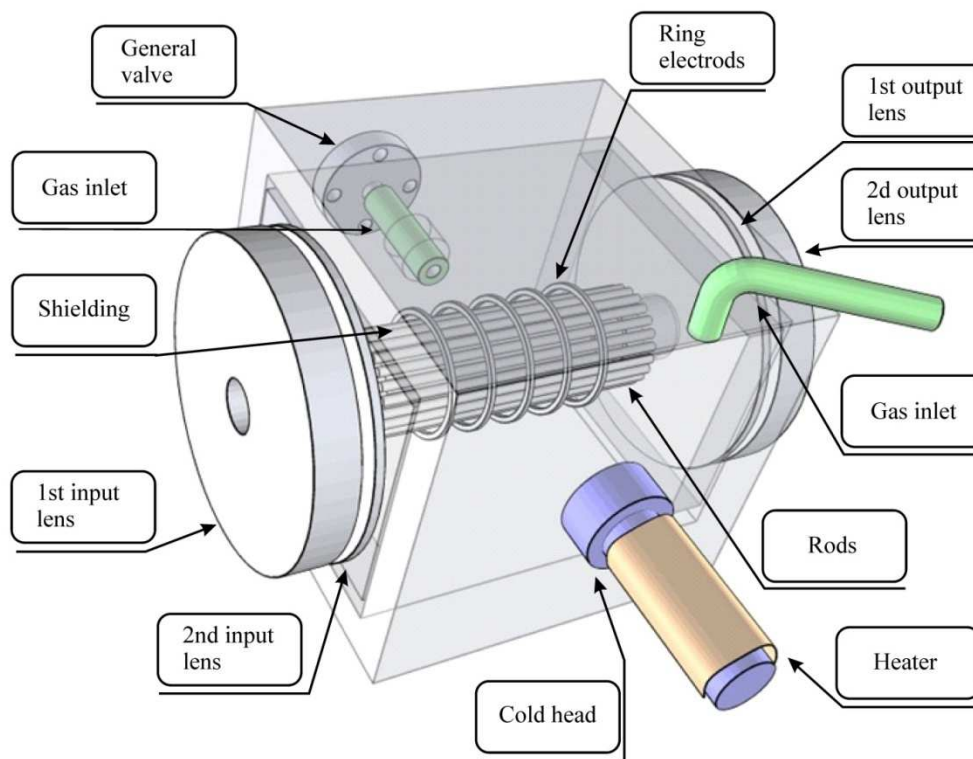


Figure 4.3.I. Detailed view of the third chamber with the 22- pole ion trap.

4.3.1 22-pole ion trap

The 22-pole ion trap was built based on the design of Gerlich [76], consisting of 22 stainless steel rods (1 mm diameter, 36 mm length) equally spaced on an inscribed radius of 10 mm. The described geometry derives from the equation:

$$R = \frac{r_0}{n - 1}$$

where R: rod radius; r_0 : inner radius of the rod arrangement or the so-called trap radius and $2n$: the number of rods. The 22-pole trap is made almost entirely out of copper. Two flat pieces of copper on each side have arrays of 11 holes drilled into them. Rods were finally press-fitted into them. The rods were cooled to low temperature and at the same time the copper was heated up.

Soon after the rods were quickly inserted into the copper pieces, so that when the copper cools, they are rigidly held in place all the time. In *Figure 4.3.1.I*, it is clearly seen that the rods are only supported on one end. The copper holders are electrically insulated from the copper trap housing by thin sapphire (Al_2O_3) plates, which have no electrical conductance but have a relatively high heat transmission. Indium foil was placed between the sapphire and copper edges to provide optimal thermal contact.

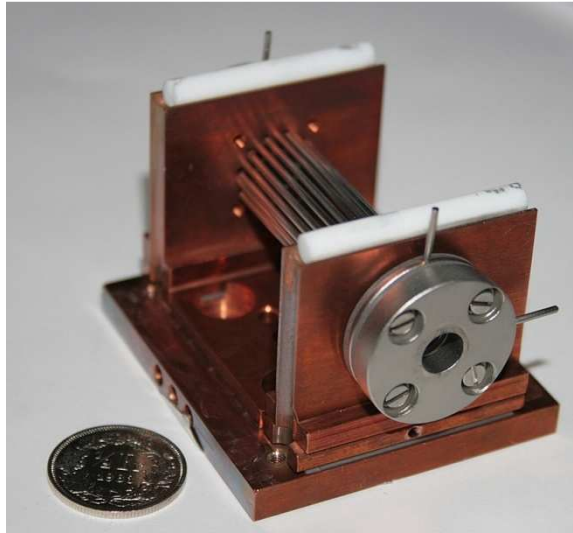


Figure 4.3.1.I. Picture of the actual 22-pole ion trap.

The rod assembly is enclosed by a Π -shaped copper cover. The cover is screwed down onto the trap housing to enclose the box and prevent gas from escaping quickly. It is electrically isolated from the oscillating voltage of the endplates by the long cylindrical ceramic insulators that fit into the hemi-cylindrical grooves.

The copper box that contains the 22-pole trap is mounted on the second stage of a helium cryostat and is additionally surrounded by a heat shield of highly polished aluminium that is bolted to the first stage of the cold-head. This shield is closed on all sides in order to avoid radioactive heat transfer from the Black-body radiation of the room-temperature chamber walls.

4.3.2 Cryostat

A Leybold COOLPOWER 5/100 cold-head is used, which can provide 6 W of cooling power at 20 K and 100 W at 80 K. The cold-head is powered by a Leybold COOLPAK 6000

compressor unit. A thin foil of indium conducts heat between the trap housing and the cold head. Electrical connection wires are precooled on the first stage of the cryostat to a temperature of 40 K before attachment to the trap. To measure the temperature of the trap, a calibrated silicon diode is mounted at the base of the 22-pole trap housing. The lowest temperature achieved is around 7.5 K. The ion trap moves by about 3 mm when cooled down to 8 K due to thermal contraction of the cold-head. Thus, the cold-head has to be on a translatable mount so that it can be aligned when cold. A Linos telescope with cross hairs is used for proper alignment. The cold-head is surrounded by the flexible heater (HK5367R6.4L12A, Minco). The combination of the cryostat and the heater gives the possibility to vary the temperature of ions in the range of 7.5-300 K.

4.3.3 Pulsed-valve

A Parker General Valve Series is used. The valve performs at ultra-high speed (as fast as 2 msec) and delivers repeatable pulses and high repetition rates. It can create a high number density of buffer gas in the trap for a short time. The high pressure of gas can cause three body collisions between ions and buffer gas (e.g. helium) and create ion-helium complexes.

4.4 Fourth Chamber (Mass Filter)

The second (analysis) quadrupole is a Nermag model with 12.5 mm quadrupole diameter, rods operating at 880 kHz with a mass range of 2000 Daltons. The second quadrupole is depicted in *Figure 4.4.I*. This quadrupole is used to analyze the products created by different means (e.g. laser radiation) in 22- pole ion trap.

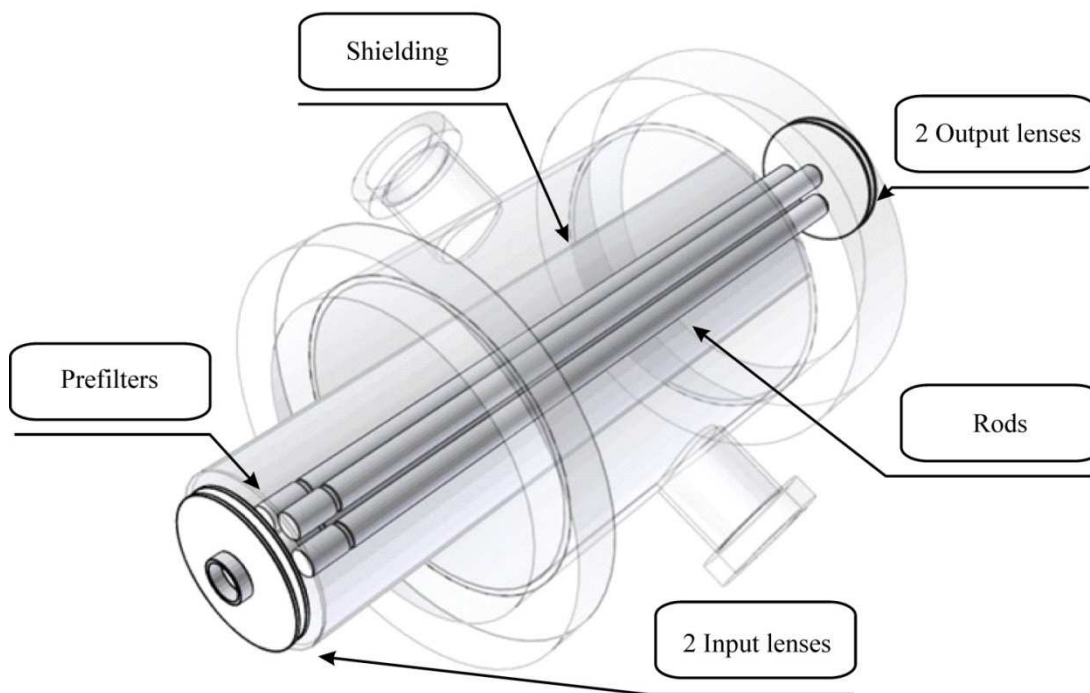


Figure 4.4.I. The fourth chamber: second quadrupole, electrostatic lenses and shielding.

4.5 Fifth Chamber (Daly Detector)

To detect cations a Daly detector is used in fifth chamber. This type of ion detector was introduced by N.R. Daly in 1960. A Daly detector (*Figure 4.5.I*) consists of a conversion dynode, scintillator (BC400 plastic scintillator, 0.5 mm thick, from GC Technology GmbH, Freidling 12 D-84172 Buch am Erlbach) and photomultiplier tube (R647 Hamamatsu PMT).

A critical feature of the scintillator is that it has been coated with a thin aluminum coating (slightly transparent), so that the burst of electrons coming from the dynode must pass through an aluminum coating prior to exciting the phosphor. This has two advantages: firstly, the highly reflective aluminum coating greatly reduces the intensity of scattered laser light that hits the detector, thereby reducing the background signal and secondly, photons emitted from the phosphor that are going in the wrong direction are reflected back to the PMT tube and thereby detected. The scintillator was custom-coated with aluminum by the Department of Materials Science and Metallurgy, New Museums Site, Pembroke Street, Cambridge CB23QZ, UK. The scintillator has a short pulse output of roughly 5 ns.

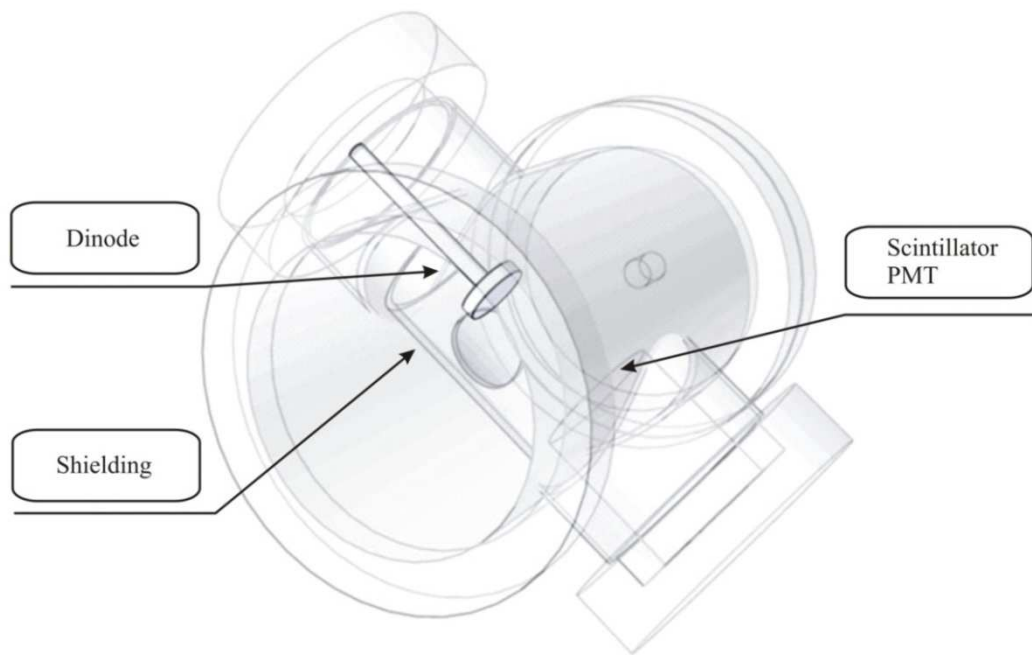


Figure 4.5.I. Daly detector chamber.

The dynode is a highly polished metal knob held at a high negative potential in the range of 20-30 kV, which emits secondary electrons when ions impinge on the surface. The secondary electrons are accelerated onto the scintillator, providing light which is then detected by a PMT. The dynode and PMT are surrounded by a cylindrical grounded shield with two holes which allow both the ion and laser beams to pass through. This shielding can be seen in *Figure 4.5.I*. It is critical so that the high electrical field of the Daly detector does not penetrate into the second quadrupole.

CHAPTER 5

Organization of the Experiment

5.1 Automation of experiment

The automation of the experiment is based on several LabView [77] programmes which are installed on a personal computer (PC). The typical frequency of the experiment is 10 Hz and specified by BNC delay/pulse generator produced by Berkeley Nucleonics Corporation. In the PC three PCI data acquisitions cards are installed. A PCI-6023E by National Instruments and two cards; PCI-DAS6014 and PCI-CTR20HD from the Measurement Computing Corporation. The DAQ cards are used to provide all required analogue voltages, TTL signals and the sequence of pulses of high precision. Detailed description of the PCI-DAS6014 and PCI-6023E cards is written elsewhere [78]. Shortly, PCI-6023E is programmed to be a delay line generator. The sequence of pulses starts when the card gets a trigger pulse from the BNC generator. These are CH1 and CH2 logical channels shown in *Figure 5.1.I*. Channel CH1 is connected to the logical switcher of the power supply of the first quadrupole electrostatic lens. Channel CH2 is connected to the logical switcher of the power supply of trap out. By varying the time width of CH1, the filling time of the trap is changed. The delay time of channel CH2 determines the release time of trapped ions. The difference between the right edge of CH1 logical signal and left edge of CH2 logical signal is the storage time of ions. The pulse width of CH3 determines the detection time and it is the gate of a counter. When an experiment is operated on a base of PCI – 6023E card then CH2 signal is equal to CH3 as this card has two output channels.



Figure 5.1.I. Timing of the experiment.

The PCI-DAS6014 card has several digital to analogue outputs. The outputs are used to tune the first and second quadrupoles to the mass. For that, Nermag mass spectrometer and Mass spectrometer programs were written. The usual way of doing mass spectrometry experiment is as follows. Ions are generated in a source and mass analyzed with second quadrupole when first quadrupole is in guide mode. If there are ions of interest then the first quadrupole is tuned to this mass. Physically ions are eventually detected by a Daly detector, the output of which is sent to a discriminator (Phillips Scientific Model 6904, 300 MHz) and pulse universal counter (HP5316A). The counter has a gate input (CH3), and counts pulses received during the gate. The number of counts is displayed on a front panel as a digital value and is sent to the computer using a GPIB interface. The schematic is depicted in *Figure 5.1.II*.

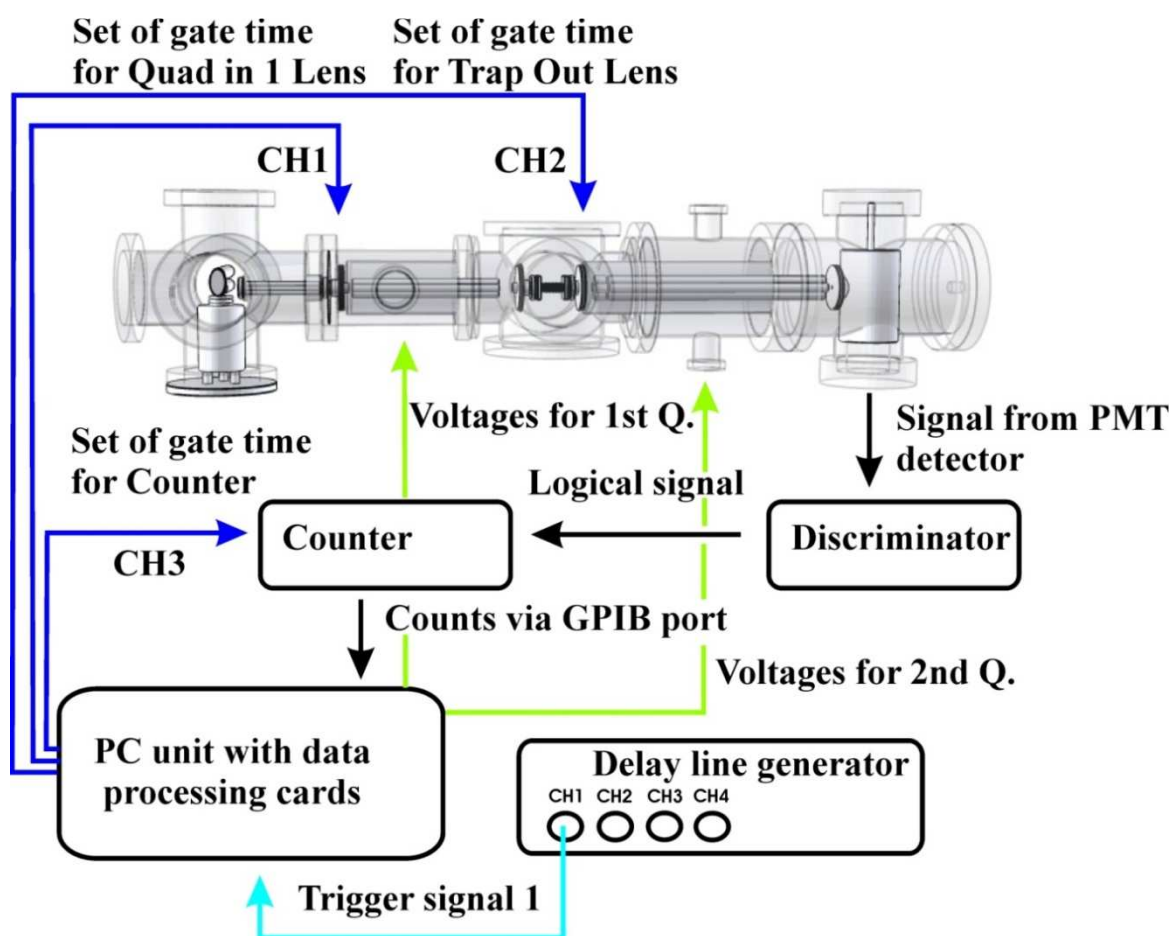


Figure 5.1.II. Base scheme of mass spectrometry experiment.

The typical mass spectrum when the first quadrupole is in a guide mode is shown in *Figure 5.1.III* and in mass select mode is shown in *Figure 5.1.IV*

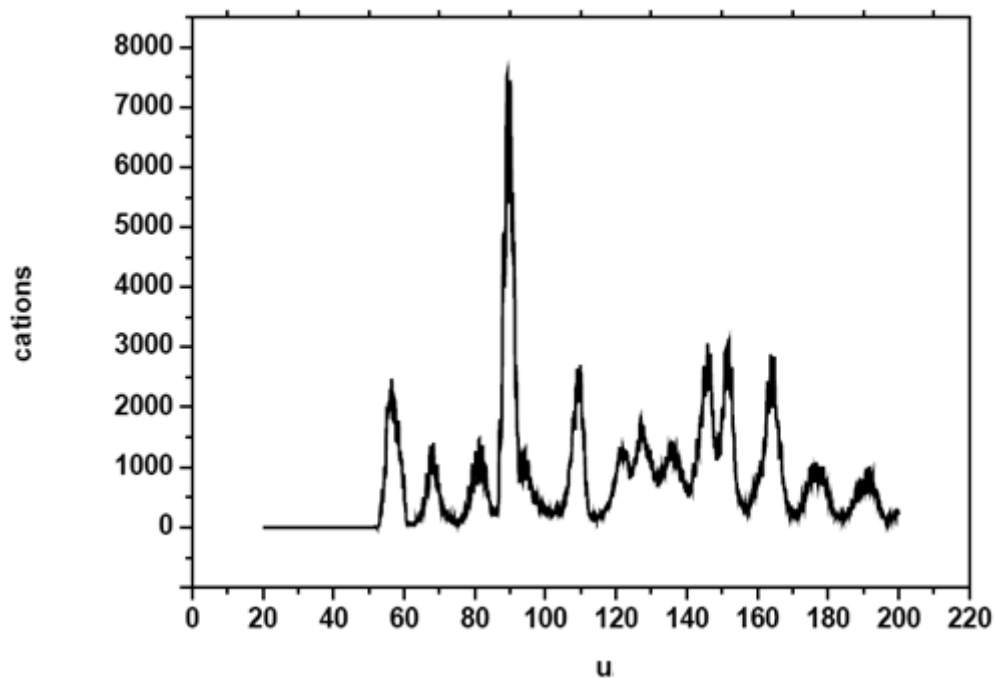


Figure 5.1.III. Typical mass spectrum. First quadrupole is in a guide mode (precursor is naphthalene).

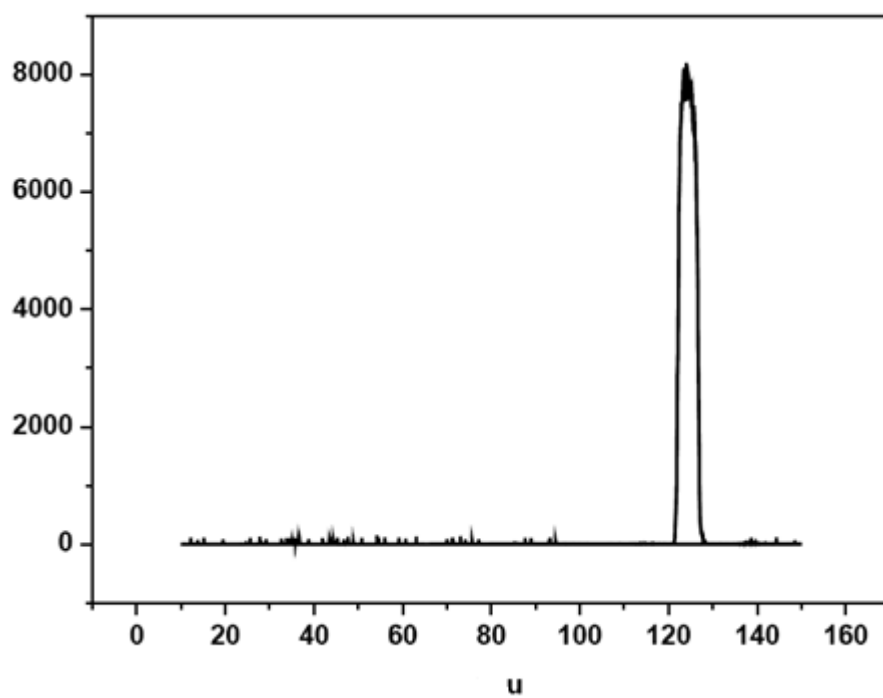


Figure 5.1.IV. Typical mass spectrum. First quadrupole is in a mass select mode (precursor is naphthalene).

5.2 Laser beam alignment

The most convenient way to align any laser beam is with the help of a HeNe laser. This has a good beam profile and intense, visible red radiation. For the alignment at least two optical elements mirrors or prisms, need to be used. The principle scheme of the alignment is depicted in *Figure 5.2.I*. A HeNe laser is fixed on an optical table and the laser radiation with the help of two prisms, which are fixed on optical mounts, is passed through the machine. When the light passes through an apparatus the position of the laser light is fixed with diaphragms. Two diaphragms are put from one side of the machine. These diaphragms are used for the proper orientation of any other laser beam going into the machine. The fine alignment of the laser beam is controlled by the signal of fragments.

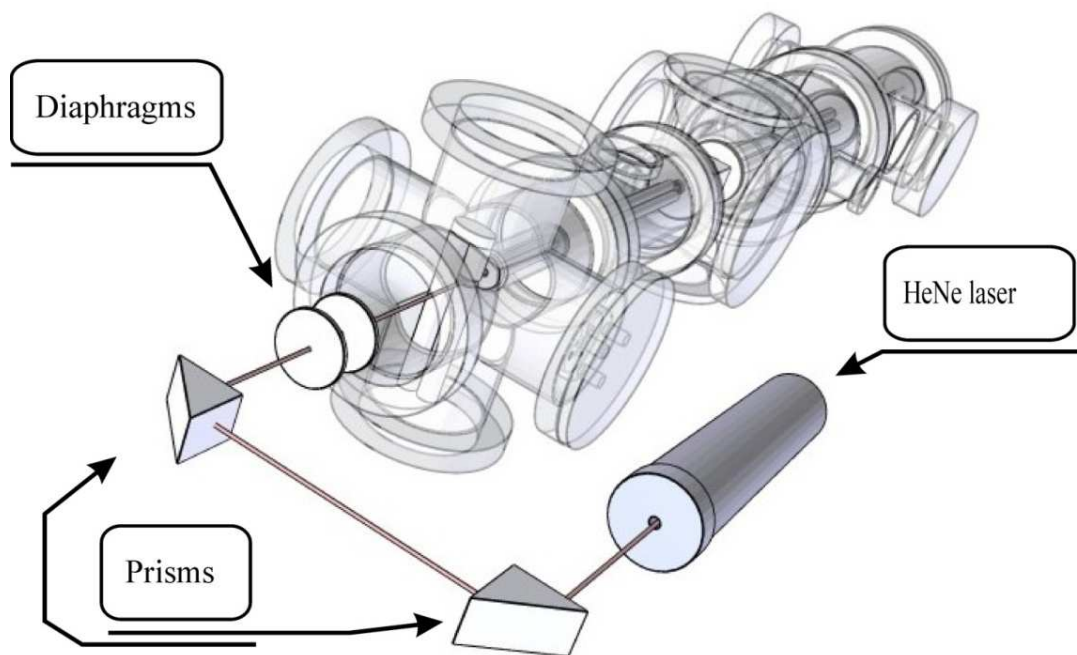


Figure 5.2.I. Scheme of the laser beam alignment.

5.3 Photofragmentation experiments

In photofragmentation experiments a scanning laser is connected to a PC via a RS232 port. If the laser is too far away from PC, the connection is based on optical fibre (*Figure 5.3.I*), reducing interference from parasitic electrical signals present in a laboratory.

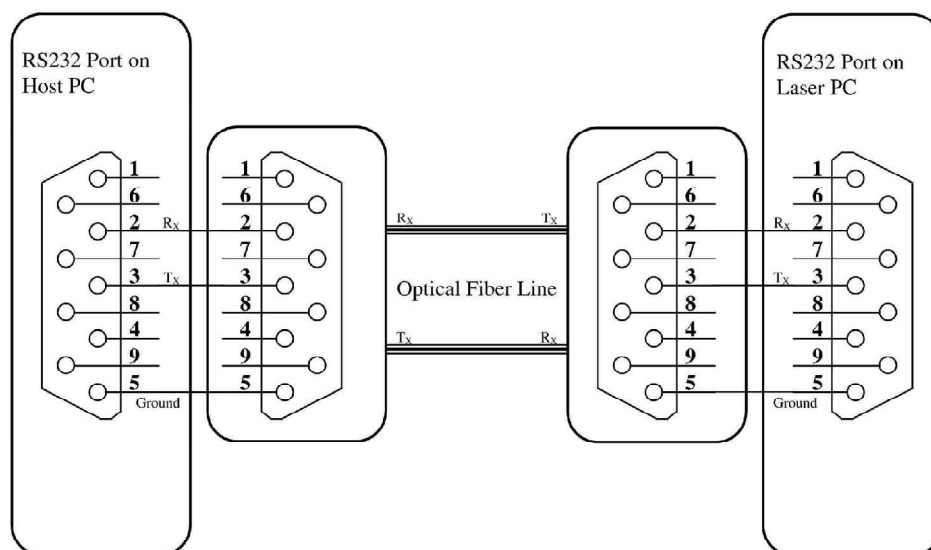


Figure 5.3.I. RS232 connection of laser and PC with an optical fibre line.

For each laser used, a different program is written. Mainly all the lasers have the similar communication protocol via RS 232. For synchronising the setup and laser shots, an additional channel from the delay line is used for one laser and two channels for two lasers. The delay time between laser shots interacting with the ion cloud is monitored by a photodiode connected to an oscilloscope. The ions of interest are mass selected with the first quadrupole and the second quadrupole is tuned to the fragments. The timing of a one-colour experiment is shown in *Figure 5.3.II*.

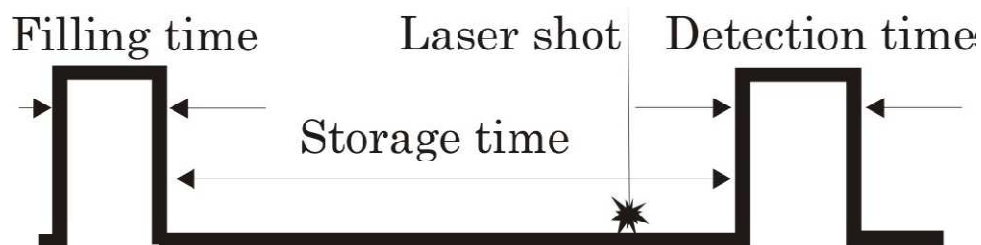


Figure 5.3.II. The timing of one-colour experiment.

The scheme of a one-colour experiment is depicted in *Figure 5.3.III*.

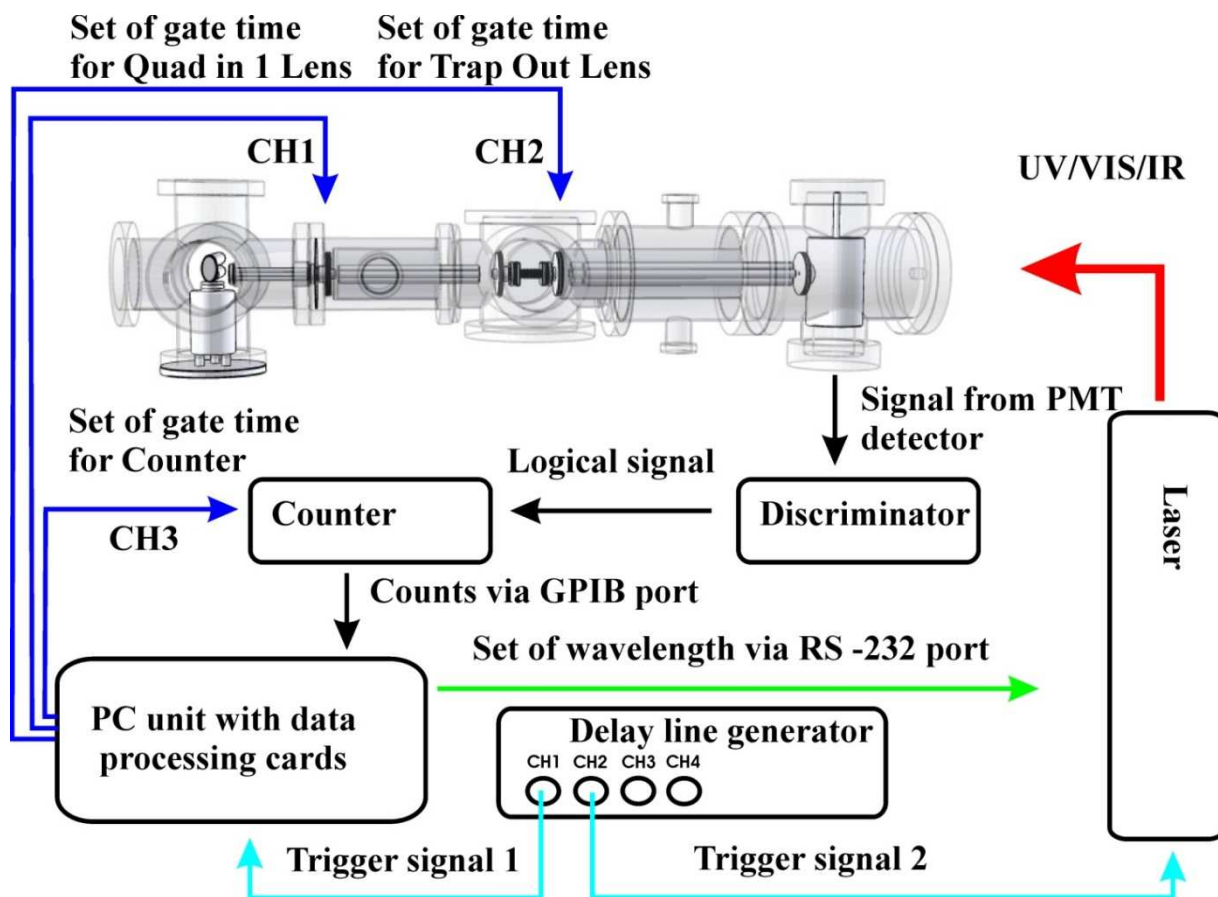


Figure 5.3.III. Scheme of one-colour experiment.

In order to synchronise two colours in time, one should use one more additional channel from the delay line generator. The overlap in time of two colours is checked with the photodiode and an oscilloscope. The timing of a two-colour experiment is depicted in *Figure 5.3.IV*. The automation of a two-colour experiment is shown in *Figure 5.3.V* and *5.3.VI*. The difference between the two schemes is that in the first, mixing mirror is used. The mixing mirror has several disadvantages, using a mirror reduces the power going to the machine. The high reflection coating of a mirror can be used in about 5-10 nm spectral range, meaning one should change the mirror if a scan takes more than 10 nm.

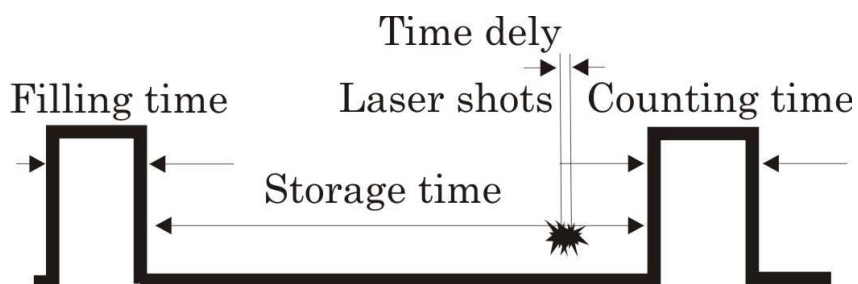


Figure 5.3.IV. Timing for a two-colour experiment.

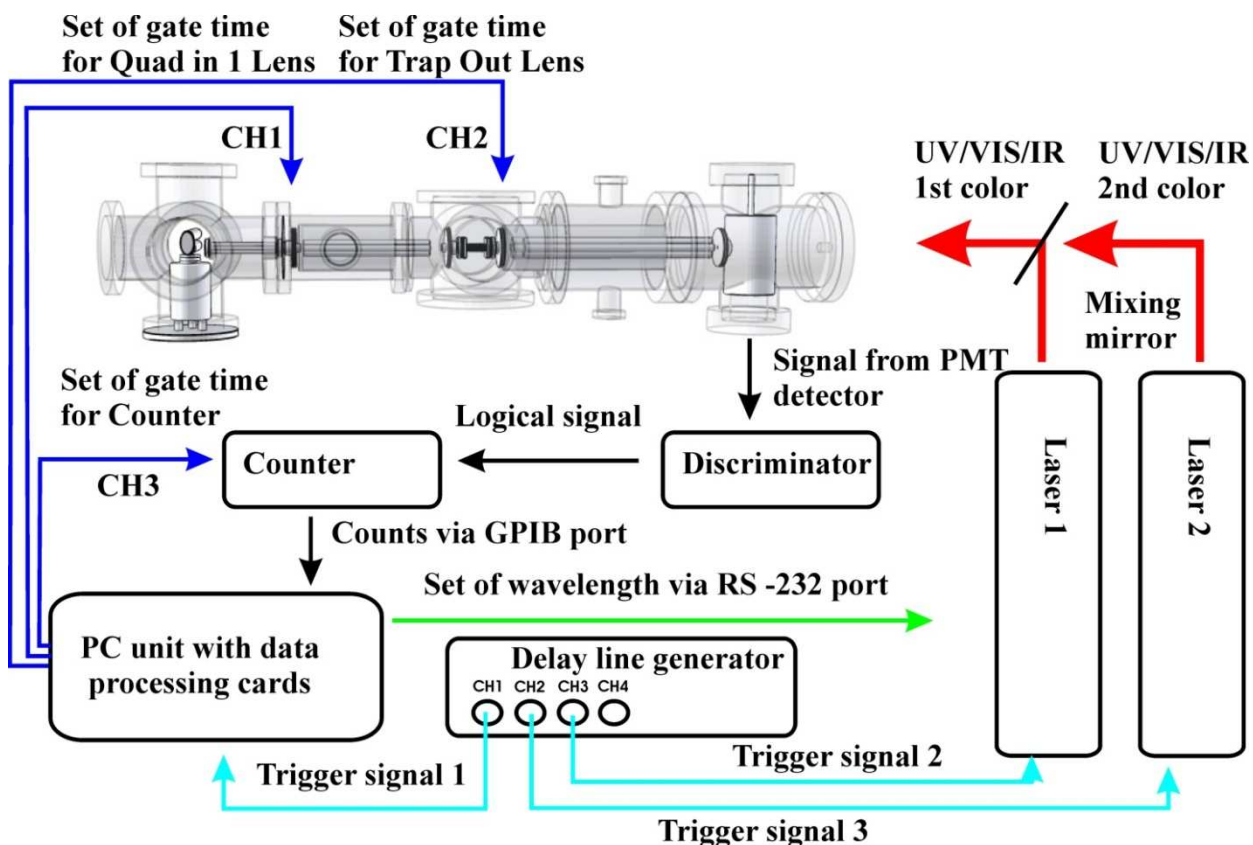


Figure 5.3.V. Scheme of a two-colour experiment, mixing mirror is used.

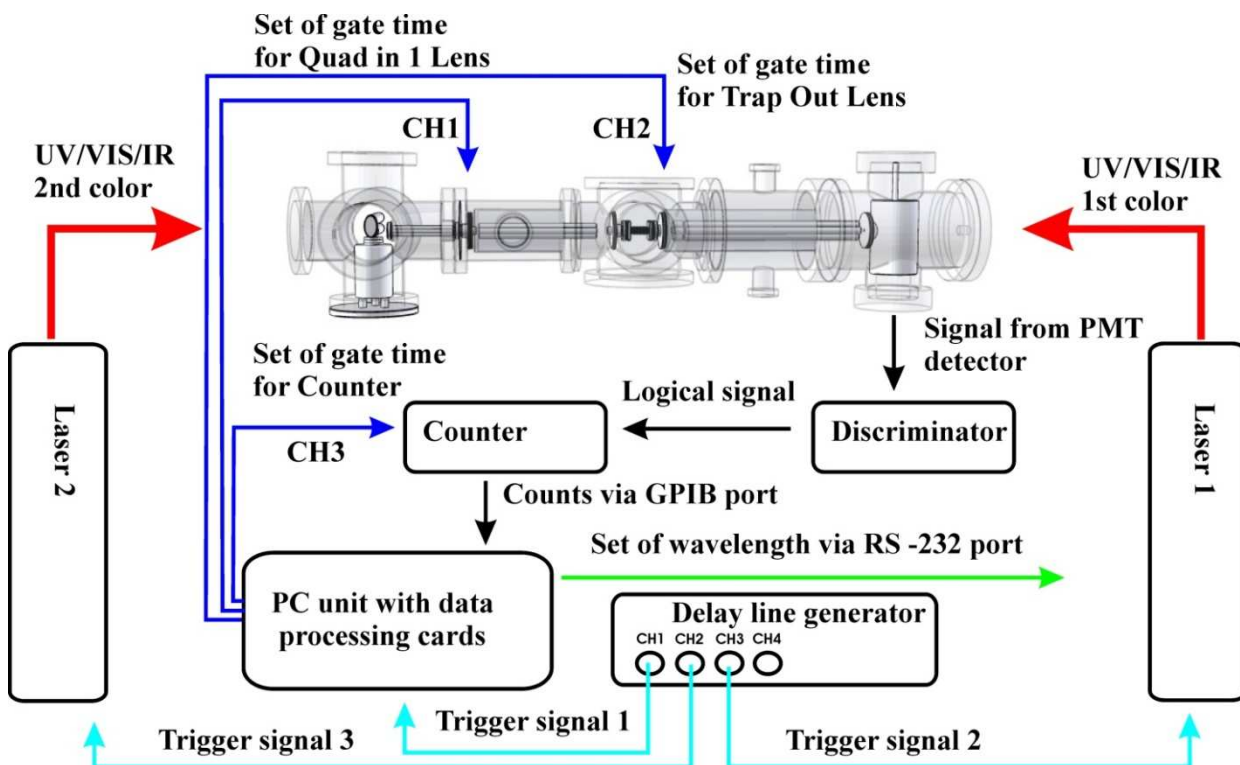


Figure 5.3.VI. Scheme of a two-colour experiment, mixing mirror is not used.

CHAPTER 6

Results and Discussion

Within the cold environment of a 10 K 22-pole ion trap, the rotational, vibrational and translational temperatures should be equilibrated. Different diagnostics can be performed to ensure that this holds true. The rotational profile of a cation of interest can be simulated to show that the rotational temperature of the ions is in the range of 15-25 K. The intensity of hot bands from low vibrational modes of cations can be probed to make sure that the vibrational temperature is in equilibrium with cryogenically cooled buffer gas. Doppler broadening of spectral lines can be measured to look at the translational temperature of the system. In the following section 6.1 the rotational profile of N_2O^+ was examined to determine the rotational temperature.

6.1 1_0^2 band , $\text{A}^2\Sigma^+ \leftarrow \text{X}^2\Pi_{3/2}$ transition, N_2O^+

The electronic spectrum of N_2O^+ cation was chosen to probe the rotational temperature of the ions within this trap. N_2O^+ has been investigated before by optical emission [79], lifetime [80] and photodissociation studies [81-83]. The 1_0^2 band of the $\text{A}^2\Sigma^+ \leftarrow \text{X}^2\Pi_{3/2}$ transition of N_2O^+ has molecular constants $B'' = 0.41157 \text{ cm}^{-1}$, $D'' = 0.2985 \cdot 10^{-6} \text{ cm}^{-1}$, $q'' = 1.13 \cdot 10^{-3} \text{ cm}^{-1}$, $A'' = 132.434 \text{ cm}^{-1}$, $B' = 0.42893 \text{ cm}^{-1}$, $D' = 0.2855 \cdot 10^{-6} \text{ cm}^{-1}$ and $\gamma'' = 7.0 \cdot 10^{-4} \text{ cm}^{-1}$ [81-82]. Simulations were performed using *PGopher* [84] and the rotational temperature was varied as the only parameter. The best agreement with the experiment could be achieved for a rotational temperature $T_{\text{rot}} = 15\text{-}25 \text{ K}$, see *Figure 6.1.1*.

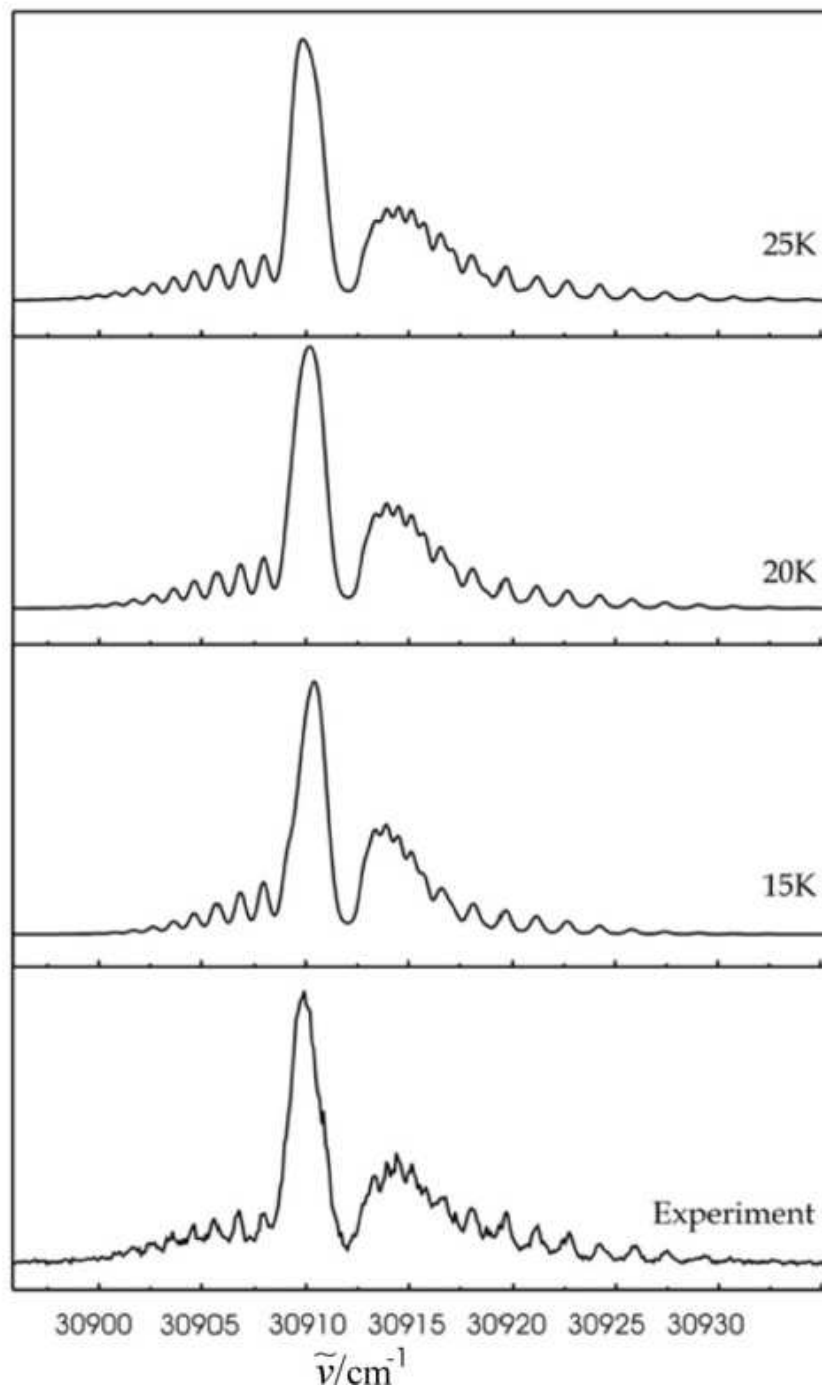


Figure 6.1.1. Rotationally resolved electronic spectrum and simulations of 1_0^2 band of $A^2\Sigma^+ \leftarrow X^2\Pi_{3/2}$ electronic transition, N_2O^+ cation.

6.2 Electronic Transitions of Polyacetylene Cations

6.2.1 Introduction

In spite of the fact that significant progress in interstellar chemistry was achieved and many interstellar molecules were discovered, a new spectroscopic problem appeared early in the 20th century which still remains elusive [6-7]. Along with the identified atomic and molecular electronic absorptions since then, more than 300 of such bands, whose origin remains unclear, were discovered which are called the Diffuse Interstellar Bands (DIBs) for their broadness compared to sharp lines arising from atomic and diatomic species in space [8-10]. In this chapter, electronic absorption spectra of polyacetylene cations are presented. These are considered as molecules of astrophysical relevance, having absorptions within the visible region.

6.2.2 Motivation

Carbon chains were proposed as carriers of DIBs in 1977 by Douglas [18]. In 1993 this idea was extended to the family of polyacetylene chains [20]. Indeed, more than 100 molecules which have been detected in the interstellar medium or circumstellar shells contain carbon and HCCH neutral molecules were detected in the interstellar medium (ISM) [1, 85]. Laboratory studies have shown that for larger polyacetylene chains the ionisation potential decreases with the number of carbon atoms and for large chains is less than 9 eV [86]. As the degree of ionization in interstellar clouds can be large, it is reasonable to assume that ionic polyacetylene chains exist in ISM as possible carriers of DIBs.

Polyacetylene cations have been investigated in terms of astrophysical relevance for some time [35, 87]. The origin bands of the first excited electronic state in the series from $C_4H_2^+$ to $C_{16}H_2^+$ were studied in the gas-phase [35, 87]; however, rotationally resolved 0_0^0 bands were only obtained for chains up to $C_8H_2^+$. In this series of molecules, the rotational constant B decreases with the number of carbon atoms and for $C_{10}H_2^+$ the origin band was only partially resolved, limited by the bandwidth of the laser [88-92]. In all cases the transitions observed are of the type $(\pi^3\pi^4)A^2\Pi_{g/u}-(\pi^4\pi^3)X^2\Pi_{u/g}$.

The obtained rotational constants B and spin-orbit coupling constants A for the ground $X^2\Pi_{u/g}$ and excited $A^2\Pi_{g/u}$ states are presented in *Table 6.2.2.I*; however, no matches between observed transitions and DIBs have been accounted for in former gas-phase studies.

HC _n H ⁺				
	4	6	8	10
T_0	19722.610(2)	16654.6873(3)	14143.1815(5)	12260.4(5)
B''	0.146888(22)	0.044594(3)	0.019078(9)	0.000988(3)
B'	0.140083(22)	0.043792(3)	0.018867(9)	0.000982(3)
B''/B'	1.049	1.018	1.011	1.007
A''	-33.5(1.9)	-31.40(28)	(-31)	(-31)
A'	-31.1(2.0)	-28.41(28)	(-28)	(-28)
ΔA			3	3

Table 6.2.2.I. Spectroscopic data of polyacetylene cations (HC_nH⁺, n=4-10), where T_0 is given in cm^{-1} , B'' and B' are the rotational constants in cm^{-1} and A'' and A' are the spin-orbit coupling constants in cm^{-1} for the ground and excited states, respectively. Data are taken from Ref. [87]

Ideal candidates of astrophysical relevance for laboratory investigations must be species with strong electronic transitions, having absorptions in the region where DIBs are observed. There is little known about higher excited states of polyacetylene cations in the gas-phase, where some of them lie in the DIB absorption range. Some of these electronic transitions may have strong oscillator strengths as examples of open shell radicals of π - π symmetry which have been explained theoretically [93]. The molecular orbital (MO) diagram involving π - π excitations encountered in the electronic spectra of carbon cation chains is depicted in *Figure 6.2.2.I*. The parity of MOs alternates for the HC_{2n}H⁺ chains, the HOMO is ungerade when n=2,4,6,8.. and gerade when n=1,3,5,7... The first excited electronic transition is $A^2\Pi_{g/u} - X^2\Pi_{u/g}$.

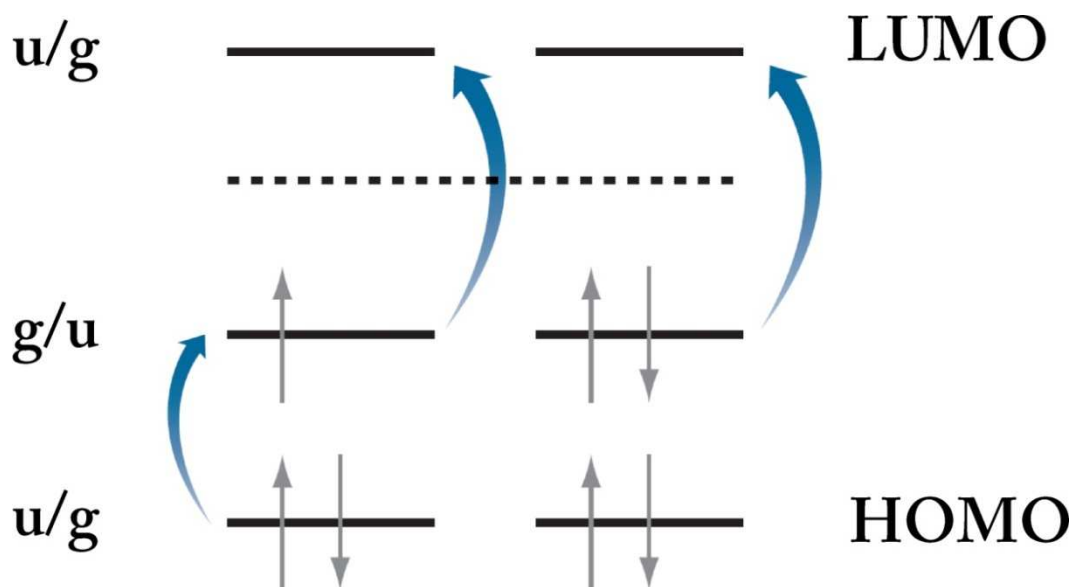


Figure 6.2.2.I. Illustration of the frontier orbitals of the polyacetylene cations. Types of π - π excitations encountered in the electronic spectra of carbon cation chains with g and u parity labels.

The higher excited states of HC_{2n}H^+ cations ($n=2-8$) were studied theoretically [94-97]. Vertical excitation energies (ΔE in eV) and oscillator strengths f using CASPT2 level of theory are depicted in Table 6.2.2.II.

Species	State	Transition	ΔE^a	f^a	ΔE^b	f^b
HC_4H^+	$X^2\Pi_g$	$\dots 1\pi_u^4 1\pi_g^3 2\pi_u^0 2\pi_g^0$	0.00		0.00	
	$A^2\Pi_u$	$1\pi_u \rightarrow 1\pi_g$	2.62	$3.08 \cdot 10^{-2}$	2.65	$3.14 \cdot 10^{-2}$
	$B^2\Pi_u$	$1\pi_g \rightarrow 2\pi_u$	3.93	$2.48 \cdot 10^{-2}$	4.00	$2.43 \cdot 10^{-2}$
	$C^2\Pi_u$	$1\pi_g \rightarrow 2\pi_u$	4.53	$8.98 \cdot 10^{-6}$	4.60	$9.10 \cdot 10^{-6}$
	$D^2\Pi_u$	$1\pi_g \rightarrow 2\pi_u$	5.21	$2.17 \cdot 10^{-2}$	5.29	$2.13 \cdot 10^{-2}$
HC_6H^+	$X^2\Pi_u$	$\dots 1\pi_g^4 2\pi_u^3 2\pi_g^0 3\pi_u^0$	0.00		0.0	
	$A^2\Pi_g$	$1\pi_g \rightarrow 2\pi_u$	2.14	$6.88 \cdot 10^{-2}$	2.17	$7.21 \cdot 10^{-2}$
	$B^2\Pi_g$	$1\pi_u \rightarrow 2\pi_g$	2.99	$4.84 \cdot 10^{-2}$	3.05	$4.81 \cdot 10^{-2}$
	$C^2\Pi_g$	$1\pi_u \rightarrow 2\pi_g$	3.46	$2.17 \cdot 10^{-7}$	3.52	$1.62 \cdot 10^{-7}$
	$D^2\Pi_g$	$1\pi_u \rightarrow 2\pi_g$	3.97	$3.55 \cdot 10^{-2}$	4.03	$3.51 \cdot 10^{-2}$
HC_8H^+	$X^2\Pi_g$	$\dots 2\pi_u^4 2\pi_g^3 3\pi_u^0 3\pi_g^0$	0.00		0.00	
	$A^2\Pi_u$	$2\pi_u \rightarrow 2\pi_g$	1.81	$1.41 \cdot 10^{-1}$	1.83	$1.43 \cdot 10^{-1}$

	$B^2\Pi_u$	$2\pi_g \rightarrow 3\pi_u$	2.40	$3.18 \cdot 10^{-2}$	2.45	$3.10 \cdot 10^{-2}$
	$C^2\Pi_u$	$2\pi_g \rightarrow 3\pi_u$	2.76	$2.98 \cdot 10^{-7}$	2.81	$4.45 \cdot 10^{-7}$
	$D^2\Pi_u$	$2\pi_g \rightarrow 3\pi_u$	3.20	$2.09 \cdot 10^{-2}$	3.25	$2.04 \cdot 10^{-2}$
HC_{10}H^+	$X^2\Pi_u$	$\dots 2\pi_g^4 3\pi_u^3 3\pi_g^0 4\pi_u^0$	0.00			
	$A^2\Pi_g$	$2\pi_g \rightarrow 3\pi_u$	1.52	$1.43 \cdot 10^{-1}$		
	$B^2\Pi_g$	$3\pi_u \rightarrow 3\pi_g$	1.98	$2.79 \cdot 10^{-2}$		
	$C^2\Pi_g$	$3\pi_u \rightarrow 3\pi_g$	2.23	$8.31 \cdot 10^{-6}$		
	$D^2\Pi_g$	$3\pi_u \rightarrow 3\pi_g$	2.60	$2.28 \cdot 10^{-2}$		
HC_{12}H^+	$X^2\Pi_g$	$\dots 3\pi_u^4 3\pi_g^3 4\pi_u^0 4\pi_g^0$	0.00			
	$A^2\Pi_u$	$3\pi_u \rightarrow 3\pi_g$	1.35	$1.88 \cdot 10^{-1}$		
	$B^2\Pi_u$	$3\pi_g \rightarrow 4\pi_u$	1.75	$2.98 \cdot 10^{-2}$		
	$C^2\Pi_u$	$3\pi_g \rightarrow 4\pi_u$	1.98	$5.87 \cdot 10^{-6}$		
	$D^2\Pi_u$	$3\pi_g \rightarrow 4\pi_u$	2.32	$2.21 \cdot 10^{-2}$		
HC_{14}H^+	$X^2\Pi_u$	$\dots 3\pi_g^4 4\pi_u^3 4\pi_g^0 5\pi_u^0$	0.00			
	$A^2\Pi_g$	$3\pi_g \rightarrow 4\pi_u$	1.22	$2.81 \cdot 10^{-1}$		
	$B^2\Pi_g$	$4\pi_u \rightarrow 4\pi_g$	1.65	$4.32 \cdot 10^{-2}$		
	$C^2\Pi_g$	$4\pi_u \rightarrow 4\pi_g$	1.85	$1.32 \cdot 10^{-5}$		
	$D^2\Pi_g$	$4\pi_u \rightarrow 4\pi_g$	2.16	$3.37 \cdot 10^{-2}$		
HC_{16}H^+	$X^2\Pi_g$	$\dots 4\pi_u^4 4\pi_g^3 5\pi_u^0 5\pi_g^0$	0.00			
	$A^2\Pi_u$	$4\pi_u \rightarrow 4\pi_g$	1.10	$3.05 \cdot 10^{-1}$		
	$B^2\Pi_u$	$4\pi_g \rightarrow 5\pi_u$	1.41	$2.59 \cdot 10^{-2}$		
	$C^2\Pi_u$	$4\pi_g \rightarrow 5\pi_u$	1.61	$3.91 \cdot 10^{-4}$		
	$D^2\Pi_u$	$4\pi_g \rightarrow 5\pi_u$	1.82	$1.63 \cdot 10^{-2}$		

Table 6.2.2.II. Vertical excitation energies (ΔE in eV) and oscillator strengths f .

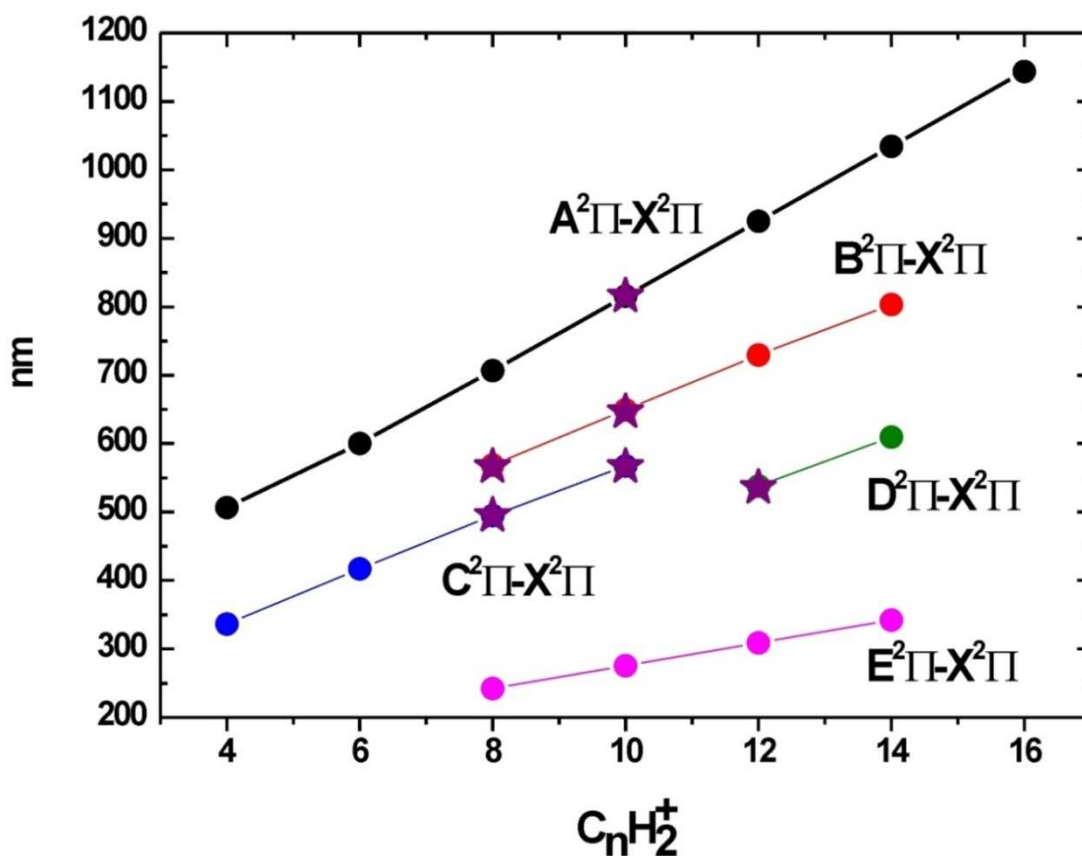
Theoretical values are taken from Ref. [97]

^aCASPT2/cc-pVTZ//RCCSD(T)/6-31G(d, p).

^bCASPT2/cc-pVTZ//RCCSD(T)/cc-pVTZ.

From Table 6.2.2.II it follows that the oscillator strengths of the $B^2\Pi_{g/u} - X^2\Pi_{u/g}$ and $D^2\Pi_{g/u} - X^2\Pi_{u/g}$ electronic transitions are of the same order of magnitude as oscillator strengths of $A^2\Pi_{g/u} - X^2\Pi_{u/g}$, and in case of the $C^2\Pi_{g/u} - X^2\Pi_{u/g}$ transitions they are much

weaker. Recently, transitions to higher excited electronic states of HC_{2n}H^+ ($n=2-8$) were studied in neon matrices at 6 K [98]. The origin band maxima of various polyacetylene cations are summarized in *Figure 6.2.2.II*. The 0_0^0 bands of the $\text{A}^2\Pi - \text{X}^2\Pi$ electronic transition are presented from gas-phase measurements and positions of higher excited states are taken from the matrix studies. Neon matrix shifts are normally less than 1% of the transition energy [99] and were taken into account during spectroscopic studies. In order to ascertain the validity of these transitions as potential DIBs, the corresponding spectra have to be obtained in the gas-phase at low temperature. In the present work, origin bands of the $\text{B}^2\Pi_{g/u} - \text{X}^2\Pi_{u/g}$ electronic transition of C_8H_2^+ , $\text{C}_{10}\text{H}_2^+$, of the $\text{C}^2\Pi_{g/u} - \text{X}^2\Pi_{u/g}$ electronic transition of C_8H_2^+ , $\text{C}_{10}\text{H}_2^+$ and of the $\text{D}^2\Pi_g - \text{X}^2\Pi_u$ electronic transition of $\text{C}_{12}\text{H}_2^+$ were obtained for the first time in the gas-phase at 20 K in an ion trap.



*Figure 6.2.2.II. The origin bands of electronic transitions of polyacetylene cations. The position of the origin bands of the first excited electronic state $\text{A}^2\Pi_{u/g}$ are from the studies made in the gas-phase. Positions of the higher excited electronic states: $\text{B}^2\Pi_{u/g}$, $\text{C}^2\Pi_{u/g}$, $\text{D}^2\Pi_{u/g}$ and $\text{E}^2\Pi_{u/g}$ are taken from neon matrix studies. The states marked with * a star are the objects of investigation in the present work. Data are taken from Refs. [35, 98]*

6.2.3 Experimental

Polyacetylene cations were produced by electron impact ionisation (15-25 eV) of diacetylene gas. A typical mass spectrum of ions produced in the source is depicted in *Figure 6.2.3.I*. To record this spectrum the first mass filter was in a transmission mode. The mass spectrum shows the abundances of carbon cation chains presented in the experiment. Intensities of odd carbon cation chains are weaker than the even ones. The concentration of an ion decreases with increasing number of carbon atoms. Quantitatively, the number of $C_{10}H_2^+$ ions is 300 times less than the number of $C_4H_2^+$ ions. Each mass peak has a fine structure corresponding to $C_nH_3^+$, $C_nH_2^+$, C_nH^+ and C_n^+ ions ($n=4,6,8,10,12$). The most intense mass peak is assigned to the $C_nH_2^+$ species (*Figure 6.2.3.I(b)*). When the cation of interest was mass-selected and all the potentials on the apparatus were optimized, it was possible to trap approximately 3000 cations. Spectra were obtained using a two-colour, two-photon photofragmentation technique. The first colour was tunable radiation from a Nd:YAG pumped dye laser (bandwidth 0.15 cm^{-1}). Ions excited by the first colour were sequentially probed by fixed radiation from an OPO laser (bandwidth 5 cm^{-1}). The pressure of the buffer gas was $\sim 10^{-3}$ mbar. The frequency of the second colour was chosen in a way such that the sum of the frequencies of the first and the second colour exceeded the photofragmentation threshold. For the second colour, photon energies of 5.05, 5.17 eV were chosen for $HC_{2n}H^+$ ($n=4, 6$), respectively. For the $A^2\Pi_g - X^2\Pi_u$ and $B^2\Pi_g - X^2\Pi_u$ transitions of $HC_{10}H^+$, photon energies were 4.35 and 4.68 eV. The overlap in time of the two photons was controlled by a fast photodiode connected to a digital oscilloscope. The overlap in space of the two laser beams was established using diaphragms, and the alignment was optimised by maximizing the fragment signal. After resonant excitation dissociated products were released from the ion trap by lowering the exit potential. The second quadrupole was tuned to a fragment mass and the resolution was decreased to collect the signal from all daughter ions corresponding to loss of C_3 , C_3H and C_3H_2 . Spectra were obtained by monitoring the yield of fragment cations by a Daly detector while the first colour was scanned over the transition. In order to avoid saturation, the laser power was reduced to less than $100\text{ }\mu\text{J}$.

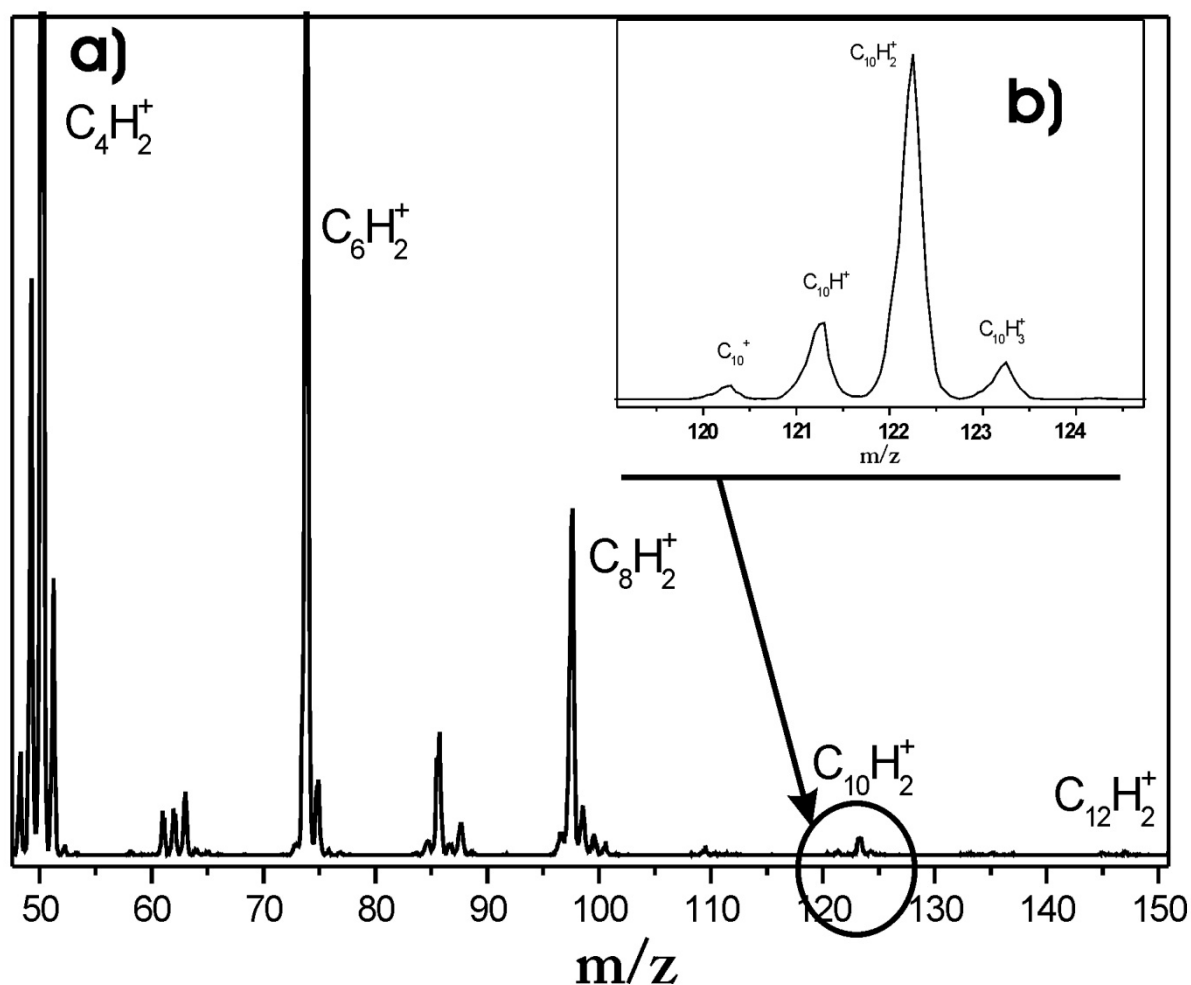


Figure 6.2.3.I. a) Mass spectrum of ions created by electron impact ionization of diacetylene. b) Fine structure of the mass peak, in the mass range of 118-126 m/z (corresponding to the C_{10}^+ , $C_{10}H^+$, $C_{10}H_2^+$ and $C_{10}H_3^+$ cations). The calibration of the mass spectrum is shifted by 0.32 m/z .

6.2.4 $A^2\Pi_g - X^2\Pi_u$ transition of $C_{10}H_2^+$

The observed origin band of the $A^2\Pi_g - X^2\Pi_u$ transition of $C_{10}H_2^+$ cation is depicted in Figure 6.2.4.I. The dashed line represents the simulation of the origin band at 20 K performed with *PGopher* [84]. In the simulation the Lorentzian contribution was set to 0.45 cm^{-1} .

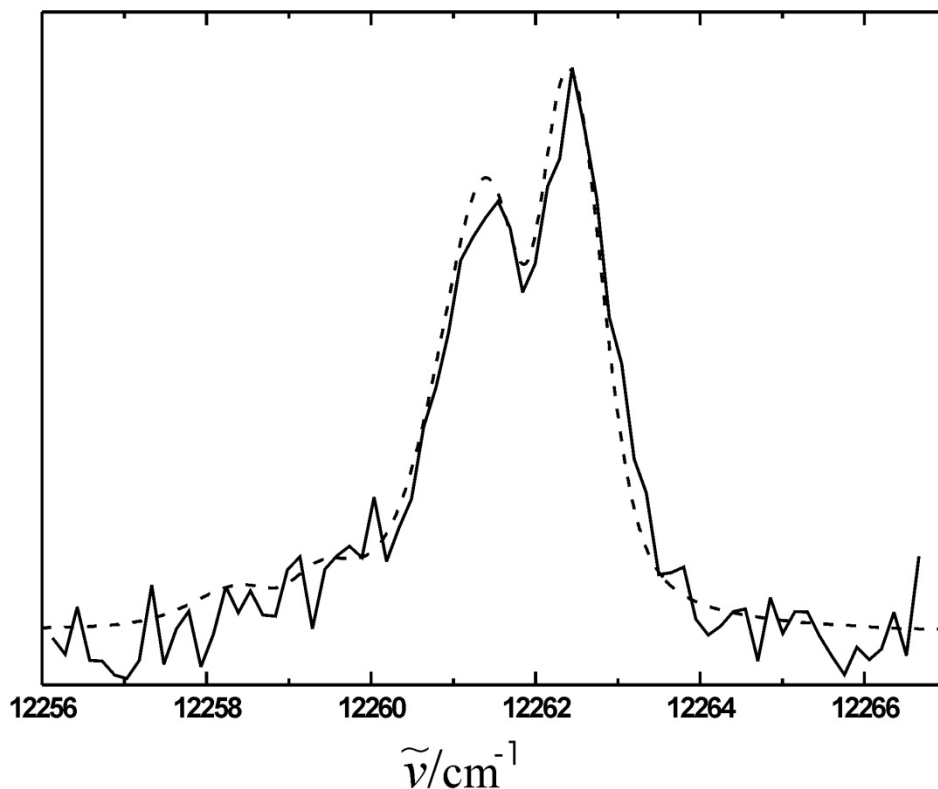


Figure 6.2.4.I. Experimental spectrum and simulation (dashed line) of the origin band of the $A^2\Pi_g - X^2\Pi_u$ transition of $C_{10}H_2^+$ at 20 K, where the Lorentzian contribution to the linewidth is 0.45 cm^{-1} .

The observed origin band could not be rotationally resolved with the present laser bandwidth. Two spin-orbit components $^2\Pi_{1/2} - ^2\Pi_{1/2}$ and $^2\Pi_{3/2} - ^2\Pi_{3/2}$ are expected, where the intensity ratio depends on the initial population in the ground state. The separation between two $\Omega'=\Omega''=3/2$ and $\Omega'=\Omega''=1/2$ is the difference between two spin-orbit constants in the ground and excited states ($\Delta A=-3\text{ cm}^{-1}$). Since the LUMO is more than half-full in the $X^2\Pi(\pi^4\pi^3)$ and $A^2\Pi(\pi^3\pi^4)$ states, the spin-orbit component with $\Omega=3/2$ is lower in energy. Based on thermal population at 20 K, the expected relative intensity of the transitions originating from $\Omega'=1/2$ are about 18% as compared to $\Omega'=3/2$. As a consequence, the $^2\Pi_{1/2} - ^2\Pi_{1/2}$ transition is hidden under the unresolved P branch of the more intense $^2\Pi_{3/2} - ^2\Pi_{3/2}$ transition but is partially responsible for the shoulder observed near 12259.4 cm^{-1} , which lies $\sim 3\text{ cm}^{-1}$ to the red. Simulations at different temperatures are presented in Figure 6.2.4.II using the rotational constants reported in Ref. [87].

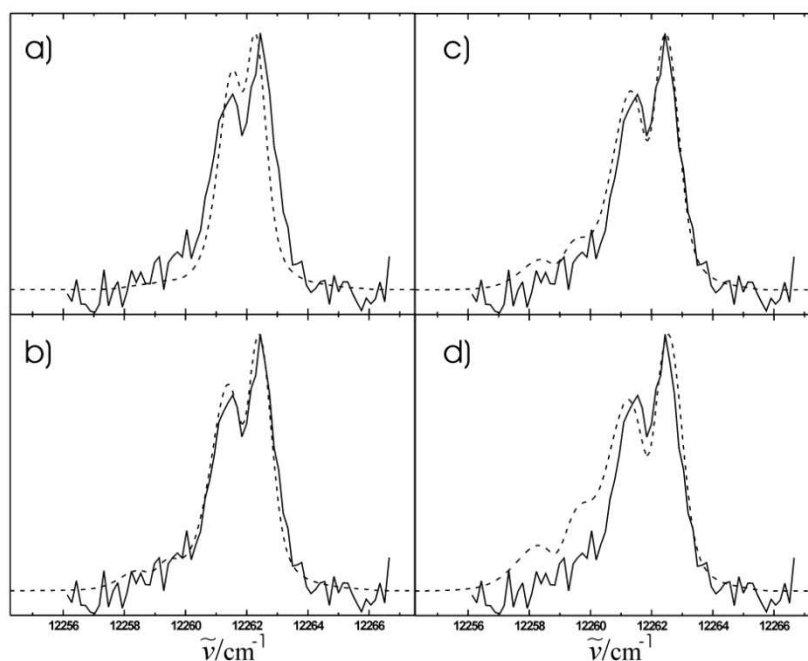


Figure 6.2.4.II. Experimental spectrum and simulation (dashed line) of the origin band at different temperatures, with Lorentzian contribution to the linewidth is 0.15 cm^{-1} . The simulations in a), b), c) and d) were performed using the temperatures of 10, 15, 20 and 25 K, respectively.

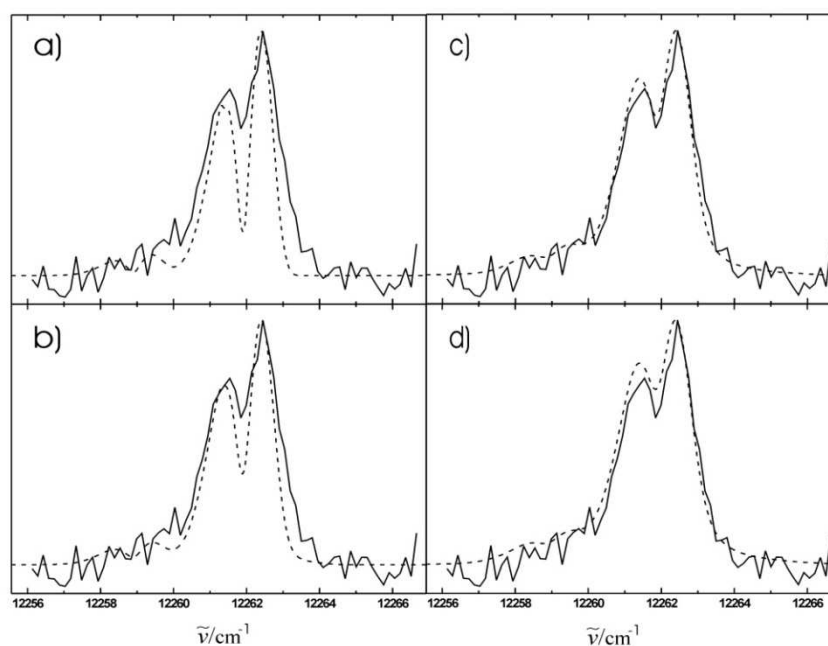


Figure 6.2.4.III. Experimental spectrum and simulation (dashed line) of the origin band with different Lorentzian contribution. In all spectra the Gaussian contribution is 0.15 cm^{-1} (bandwidth of laser) and Lorentzian contribution is a) 0.0 , b) 0.15 , c) 0.45 and d) 0.55 cm^{-1} . The temperature is 20 K.

By using *PGopher* it is possible to simulate the rotational structure of the transition with both Lorentzian and Gaussian contributions. In the experiment the resolution of laser used was 0.15 cm^{-1} . From simulations it was concluded that the different temperatures effect the full width at half maximum (FWHM) of the origin band. At the same time the dip between observed P and R branches is almost determined by the Lorentzian contribution to the origin band, see *Figure 6.2.4.III*. At the Lorentzian contribution 0.45 cm^{-1} the simulated dip is matched with experimental one and Gaussian contribution does not effect the simulated origin band, i.e. when the Lorentzian contribution is 0.45 cm^{-1} it does not matter if the Gaussian contribution is 0 cm^{-1} or the laser bandwidth used (0.15 cm^{-1}). The last fact leads to the conclusion that experimentally observed spectrum is not power broadened and the rotational temperature is in the range of 15-25 K. Indeed, at 10 K the FWHM of the simulated origin band is less than in the experiment. The relative intensity of the $\Omega''=1/2, \Delta\Omega=0$ band is about 0.1% of the $\Omega''=3/2$ component. However, the experimental spectrum exhibits a small absorption feature at this position. At ca. 20 K the fitted origin band matches the experimental one; but S/N ratio in the experimental spectrum does not allow a clear determination of the temperature more accurately than within 5 K and the FWHM of the origin band is about 2.2 cm^{-1} .

The laser power used to observe $A^2\Pi_g - X^2\Pi_u$ electronic transition was less than 100 μJ . The same power of the lasers was used for all measurements. Therefore, it is believed that all the other origin bands are free of power saturation and FWHMs present the natural bandwidths. Thus, the bands can be comparable with absorption features of astrophysical relevance directly.

6.2.5 $E^2\Pi_g - X^2\Pi_u$ transition of $\text{C}_{10}\text{H}_2^+$

The spectrum obtained for the $E^2\Pi_g - X^2\Pi_u$ transition of $\text{C}_{10}\text{H}_2^+$ in an ion trap is presented in *Figure 6.2.5.I*. The broad spectrum presented in *Figure 6.2.5.I(c)* is a spectrum obtained in a neon matrix at 6 K [98]. The most intense band is located at 275 nm. The shift between the most intense band obtained in the ion trap and in a neon matrix is about 650 cm^{-1} (matrix shift). Taking into account this shift, the two spectra were superimposed in *Figure 6.2.5.I(b)*. The weak transition of the matrix spectrum is matched with the 255 nm transition and the shoulder of the intense broad peak is matched with the transition at 275 nm.

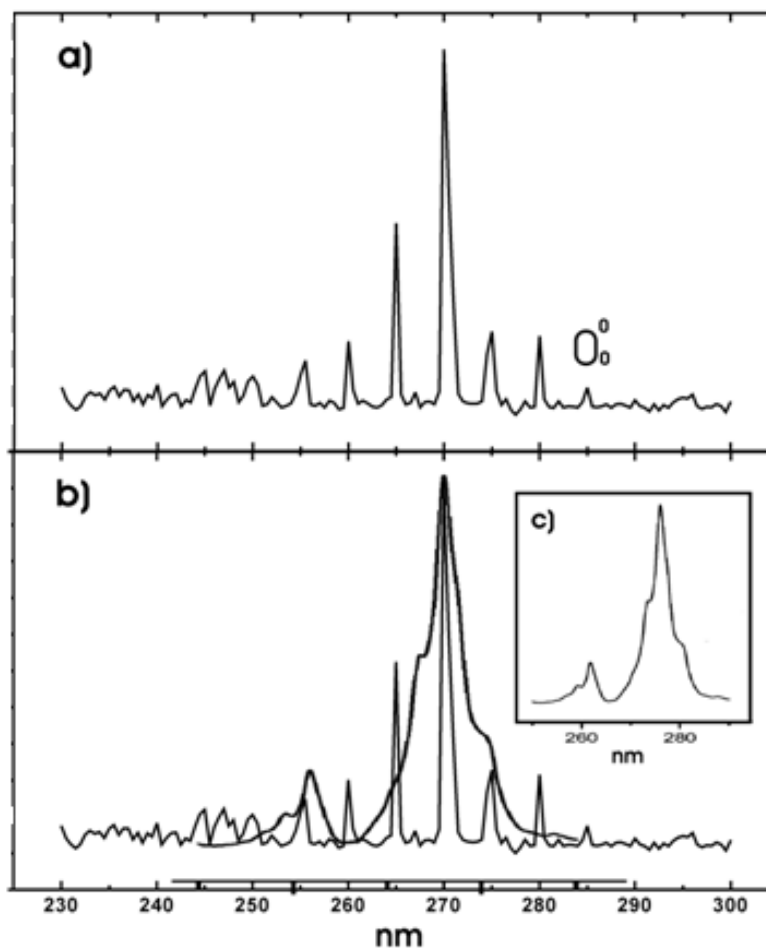


Figure 6.2.5.I. a) The $E^2\Pi_g - X^2\Pi_u$ transition of $C_{10}H_2^+$ with the assigned origin band at 20 K. b) spectrum in a) superimposed by the spectrum obtained in a neon matrix and c) spectrum observed in a neon matrix (taken from Ref. [98]).

The spectrum obtained in the ion trap shows vibrational structure in the $E^2\Pi_g$ state where the most intense peak was detected at 270 nm. This peak cannot be assigned to the origin band of $E^2\Pi_g - X^2\Pi_u$ electronic transition as there are bands located towards the red, separated by $\sim 650\text{ cm}^{-1}$. Trapped ions have a temperature of approximately 20 K, hence these transitions cannot be hot bands from vibrational levels in the ground electronic state populated at this temperature. In addition, these absorption features cannot be assigned to highly excited vibrations of the $D^2\Pi_g$ electronic state of $C_{10}H_2^+$ cation due to the energy separation between the $D^2\Pi_g$ and $E^2\Pi_g$ states. Although the position of the $D^2\Pi_g - X^2\Pi_u$ transition is not known, it is possible to estimate the energy of $D^2\Pi_g$ state. Indeed, for linear carbon cation chains the positions of the origin bands are approximately linearly dependent on the number of carbon atoms in a molecule [97]. Using the positions of the origin bands of the $D^2\Pi_{g/u} - X^2\Pi_{u/g}$ electronic transition of $C_{12}H_2^+$ and $C_{14}H_2^+$ known from studies in neon matrices at 6 K [98], the

position of the origin band of the $D^2\Pi_g$ state of $C_{10}H_2^+$ cation can be estimated to be ~ 450 nm corresponding to 22222 cm^{-1} . Thus, two electronic states $D^2\Pi_g$ and $E^2\Pi_g$ are separated by $\sim 14000\text{ cm}^{-1}$.

Vibrational frequencies of higher excited electronic states do not differ much from calculated ones for the ground state, i.e. the geometry of the species do not change much for $D^2\Pi_g$ and $A^2\Pi_u$ states [98]. Therefore, the calculated 14000 cm^{-1} separation is believed to be too big to have a good Franck-Condon overlap of the totally symmetrical wave function in a ground state with highly excited vibrations of $D^2\Pi_g$ state. Thus, it is assumed that the observed weak transition at 285 nm is the origin band and the weakness of this band can be explained by a small Franck-Condon factor with a significant geometry change of the molecule in the $E^2\Pi_g$ excited state. Therefore, the vibrational assignment of the $E^2\Pi_g - X^2\Pi_u$ transition of $C_{10}H_2^+$ was not possible based on the ground state frequencies.

6.2.6 $B^2\Pi_g - X^2\Pi_u$ transition of $C_{10}H_2^+$

The searches of the origin bands were based on matrix data. The band position is known with uncertainty of the matrix shift, which is typically about 1% of the observed transition energy. For the $B^2\Pi_g - X^2\Pi_u$ transition of $C_{10}H_2^+$ located at 15403 cm^{-1} matrix shift is about 150 cm^{-1} . Thus, one has to scan within 150 cm^{-1} around the 15403 cm^{-1} position. If the transition is found, it is necessary to check that this is not a vibrational/vibronic one, i.e. scan towards the red within 150 cm^{-1} . When no other transitions are observed, one can assign the absorption feature to the origin band.

The origin band of the $B^2\Pi_g - X^2\Pi_u$ electronic transition of $C_{10}H_2^+$ is presented in *Figure 6.2.6.I*. The band is split into three components which are separated from the most intense one by 12 cm^{-1} and 22 cm^{-1} , respectively. DFT and CASSF level of theory calculations have been performed using different basis sets (6-311++G(d,p) and TZV) for the ground state. The frequency of the lowest π_u bending mode of the $C_{10}H_2^+$ cation was calculated to be $\sim 40\text{ cm}^{-1}$ (41 cm^{-1} (DFT) and 38 cm^{-1} (CASSF)). Thus, these two features are not likely to be one and double quantum excitation of the lowest vibrational mode. However, the π_u bending mode coupled with $\Pi_{u/g}$ electronic states can be split due to the Renner-Teller effect and transitions arising from these components may appear. Namely, it has been assumed that the most intense

transition can be assigned to the origin band and two absorption features are likely to be ${}^2\Sigma_g^+ \leftarrow {}^2\Sigma_u^+$ and ${}^2\Delta_g \leftarrow {}^2\Delta_u$ dipole-allowed vibronic transitions.

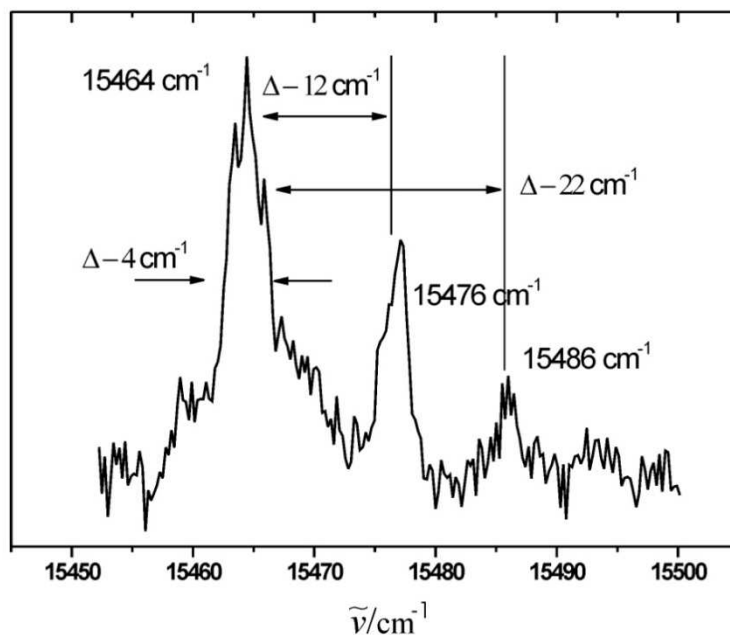


Figure 6.2.6.I. Origin band of the $B^2\Pi_g - X^2\Pi_u$ transition with two absorption features.

6.2.7 Origin bands of electronic transitions:

$C^2\Pi_g - X^2\Pi_u$ ($C_{10}H_2^+$), $B^2\Pi_u - X^2\Pi_g$ ($C_8H_2^+$) and $D^2\Pi_u - X^2\Pi_g$ ($C_{12}H_2^+$).

The origin bands of: $C^2\Pi_g - X^2\Pi_u$ ($C_{10}H_2^+$), $B^2\Pi_u - X^2\Pi_g$ ($C_8H_2^+$) and $D^2\Pi_u - X^2\Pi_g$ ($C_{12}H_2^+$) electronic transitions are presented in Figure 6.2.7.I. The obtained FWHM of the origin band of the $B^2\Pi_u - X^2\Pi_g$ transition of $C_8H_2^+$ is 4 ± 0.5 cm^{-1} . For the $D^2\Pi_u - X^2\Pi_g$ transition of $C_{12}H_2^+$ and $C^2\Pi_g - X^2\Pi_u$ transition of $C_{10}H_2^+$ the FWHMs are 28 ± 2.5 cm^{-1} and 30 ± 2.5 cm^{-1} , respectively. The origin band of $B^2\Pi_u - X^2\Pi_g$ electronic transition of $C_8H_2^+$ is split in two components, which are attributed to rotational P and R branches. The separation is ~ 1.6 cm^{-1} . Although, this separation is barely visible in the spectrum because of the noise in the experiment, it is possible to estimate the rotational temperature by the formula $T = \frac{\Delta\nu^2 hc}{8k_B}$ for linear molecules [100]. This estimate is based on assumption that in the $B^2\Pi_u$ state the geometry of the

molecule does not change significantly. Indeed, the ratio of the rotational constant B' in the excited $A^2\Pi_u$ state to the rotational constant B'' in the ground state $X^2\Pi_g$ is 1.011 (Table 6.2.2.I). For the separation of about 1.6 cm^{-1} and rotational constant B of 0.02 cm^{-1} the calculated rotational temperature is $\sim 23\text{ K}$ ($3 \cdot 10^{10} \cdot 6.6 \cdot 10^{-27} / 1.38 \cdot 10^{-16} / 0.02 \cdot 1.6^2 / 8$), which lies in the range of temperatures expected for the experiments performed in our ion trap. The origin bands of $C^2\Pi_g - X^2\Pi_u$ and $D^2\Pi_u - X^2\Pi_g$ transitions are broad and do not exhibit any fine structure. The bands are not rotationally resolved because of small rotational constants. In addition, lifetime broadening might occur as result of intramolecular processes.

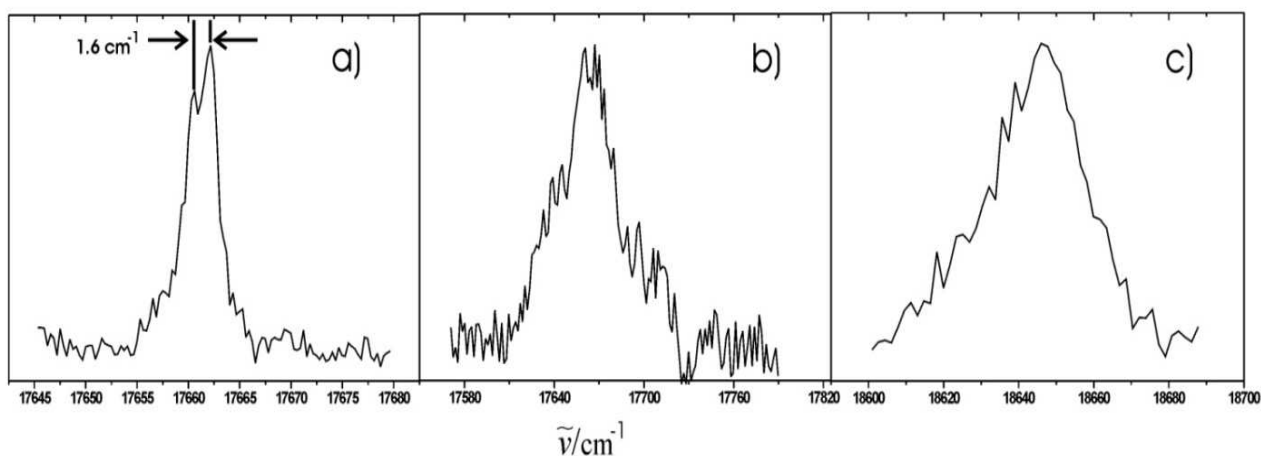


Figure 6.2.7.I. a) Origin band of the a) $B^2\Pi_u - X^2\Pi_g$ transition, $C_8H_2^+$, b) $C^2\Pi_g - X^2\Pi_u$ transition, $C_{10}H_2^+$ and c) $D^2\Pi_u - X^2\Pi_g$ transition, $C_{12}H_2^+$.

6.2.8 $C^2\Pi_u - X^2\Pi_g$ transition, $C_8H_2^+$

The origin band of the $C^2\Pi_u - X^2\Pi_g$ transition of $C_8H_2^+$ is depicted in Figure 6.2.8.I.

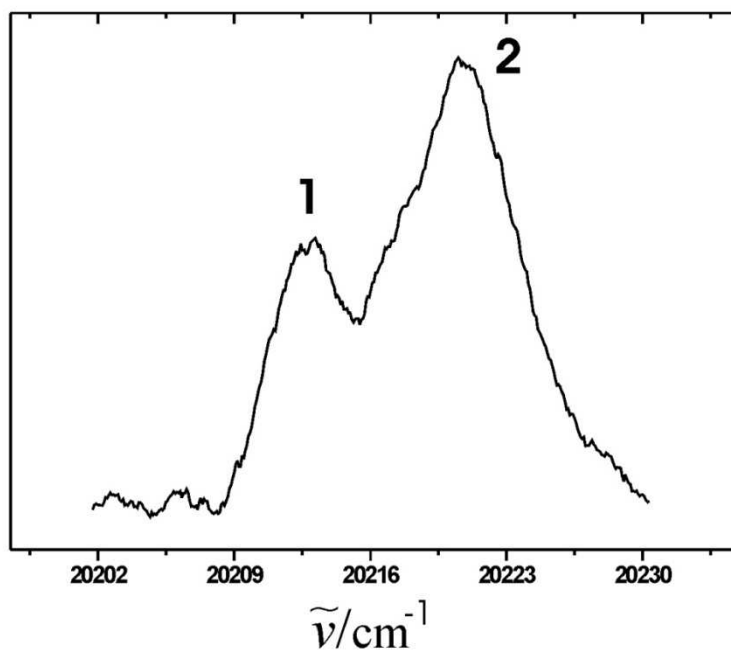


Figure 6.2.8.I. Origin band of the $C^2\Pi_u - X^2\Pi_g$ transition, $C_8H_2^+$.

The origin band of the $C^2\Pi_u - X^2\Pi_g$ electronic transition of $C_8H_2^+$ is split into two components. The separation is $\sim 12\text{ cm}^{-1}$. Although they appear to P and R branches for a linear molecule, this cannot be the explanation; a simple estimate using $\sim 12\text{ cm}^{-1}$ separation and a rotational constant $B \sim 0.02\text{ cm}^{-1}$ leads to the temperature $\sim 1200\text{ K}$ which is not possible. As shown for $C_{10}H_2^+$ the temperature of ions in the trap is in the range of 15-25 K. Very likely the absorption feature lying close to the origin is a highly excited vibration of the $B^2\Pi_u$ electronic state. Indeed, the energies separation of the two electronic states $B^2\Pi_u$ and $C^2\Pi_u$ of $C_8H_2^+$ is only $\sim 2550\text{ cm}^{-1}$ [97-98]. A DFT (6-311++G basis set) normal mode analysis performed for the $C_8H_2^+$ cation for ground state gives 2500 cm^{-1} vibration of σ_g symmetry. For the excited state this frequency is likely to be different and may lie closer to the 0_0^0 band. Thus, the less intense peak is assigned to a vibrational excitation of the $B^2\Pi_u$ state.

6.2.9 Cooling dynamics

The population of the excited state was probed by delaying the length of time between the excitation and fragmentation laser. The obtained decay curves are depicted in *Figure 6.2.9.I*.

The maximum of the signal was detected with 26.31 μs time delay between the VIS and UV lasers for $A^2\Pi_g$ state (Figure 6.2.9.I(a)). The decay constant is $\sim 64 \mu\text{s}$. In contrast, the decay curve obtained for the $B^2\Pi_g$ state appears at a delay of 0 μs with a $\sim 9.1 \mu\text{s}$ decay constant (Figure 6.2.9.I(b)). Uncertainty of the time measurements was about 5 ns.

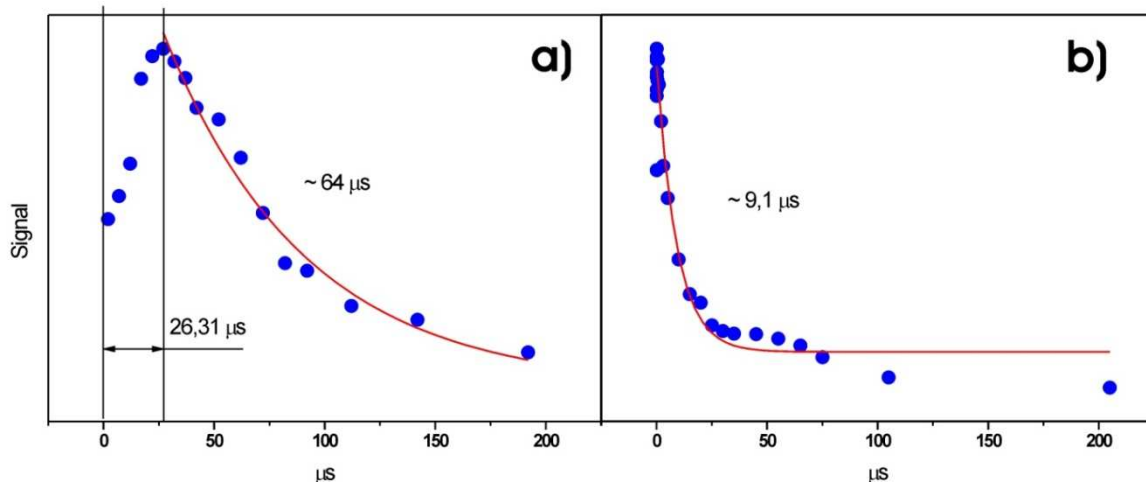


Figure 6.2.9.I. The observed decay curves for a) the origin band of the $A^2\Pi_g - X^2\Pi_u$ electronic transition and b) the 0_0^0 band of the $B^2\Pi_g - X^2\Pi_u$ electronic transition of $C_{10}H_2^+$.

The large polyacetylene cations do not fluorescence. The lifetimes of the first excited state for $C_4H_2^+$, $C_6H_2^+$ and $C_8H_2^+$ have been measured to be 71, 17 and < 6 ns, respectively [101-102]. As the observed FWHM for all origin bands are greater than 2.2 cm^{-1} , the lifetime of the excited states is expected to lie in the 100 picosecond range. The decay curves of the excited states exhibit different behaviour. The observed decay constants for the $A^2\Pi_g$ and $B^2\Pi_g$ states are ~ 64 and $9 \mu\text{s}$. Estimate of the collisional rate based on Langevin theory in the presence of $\sim 10^{-3}$ mbar buffer gas leads to ~ 10 collision/ μs . Thus, the long decay curves are likely related to the deactivation process by the collisions of trapped ions with buffer gas. The same deactivation process for the first excited state of $C_{10}H_2^+$ was studied previously [35]. However, the maximum shift was not observed [103]. The energy of the second probe photon was the only difference in the experiments (in the present work 4.5 eV as compared to 5 eV). It is assumed that this 0.5 eV additional energy distributed among the 31 vibrational oscillators of $C_{10}H_2^+$ cation leads to different photofragmentation rate and is likely responsible for the observed 26.3 μs shift.

The first colour excites the cation after which fast intra relaxation process can either leave the molecule in a highly excited vibrational level of the ground state or in a close lying

quartet state [35]. These ${}^4\Pi_u$, ${}^4\Pi_g$ quartet states were theoretically investigated for the $C_4H_2^+$ and $C_6H_2^+$ cations. It was shown that the quartet states lie above $A^2\Pi$ state [96]. However, the quartet states drop closer to the double states as the ion is bent. Therefore, they may play role in the observed decay curves.

6.2.10 Conclusion

The summary of the results are presented in *Table 6.2.10.I*.

	λ , nm ^a	λ , nm ^b	$\tilde{\nu}$, cm ⁻¹ ^b	FWHM, cm ⁻¹ ^b	Transition
$C_8H_2^+$	568.5	566.22 ± 0.02	17661 ± 0.5	4 ± 0.5	$B^2\Pi_u - X^2\Pi_g$
	495.2	494.56 ± 0.03	20220 ± 1	8 ± 1	$C^2\Pi_u - X^2\Pi_g$
$C_{10}H_2^+$		815.4*	12264*	2.2 ± 0.2	$A^2\Pi_g - X^2\Pi_u$
	649.2	646.66 ± 0.02	15464 ± 0.5	4 ± 0.5	$B^2\Pi_g - X^2\Pi_u$
	567.3	566.1 ± 0.1	17664 ± 2.5	30 ± 2.5	$C^2\Pi_g - X^2\Pi_u$
$C_{12}H_2^+$	538.5	536.1 ± 0.1	18646 ± 2.5	28 ± 2.5	$D^2\Pi_u - X^2\Pi_g$

Table 6.2.10.I. Observed wavelengths of the five new origin bands.

^a Studies in neon matrices at 6 K. ^b This work. * Previous study in an ion trap [35].

Five origin bands of higher excited states of polyacetylene cations have been observed by two-colour, two-photon resonance-enhanced photodissociation spectroscopy for the first time in the gas-phase. The observed ions have a rotational temperature in the range between 15-25 K which allows a direct comparison between experiment and astrophysical data. Although no

matches were found between the experimentally determined origin bands and any known diffuse interstellar bands [10, 104-105], some conclusions can be made.

The first is that the FWHMs of the origin bands of higher excited states increase with increasing electronic excitation. This was illustrated with the $A^2\Pi_g$, $B^2\Pi_g$ and $C^2\Pi_g$ excited states of $C_{10}H_2^+$ cation. For $C_8H_2^+$ only two $B^2\Pi_u$ and $C^2\Pi_u$ excited states were measured and compared. The same behaviour was observed: the FWHM of the origin band of $C^2\Pi_u$ excited state is greater than the FWHM of the origin band of $B^2\Pi_u$ state (4 as compared to 8 cm^{-1}). Another conclusion is derived when the FWHMs of the origin bands of the same electronic state are considered for different cations ($HC_{2n}H^+$ $n=4,5,\dots$). In case of $C_8H_2^+$ and $C_{10}H_2^+$ the FWHMs of the origin band of the $B^2\Pi_{g/u}$ excited state are $\sim 4 cm^{-1}$, whereas for the $C^2\Pi_u$ excited state of $C_{10}H_2^+$ the FWHM is greater than in $C_8H_2^+$, 30 and 8 cm^{-1} . Thus, the bandwidth of the transition of the $C^2\Pi_{u/g}$ state increases with increasing number of carbon atoms in the molecule. In contrast, the observed bandwidths for $B^2\Pi_{g/u}$ state are the same and do not change or change slightly with increasing number of carbon atoms.

The study of the FWHMs of the bands is important for molecules of astrophysical relevance. A pseudo energy diagram showing location of interstellar absorption bands versus their FWHM in the DIB range 400-900 nm is presented in *Figure 6.2.10.1 [106]*. Roughly, the FWHM distribution can be divided into three classes: very broad (15-200 cm^{-1}), broad (3-15 cm^{-1}) and narrow DIBs (1-3 cm^{-1}). Most DIBs are concentrated between 1.56 and 2.25 eV (550-795 nm); very narrow DIBs above 2.25 eV; and few very broad DIBs above 3.0 eV. For the spectral range in the present work DIBs have FWHMs of 1-5 cm^{-1} . Accordingly, only the origin bands of the $B^2\Pi_{g/u} - X^2\Pi_{u/g}$ transition of $C_8H_2^+$ and $C_{10}H_2^+$ cations fall in a class relevant for DIBs. The origin bands of the $C^2\Pi_{g/u} - X^2\Pi_{u/g}$ and the $D^2\Pi_u - X^2\Pi_g$ transitions are too broad. Although no direct matches were found between the experimentally determined origin bands and any known diffuse interstellar bands, based on experimental FWHMs of $B^2\Pi_{g/u}$ states we assume that these of $C_{12}H_2^+$ and $C_{14}H_2^+$ cations are of DIB relevance.

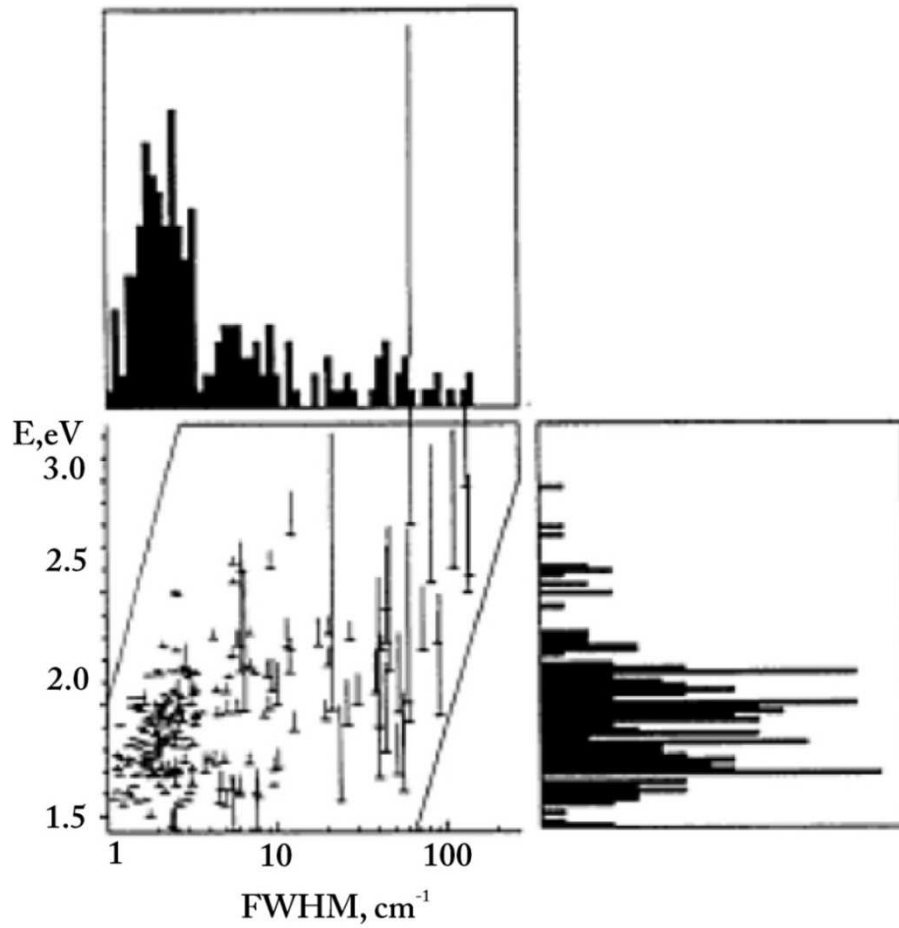


Figure 6.2.10.I. Histograms of energy and FWHM distribution of DIBs. The FWHM distribution has two or perhaps three peaks, while the energy distribution has a broad maximum between 1.56 and 2.25 eV. (Histogram is taken from Ref. [106])

6.3 C₄H₃Cl⁺ cation

The original aim was to record the electronic spectrum of C₇H₂⁺ in the gas phase, which was previously measured in a 6 K neon matrix [21]. The origin band of the A²Π_g – X²Π_u transition of C₇H₂⁺ is located around 599.5 nm. In order to produce the odd carbon cation chains, diacetylene precursor was used. The mass 86 m/z corresponding to C₇H₂⁺ was selected with a first quadrupole mass filter following the standard procedure described in *Chapter 5* (*Figure 6.3.I*).

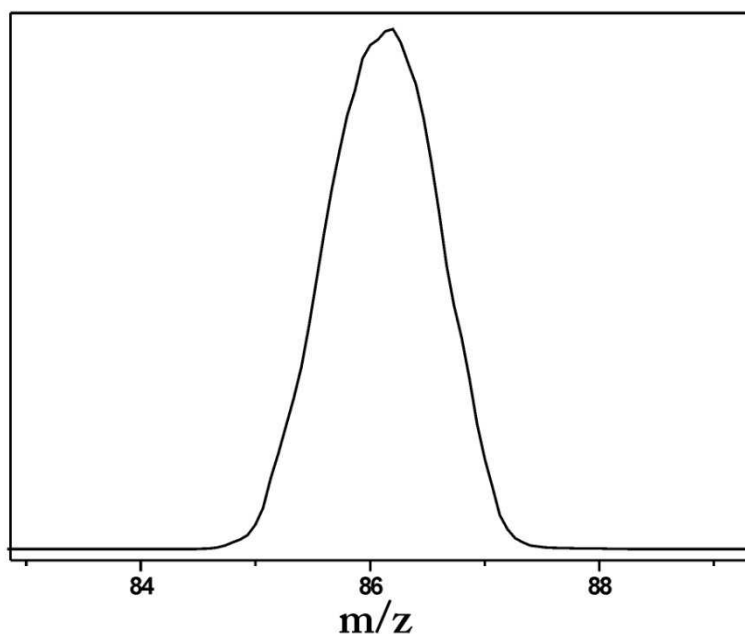


Figure 6.3.I. Mass spectrum of diacetylene with a mass peak centered around 86 m/z.

Both quadrupoles were calibrated using Kr⁺ (electron ionization) and compared with the mass spectrum from NIST Mass Spectrum Data Center [107]. *Figure 6.3.II(a)* presents the spectrum of Kr⁺ taken from the database and *Figure 6.3.II(b)* was the one obtained during calibration. The positions and intensities of the mass peaks are matched. R2C2PD spectroscopy was applied to record the origin band. The photofragmentation loss channel of C₃H (37 ± 2 u) was monitored. However, no transition was observed around 599.5 nm but an unexpected transition with the origin band located near 521 nm was obtained (*Figure 6.3.III*). As neon matrix shifts are normally less than 1% of the transition energy [99] which in case of a band around 599.5 nm is about 166 cm⁻¹. Therefore, it was concluded that the obtained spectrum was not the spectrum of linear C₇H₂⁺.

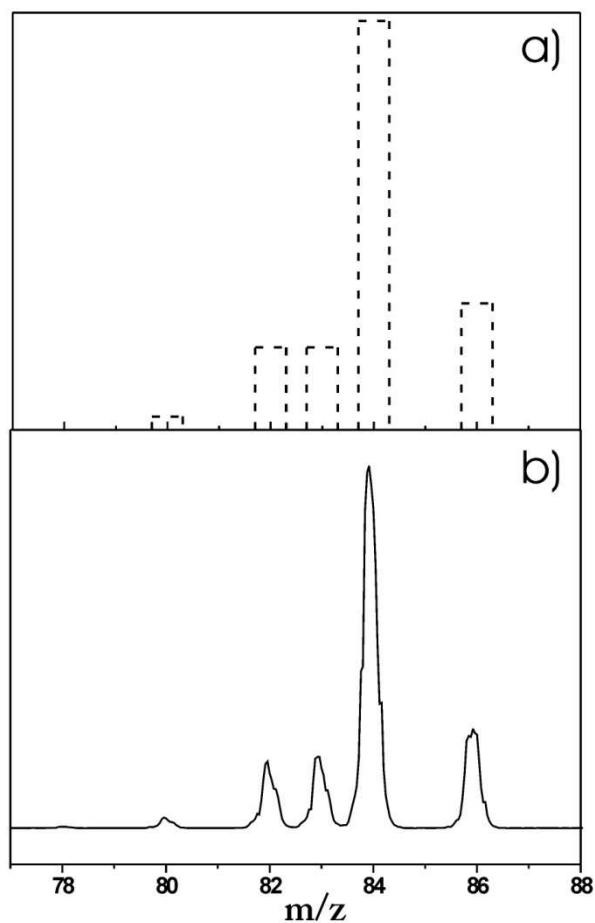


Figure 6.3.II. Mass calibration a) spectrum of Kr^+ from NIST database (Ref.[107]) and b) experimental mass spectrum obtained in an ion trap.

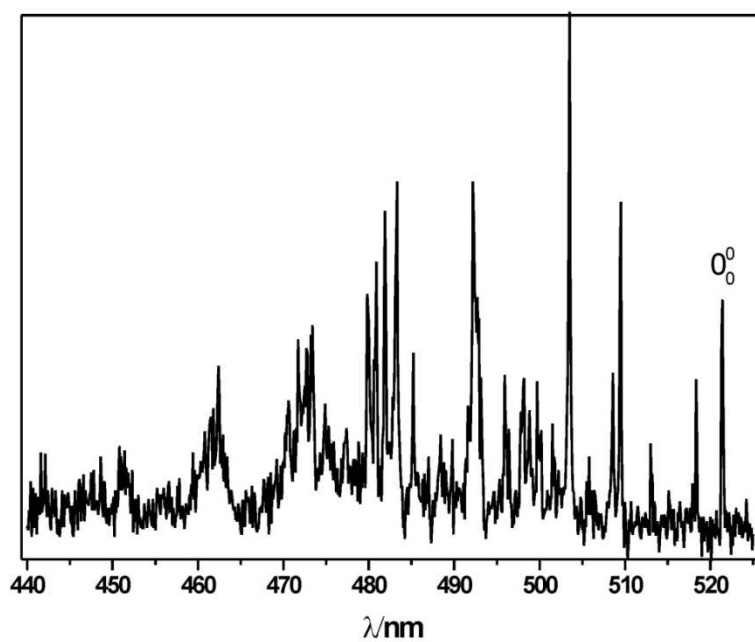


Figure 6.3.III Observed electronic spectrum with the origin band located near 521 nm.

The electronic spectrum recorded in the experiment shows rich vibrational structure. After the peak around 521 nm no transitions were observed to the red up to 600 nm. Therefore, the peak was assigned to the origin band and the spectrum could be obtained by using one visible colour with the power of 0.5 mJ. The dye laser with 0.05 cm^{-1} resolution was used to rotationally resolve the 0_0^0 band (*Figure 6.3.IV*).

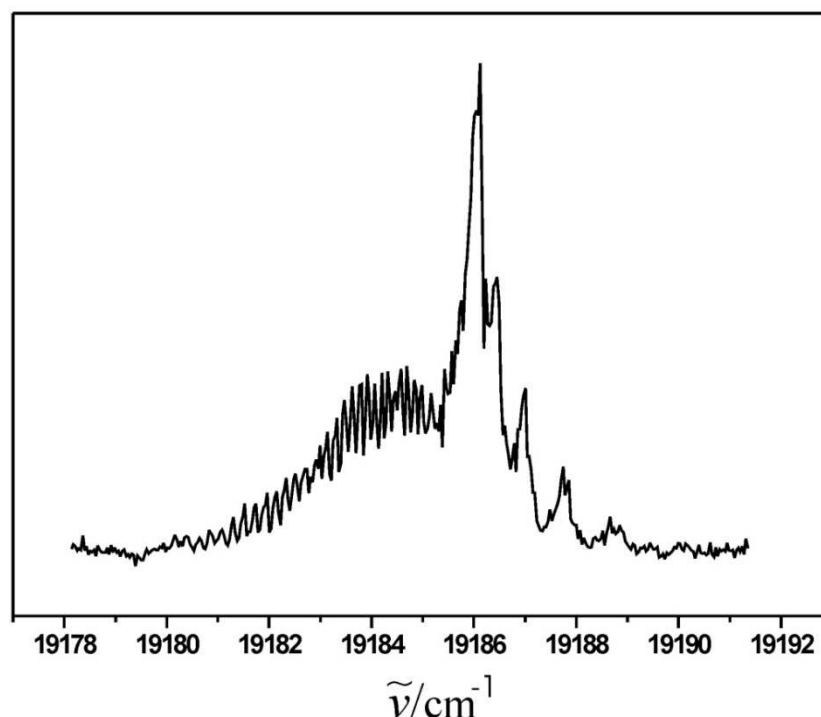


Figure 6.3.IV. Rotationally resolved origin band located at 19186 cm^{-1} .

6.3.1 Rotational analysis

The origin band has a well-resolved K-structure which is not a feature for a linear molecule as expected for the linear C_7H_2^+ cation. It was assumed that diacetylene was contaminated in the chemical preparation because a chlorinated precursor was used. Accordingly, the presence of $\text{C}_4\text{H}_3\text{Cl}^+$ at the same mass of 86 m/z in an ion trap was suggested. In order to explain the experimentally obtained data, DFT calculations were made (basis set for open-shell molecules was b3lyp/(6-311++G(d,p))) for the ground state. The results of different isomers of $\text{C}_4\text{H}_3\text{Cl}^+$ with *A, B, C* rotational constants are presented in *Table 6.3.I.I*. Altogether, five isomers were obtained. From the calculations it follows that the isomer A has the lowest energy.

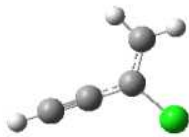

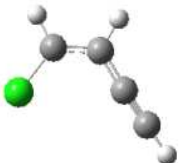


Isomer	Energy / eV	A / GHz	B/ GHz	C/ GHz
 D	0.345	7.106	3.047	2.132
 C	0.186	43.245	1.399	1.355
 B	0.045	9.472	2.486	1.969
 Lin	0.043	26.621	1.547	1.464
 A	0	45.747	1.545	1.499

Table 6.3.1.I. Relative energies and rotational constants of $C_4H_3Cl^+$ C_s symmetry isomers of the ground state.

Although it is supposed that in an ion trap at low temperatures of about 20 K, isomer A has to be observed as it is the lowest energy; additional information can be obtained from the resolved structure of the origin band. Starting with the rotational constants presented in *Table 6.3.1.I*, it was possible to simulate the band profiles of the different isomers using *PGopher* [84]. The three principal moments of inertia of the isomers differ; the isomers were

classified as asymmetric tops. In the simulations the model of the rigid rotor was used and centrifugal distortion was not taken into account.

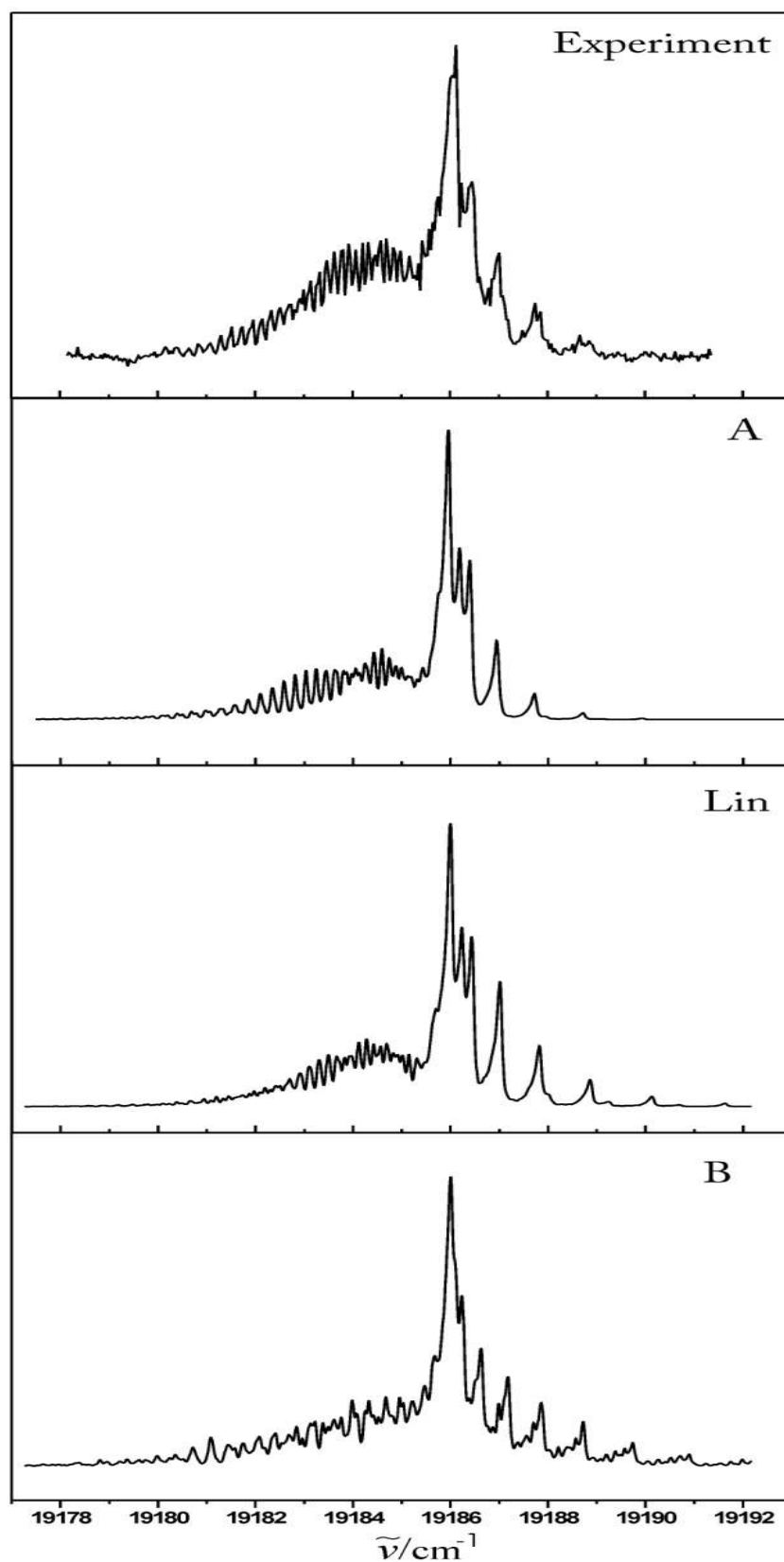


Figure 6.3.1.I. Rotationally resolved origin band and simulations of different isomers at 20 K (*a*-type rotational transition). ${}^2A' \rightarrow {}^2A'$ and ${}^2A'' \rightarrow {}^2A''$ electronic excitations.

With *PGopher* it was possible to set the symmetry of the molecule (C_s), rotational constant of ground and excited state and type of transition (a,b,c). In the fit only the rotational constants of the excited state were varied. The fitting procedure included about 800 rotational lines was considered converged when residual errors were ~ 0.1 for all isomers. Relative intensity of the lines and separations/positions of the bandheads were controlled and the temperature of simulations was set to 20 K as a typical rotational temperature of ions.

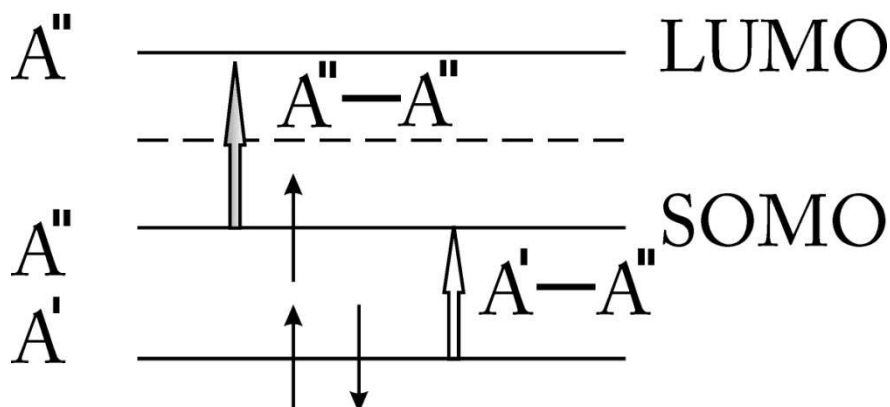


Figure 6.3.1.II. MO diagram with ${}^2A'-{}^2A''$ and ${}^2A''-{}^2A''$ electronic excitations.

Results are presented in *Figure 6.3.1.I*. Firstly, it was not possible to fit the 0_0^0 band with the constants of isomer B, C and D; only the simulation for isomer B is depicted (*Figure 6.3.1.I*). As a result the band of isomer B has different relative intensities and the bandhead separations. At the same time, for isomer A and the linear isomer, the fitted spectra exhibit a much better agreement with the experimental spectrum. The simulations were performed for an a-type ${}^2A'-{}^2A'$ and ${}^2A''-{}^2A''$ electronic transitions. With other types of rotational transitions and electronic excitations the fit procedure did not converge. The MO diagram based on DFT calculations for the ground state is depicted in *Figure 6.3.1.II*. As singly occupied molecular orbital (SOMO) has A'' symmetry, hence the ground electronic state is ${}^2A''$ and therefore, it has been assumed that the possible observed electronic transition in the experiment is ${}^2A''-{}^2A''$.

The obtained rotational constants of the excited state for the linear and isomer A are presented in *Table 6.3.1.II*.



	A/GHz	B/GHz	C/GHz		
	A	45.75	1.54	1.50	ground state (DFT values)
		48.95	1.46	1.44	excited state (fitted)
		1.07	0.95	0.96	excited/ground
	Lin	26.62	1.55	1.46	ground state (DFT values)
		29.98	1.42	1.40	excited state (fitted)
		1.12	0.92	0.96	excited/ground

Table 6.3.1.II. Obtained rotational constants of isomers.

From *Table 6.3.1.II*, it follows that the isomer A has the closest rotational constants in the excited state to the rotational constants in the ground state. For example, the ratio of A constants for the isomer A in excited state to the ground state is 1.07. At the same time for the linear isomer this ratio is 1.12. Thus, it has been assumed that isomer A and the linear isomer are likely responsible for the observed origin band in the experiment and the 0_0^0 band was assigned to an a-type ${}^2A''-{}^2A''$ electronic transition of the $C_4H_3Cl^+$ cation.

6.4 Anthracene and naphthalene radical cations

Naphthalene (Np^+) and anthracene (An^+) radical cations were chosen as representatives of the polycyclic aromatic hydrocarbons (PAH), having potential for astrophysical interest (*Chapter 1*). Accordingly, R2C2PD spectroscopy, which was applied to linear carbon chains, was chosen to probe the electronic transitions of PAH^+ cations.

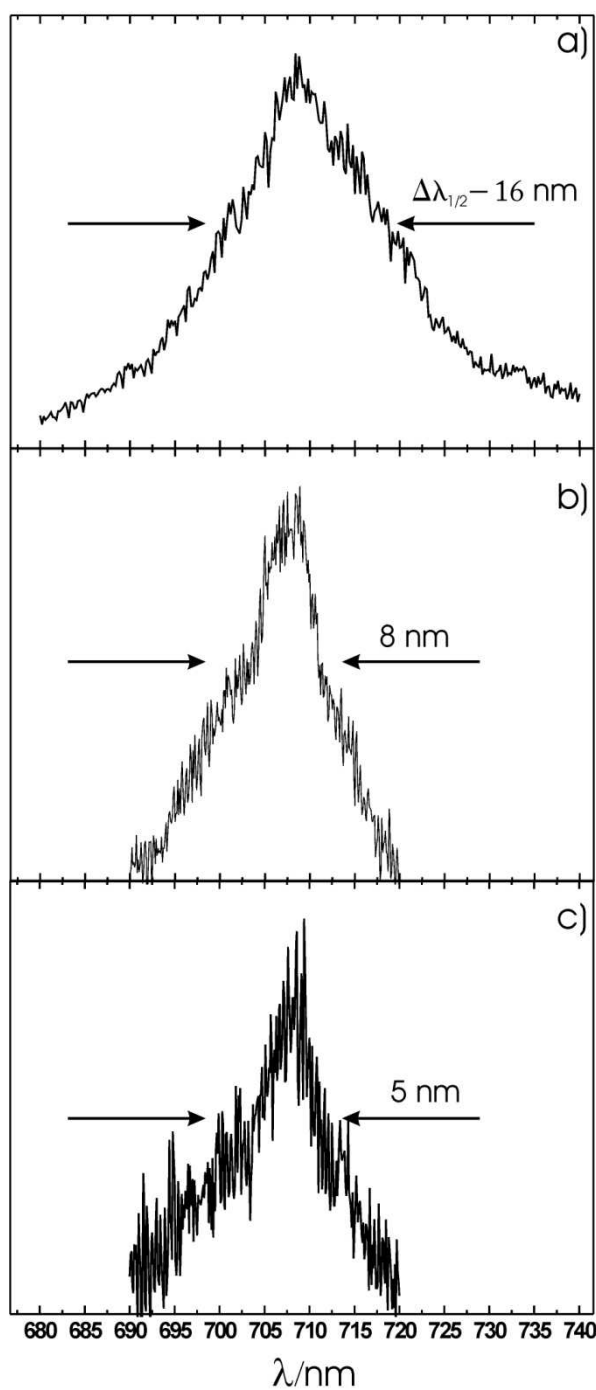


Figure 6.4.1. The $D_2(^2A_u) \leftarrow D_0(^2B_{2g})$ transition of An^+ at 708 nm. The power of the scanning laser was a) 2.4 b) 1.1 and c) less than 0.2 mJ.

The $D_2(^2A_u) \leftarrow D_0(^2B_{2g})$ transition of An^+ was observed at 708.5 ± 0.5 nm (*Figure 6.4.I*). The second colour was 5.4 eV (230 nm) with a power of 0.5 mJ per pulse and the FWHM of the transition has a strong, non-linear power dependence upon the first colour. The FWHM for different laser power was ~ 16 nm at 2.4 mJ, ~ 8 nm at 1.1 mJ and ~ 5 nm when it was less than 0.2 mJ. An^+ cations were thermalized with cryogenically cooled buffer gas, therefore ions have a temperature ~ 20 K.

R2C2PD spectroscopy was not possible to realize for Np^+ . Although, the second colour was varied in a wide range of energies 5.9-4.1 eV (210-300 nm) and the two laser pulses were overlapped in time and spatially. However, using multi-photon, one-colour photofragmentation spectroscopy was possible to obtain the $D_2(^2B_{3g}) \leftarrow D_0(X^2A_u)$ transition of Np^+ at 672 ± 1.5 nm when 5 mJ of laser power was used (*Figure 6.4.II*). Already with a power of 3.5 mJ the S/N ratio was below the detection limit. The measured FWHM of the transition was broad and ~ 6.5 nm. The measurement of Np^+ was performed at room temperature, and in both experiments the photofragmentation loss channel of C_2H_2 was monitored.

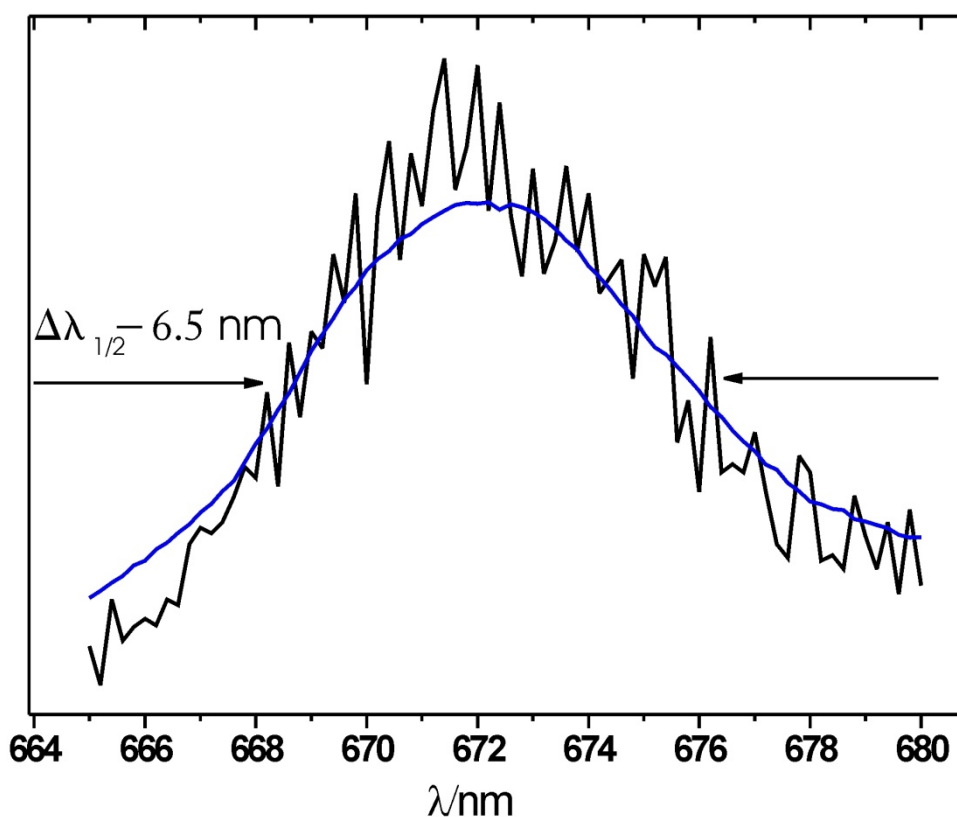


Figure 6.4.II. The $D_2(^2B_{3g}) \leftarrow D_0(X^2A_u)$ transition of Np^+ at 672 nm.

<i>Species</i>	<i>Conditions</i>	λ/nm	<i>FWHM/nm</i>
Np^+	<i>Gas phase</i> ^a	670.73 ± 0.06	1.63
Np^+	<i>22 ion trap</i> ^c	672 ± 1.5	6.5 ± 1.5
An^+	<i>Gas phase</i> ^a	708.76 ± 0.13	4.75
An^+	<i>22 ion trap</i> ^c	708.5 ± 0.5	5 ± 0.5
An^+	<i>REMD in an RF ion trap</i> ^b	~ 712	70

Table 6.4.I Absorption band maxima for Np^+ and An^+ cation observed in supersonic jets [108]^a, REMD [32]^b and 22 pole ion trap^c.

Table 6.4.I presents a summary of the results obtained in this work for Np^+ and An^+ cation compared to results observed by CRDS [108] and by resonance enhanced multiphoton dissociation (REMD) technique [32]. The latter technique is related to the multiphoton dissociation of An^+ by intense laser radiation.

Rotational and vibrational temperatures in the CRDS experiments are believed to be larger than 50 K [108]. This assumption was argued because a larger FWHM than expected was observed for the transition of An^+ . However, based on the previous results obtained in an ion trap, it was assumed that the An^+ cation was thermalized to 20 K [34, 49]. Thus, the experimentally observed band with FWHM ~ 5 nm can be directly compared with diffuse interstellar bands. The FWHM of a close-lying DIB at 708.7 nm is only 0.2 nm, whereas the present work has a band at 708.5 ± 0.5 nm. Although at the proper position, it is 5 nm broad and almost a factor of 25 wider [104]; therefore, the An^+ cation is not of DIB relevance.

There are many reasons why only a few PAHs have been measured in a 22-pole ion trap by means of two-colour and/or one-colour multi-photon techniques (i.e An^+ and Np^+ cations) and they can be understood. The resilience of PAHs toward decomposition is due to their high bond energies and many degrees of freedom. Photodissociation experiments on pure PAH cations have shown that decomposition process goes through intramolecular vibrational redistribution (IVR). The absorbed energy is subsequently distributed among all vibrational degrees of freedom of a molecule, where the phase space of microscopic states is defined with equal energy. A molecule explores these states randomly through IVR. If the energy stored in one particular degree of freedom is higher than the dissociation energy of this bond (e.g., about 3.8 eV for a CH bond in a PAH cation), then it undergoes photodissociation by cleavage of a specific bond. Characteristic

rates of infrared emission from excited vibrational levels of aromatic neutral or ionic species have been determined experimentally to be in the range $1-10^3 \text{ s}^{-1}$. A critical energy is entered as a parameter where the dissociation rates are less than or equal to 10^2 s^{-1} , i.e. below which infrared radioactive relaxation will dominate over fragmentation [109]. The dissociation rate depends strongly on internal energy stored in vibrational modes [110]. For example, to dissociate coronene cation with a dissociation rate of 10^2 s^{-1} , more than 10 eV of energy is needed. Another feature of PAH photofragmentation is the different loss channels. Experimentally, C_2H_2 loss has only been observed for small catacondensed PAHs with an open skeleton (e.g. naphthalene, anthracene and phenanthrene), whereas for the pericondensed PAHs (e.g. coronene, pyrene and coronene) the dominant loss channel is atomic hydrogen [111-112]. Attempts to obtain the electronic spectrum of the coronene cation were unsuccessful in a 22-pole ion trap, although the H channel loss was monitored. The two-colour, two-photon technique is limited by the laser radiation of an OPO. Namely, the sum energy of two photons leads a total energy of $\sim 8 \text{ eV}$. This energy is enough to dissociate benzene, naphthalene, anthracene radical cations but already with pyrene cation this becomes more difficult. In order to initiate fragmentation, at least two UV photons have to be absorbed in addition to the first one within the visible region. Another difficulty derives from intrinsic transition bandwidth for the electronic transitions of several 10s cm^{-1} [108, 113]. This fact leads to the conclusion that fast non-radioactive processes (of the order of $\sim 50 \text{ fs}$) occur in the excited PAH cations. Thus, with nanosecond lasers is not possible to probe the excited states. Some other states have to be used to drive the molecule above photofragmentation threshold but these states are not known because of lack of experimental and theoretical investigations.

From the spectra obtained using the REMD technique, it has been observed that there is a disadvantage of resonance multi-photon photofragmentation spectroscopy. The efficiency of this technique is strongly dependent on the laser power and several photons are needed to produce photodissociation channels. The photofragmentation rate for the naphthalene cation is calculated to be 10^3 s^{-1} at 7 eV internal energy and 10^5 s^{-1} at 8 eV for the C_2H_2 loss channel, whereas the critical energy to dissociate the cation is ca. 6.3 eV [110]. In the case of the Np^+ cation, this leads to the absorption of more than 4 photons. The absorption of many-photons and high power leads to saturation of the recorded band. As a result the FWHM is very broad, and for An^+ cation, it has been measured by REMD to be approximately 70 nm at room temperature [32]. In a 22-pole ion trap, REMD spectroscopy for the Np^+ gives a FWHM of about 6.5 nm at room temperature, whereas CRDS gives 1.5 nm [108]. Thus, the resonance multi-photon photodissociation

spectroscopy does not give a natural bandwidth of the transition and the obtained FWHM cannot be comparable with astrophysical observations.

6.5 $\text{B}^2\Sigma_u^+ \leftarrow \text{X}^2\Pi_g$ *electronic spectrum of NCCN⁺ in the gas phase*

$B^2\Sigma_u^+ \leftarrow X^2\Pi_g$ electronic spectrum of NCCN^+ in the gas phaseV. Rudnev, C. A. Rice, and J. P. Maier^{a)}*Department of Chemistry, University of Basel, Klingelbergstrasse 80, CH-4056 Basel, Switzerland*

(Received 7 July 2008; accepted 3 September 2008; published online 7 October 2008)

The $B^2\Sigma_u^+ \leftarrow X^2\Pi_g$ absorption spectrum of NCCN^+ in the gas-phase was observed using a two-color, two-photon photodissociation technique. This was measured at ~ 20 K in a 22-pole ion trap with laser bandwidths of less than a cm^{-1} . The spectrum shows distinct vibrational structure, with the origin band near $11\,253\text{ cm}^{-1}$, and the excitation of four normal modes in the excited state. The rotational structure of the 0_0^0 band in the gas phase could not be resolved, indicating that the $B^2\Sigma_u^+$ state has a lifetime of a few picoseconds because of a fast intramolecular process. © 2008 American Institute of Physics. [DOI: 10.1063/1.2989982]

I. INTRODUCTION

Cyanopolyacetylene chains have been identified in the interstellar medium using radio astronomy up to HC_{11}N .¹ The centrosymmetric $\text{NC}(\text{CC})_n\text{CN}$ chains and their cations are not accessible to millimeter-wave spectroscopy because they lack a permanent dipole moment. However, their electronic spectra can be observed, making them of astrophysical interest. Ions and large neutral molecules can have electronic transitions in the 400–900 nm region.² $\text{NC}(\text{CC})_n\text{CN}^+$ ($n=1,2$) are two such moieties with a band system in the visible region.^{3,4} The origin band of the $^2\Pi \leftarrow X^2\Pi$ transition of dicyanoacetylene cation is close to a diffuse interstellar band with a similar two peak contour but the position differs by about 3 cm^{-1} .⁵

Cyanogen (NCCN) and its cation are two components which make up the atmosphere of Titan,^{6,7} whereby the sun's UV radiation produces NCCN^+ . The latter has a $X^2\Pi_{3/2,g}$ ground state. Four excited states $A^2\Sigma_g^+$, $B^2\Sigma_u^+$, $C^2\Pi_u$, and $D^2\Pi_u$ have long been known from photoelectron (PE) spectroscopy^{8,9} and theory.^{10–12} The transitions from the $X^2\Pi_g$ ground state to the B , C , and D states are dipole allowed. The cation has also been investigated by matrix isolation spectroscopy, where its electronic^{12,13} and infrared¹⁴ spectra have been recorded. In the neon matrix at 6 K, the observation of the $B^2\Sigma_u^+ \leftarrow X^2\Pi_g$ transition is hindered by the absorption bands of CN ($A^2\Pi_i \leftarrow X^2\Sigma^+$) and C_2 ($A^1\Pi_u \leftarrow X^1\Sigma_g^+$), causing spectral congestion and leading to an uncertainty in the location of the origin band.¹² The photoelectron⁸ and photoionization¹⁵ spectra are also broad.

The best resolved spectra observed so far are by a PFI-PE measurement⁹ using a molecular beam and synchrotron radiation, though the resolution is still limited to $\sim 12\text{ cm}^{-1}$. In the present work, a new approach to study mass-selected ions at low temperature is used to obtain a good quality absorption spectrum with a resolution of approximately 0.3 cm^{-1} . The width of the bands in the observed $B^2\Sigma_u^+ \leftarrow X^2\Pi_g$ electronic absorption spectrum is limited by lifetime broadening of the excited state. The method

used a 22-pole trap to confine and collisionally cool the cyanogen cations to 20–30 K prior to the measurement of the absorption using a two-color excitation dissociation approach.

II. METHOD

The cyanogen cations were created using electron impact (20 eV) of the neutral molecular gas. The apparatus employed earlier¹⁶ was modified by incorporating a magnetic bender which separates cations and neutrals after they exit the source from a 0.5 mm pinhole (Fig. 1). The ions were passed into a hexapole, subsequently mass-selected by a quadrupole filter and then injected into a 36 mm long 22-pole ion trap, based on the design of Gerlich.¹⁷ The mass resolution was set to $\pm 0.5\text{ u}$. The trap was filled with approximately 70 000 ions in 20 ms. There, the ions undergo collisions with cryogenically cooled He gas (approximately 10 K) for 70 ms, thermalizing their rotational and vibrational degrees of freedom.

The ions were probed using a two-color, two-photon pump-probe technique. In this the ions were first excited by one photon from a tunable OPO laser (0.3 cm^{-1}) and subsequently fragmented by a second photon at 355 nm (6 cm^{-1}). The two laser beams were overlapped in time and space for the optimization of the signal. After resonance excitation the dissociation products were released from the ion trap by lowering the exit potential. A second quadrupole mass filter analyses and detects fragment ions. The spectra were obtained by monitoring CN^+ as a function of photon energy. Measurements of the 0_0^0 band in the $B^2\Sigma_u^+ \leftarrow X^2\Pi_{3/2,g}$ transition with a Nd:YAG pumped dye laser with a 0.15 cm^{-1} bandwidth were also carried out.

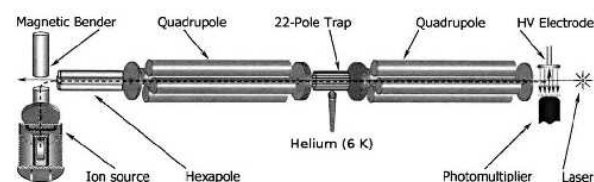


FIG. 1. Experimental scheme of the ion trap apparatus.

^{a)} Author to whom correspondence should be addressed. Electronic mail: j.p.maier@unibas.ch.

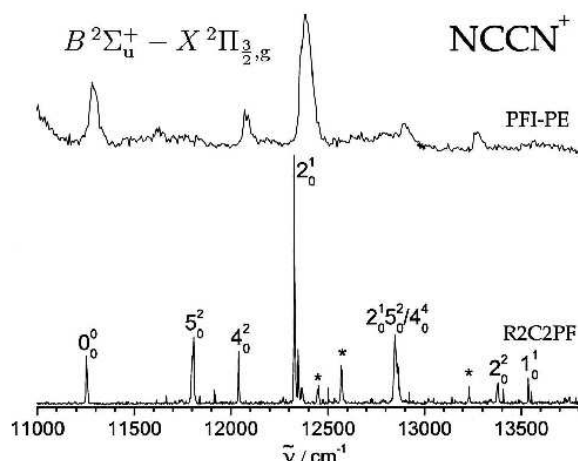


FIG. 2. Comparison of resonance two-photon, two-color spectrum of the $B^2\Sigma_u^+ - X^2\Pi_{3/2,g}$ transition in a 22-pole ion trap (~ 20 K) and pulsed-field ionization-photoelectron (Ref. 9) (300 K) spectrum (made available by the authors of Ref. 9). The photodissociation product CN^+ was monitored to obtain the lower spectrum.

III. RESULTS AND DISCUSSION

The spectrum was recorded using a resonant two-color, two-photon fragmentation (R2C2PF) technique in the 11 000–13 800 cm^{-1} range where the $B^2\Sigma_u^+ \leftarrow X^2\Pi_g$ electronic transition is expected, based on the PFI-PE⁹ and matrix isolation¹² studies. A distinct spectrum is observed (Fig. 2) with good signal-to-noise ratio (20:1). The observed origin band is centered at 11 253 cm^{-1} . This value is 32 cm^{-1} lower than that reported in the PFI-PE study, quoted with an uncertainty of ± 8 cm^{-1} .⁹

In addition to the origin band, the spectrum in Fig. 2 shows vibrational excitation in the upper electronic state. The ground electronic state $X^2\Pi_g$ is inverted with a calculated spin-orbit constant of around -55 cm^{-1} .⁹ Thus, all the transitions originate from $v=0$ of the lower level $X^2\Pi_{3/2,g}$ as the $\Pi_{1/2,g}$ component is not significantly populated at ~ 20 K. The vibrational assignment of the $B^2\Sigma_u^+ \leftarrow X^2\Pi_{3/2,g}$ transition is shown in Fig. 2 and the positions of the band maxima are given in Table I.

The excitation of the two stretching modes ν_1 and ν_2 in the $B^2\Sigma_u^+$ state is seen and the 2_0^1 transition is the most intense band in the spectrum. The intensities may be somewhat distorted because this is not a linear absorption experiment. Thus, the two small, unidentified bands to the blue of 2_0^1 vibrational band become apparent because of saturation. The 2_0^2 band is also observed at 13 380 cm^{-1} . The Franck-Condon intensity distribution shows that the bond lengths in the $B^2\Sigma_u^+$ and $X^2\Pi_g$ states are different. The theoretical calculations¹² indicate that the C–C length remains almost the same, whereas the CN bond decreases by 0.037 Å. Compared to the ground state, the ν_2 frequency of 1066 cm^{-1} increases from 956 cm^{-1} in the $X^2\Pi_g$ state.⁹ The increase appears to result from the CN bond length decreasing. The assigned 1_0^1 transition leads to $\nu_1' = 2287$ cm^{-1} , whereas in the $X^2\Pi_g$ state it is 2263 cm^{-1} according to the PFI-PE data.⁹ The excitation of the ν_4 and ν_5 degenerate modes in double quanta is seen at 11 799 and 12 032 cm^{-1} , respectively. The

TABLE I. Vibrational band maxima (± 1 cm^{-1}) observed in the $B^2\Sigma_u^+ - X^2\Pi_{3/2,g}$ transition of NCCN^+ and a comparison with the PFI-PE data. An asterisk (*) denotes unassigned bands. The last column shows a reassignment of the absorption spectrum observed in a neon matrix. The error limits given in Refs. 9 and 12 are ± 8 and ± 3 cm^{-1} , respectively.

Assignment	This work		$\bar{\nu}$ (cm^{-1})	
	$\bar{\nu}$ (cm^{-1})	$\Delta\bar{\nu}$ (cm^{-1})	PFI-PE ^a	Matrix ^b
0_0^0	11 253		11 285	
5_0^2	11 799	546	11 618	11 748 11 770 11 826
4_0^2	12 032	779	12 074	11 982 12 000 12 051
2_0^1	12 319	1066	12 384	12 248 12 270 12 319
*	12 444	1191		
*	12 562	1309		12 502 12 532 12 586
$2_0^1 5_0^2 / 4_0^4$	12 837	1584		
*	13 230	1977		
2_0^2	13 380	2127		
1_0^1	13 540	2287		

^aReference 9.

^bReference 12.

inferred vibrational frequencies in the $B^2\Sigma_u^+$ state are collected in Table II where they are compared to the $X^2\Pi_g$ state values from the PFI-PE study. The theoretically calculated¹² frequencies and symmetries of the three stretching and two bending modes in the ground state of the cation are included in the caption of Table II.

A comparison of the R2C2PF spectrum (~ 20 K) of Fig. 2 with that measured by the PFI-PE technique (~ 300 K) is made in Fig. 2. Apart from the widths of the peaks due to the different temperatures, there are irregular shifts in the frequencies between the two sets of data (Table I). The 0_0^0 , 2_0^1 , and 4_0^2 transitions differ by 32, 65, and 42 cm^{-1} , respectively. The discrepancies are outside the ± 8 cm^{-1} error quoted in the PFI-PE study.⁹ The temperature difference (20 K versus 300 K) between the two measurements would result in a

TABLE II. Experimentally determined vibrational frequencies (in cm^{-1}). The calculated (Ref. 12) $X^2\Pi_g$ state frequencies are $\nu_1(\sigma_g^+) = 2300$, $\nu_2(\sigma_g^+) = 808$, $\nu_3(\sigma_u^+) = 1789$, $\nu_4(\pi_g) = 537$, and $\nu_5(\pi_u) = 240$.

	$X^1\Sigma_g^+$ NCCN^a	NCCN^+	
		$X^2\Pi_g$	$B^2\Sigma_u^+$
ν_1	2330(3)	2262(10) ^b	2287(1) ^c
ν_2	846(6)	956(10) ^b	1066(1) ^c
ν_3	2158(1)	1818(20) ^b	
ν_4	503(6)		390 ^d
ν_5	234(3)		273 ^d

^aReference 19.

^bReference 9.

^cThis work.

^dObtained by dividing double quanta excitations.

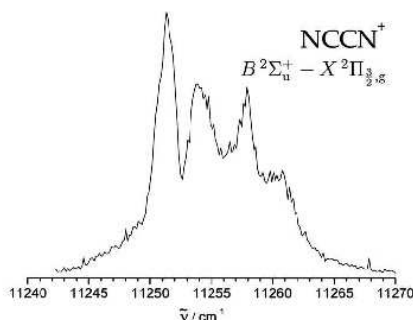


FIG. 3. The origin band of the $B^2\Sigma_u^+ \leftarrow X^2\Pi_{3/2,g}$ transition of NCCN^+ recorded with 0.15 cm^{-1} laser bandwidth. The first two peaks to the left are the unresolved P and R branches, whereas the two bands above $11\,256 \text{ cm}^{-1}$ are assumed to originate from a transition to the $A^2\Sigma_g^+$ manifold.

shift of the band's maximum of a few wavenumbers at most, according to simulation of the rotational profile. The current data, due to better resolution and calibration, are judged to be the more reliable. Some bands in the PFI-PE spectrum have a weak intensity compared to the spectrum in Fig. 2 (e.g., S_0^2 transition), probably due to the difference in the Franck-Condon overlap in the two approaches. In the PFI-PE measurement the electronic excitation originates from the $X^1\Sigma_g^+$ ground state of the neutral using a single photon, while in R2C2PF from the $X^2\Pi_g$ state of the cation to the excited state which is then followed by another photon absorption and dissociation.

In Table I the absorption band maxima of the $B^2\Sigma_u^+ \leftarrow X^2\Pi_g$ transition measured in a 6 K matrix¹² are given. In the latter study, the origin band was assumed to be at $11\,486(3) \text{ cm}^{-1}$. The present data show that in the matrix the origin band was not observed and it lies under the intense CN absorption ($A^2\Pi \leftarrow X^2\Sigma^+$, $v''=1$), causing a misassignment of the vibrational progression within the spectrum. This leads to a reassignment of the observed bands and this is given in the last column of Table I. The unassigned band in the neon matrix at $11\,769 \text{ cm}^{-1}$ corresponds to the S_0^2 vibrational band in Fig. 2, whereas that at $12\,000 \text{ cm}^{-1}$ is assigned to the 4_0^2 transition. The 4_0^2 transition assigned in the matrix at $12\,532 \text{ cm}^{-1}$ is reassigned as indicated in Table I.

The origin band of the $B^2\Sigma_u^+ \leftarrow X^2\Pi_g$ transition was recorded using 0.15 cm^{-1} resolution. However, only the rotational profile was observed as seen in Fig. 3. The rotational profile can be simulated for a $^2\Sigma \leftarrow ^2\Pi$ transition, using the calculated geometries,¹² which corresponds to $B''=0.156$ and $B'=0.161 \text{ cm}^{-1}$. One obtains two peaks separated by $\sim 3 \text{ cm}^{-1}$ such as the first two bands in the experimental spectrum; however, four peaks are observed. Because the ions have been cooled to $\sim 20\text{--}30 \text{ K}$, as has been shown also in measurements of other ions,¹⁸ all the transitions originate from the lowest vibrational level of the $X^2\Pi_g$ state and thus a vibrational sequence transition can be excluded. A possibility for the occurrence of the two additional peaks to the blue (Fig. 3) is that they are due to a transition to the nearby lying $A^2\Sigma_g^+$ state, becoming vibronically allowed. The $A^2\Sigma_g^+$ and $B^2\Sigma_u^+$ origin bands are separated by just $\sim 2000 \text{ cm}^{-1}$.⁹ For a vibronically induced transition to have intensity comparable to a dipole allowed one, strong intensity stealing

would have to occur. Thus, the interpretation of the four peaks is tentative and a definitive interpretation will require the help of high level theoretical calculations because the rotational structure cannot be resolved.

The lifetime characteristics of the $B^2\Sigma_u^+$ excited state were followed by varying the time delay between the excitation and fragmentation laser. The observed decay curve was fitted with a single exponential with a constant of $35 \mu\text{s}$. However, the $B^2\Sigma_u^+$ lifetime as determined from the FWHM ($\sim 10 \text{ cm}^{-1}$) of the 0_0^0 band (Fig. 3) corresponds to a few picoseconds. Thus, the measured $\sim 35 \mu\text{s}$ decay constant arises from the population of another state, quite possibly $A^2\Sigma_g^+$, following picosecond intramolecular vibrational relaxation from the $B^2\Sigma_u^+$ state. The second UV photon is then absorbed from the longer lived $A^2\Sigma_g^+$ state and leads to the CN^+ fragment.

IV. CONCLUSION

Dicyanocationic compounds may occur in the interstellar medium but cannot be probed by radio astronomy. However, the electronic spectra may be a way to observe these species in space and terrestrial environments such as plasmas and flames. The observation of the $B^2\Sigma_u^+ \leftarrow X^2\Pi_{3/2,g}$ transition of NCCN^+ , with an origin band at $11\,253 \text{ cm}^{-1}$, provides an accurate band maximum in the gas phase and allows the frequencies of four fundamentals in the $B^2\Sigma_u^+$ state to be deduced. By using the PFI-PE adiabatic ionization energy to the $X^2\Pi_{3/2,g}$ state (13.3705 eV) (Ref. 9) and the $B^2\Sigma_u^+ \leftarrow X^2\Pi_g$ origin band transition, a more exact value for the adiabatic ionization potential to the $B^2\Sigma_u^+$ excited state of $14.766(1) \text{ eV}$ is obtained. Because of the short $B^2\Sigma_u^+$ state lifetime, a picosecond pump-probe approach may shed insight into the dynamics and fast intramolecular vibrational relaxation.

ACKNOWLEDGMENTS

This work is supported by the Swiss National Science Foundation (200020-115864/1) and is part of the European Union project *Molecular Universe* (MRTN-CT-2004-512303).

- P. Thaddeus and M. C. McCarthy, *Spectrochim. Acta, Part A* **57**, 757 (2001) and references therein.
- E. B. Jochowitz and J. P. Maier, *Annu. Rev. Phys. Chem.* **59**, 519 (2008).
- W. E. Sinclair, D. Pfluger, and J. P. Maier, *J. Chem. Phys.* **111**, 9600 (1999).
- H. Linnartz, D. Pfluger, O. Vaizert, P. Cias, P. Birza, D. Khoroshev, and J. P. Maier, *J. Chem. Phys.* **116**, 924 (2002).
- T. Motylewski, H. Linnartz, O. Vaizert, J. P. Maier, G. A. Galazutdinov, F. A. Musaeov, J. Krelowski, G. A. H. Walker, and D. A. Bohlender, *Astrophys. J.* **531**, 312 (2000).
- V. G. Kunde, A. C. Aikin, R. A. Hanel, D. E. Jennings, W. C. Maguire, and R. E. Samuelson, *Nature (London)* **292**, 686 (1981).
- J. H. J. Waite, D. T. Young, T. E. Cravens, A. J. Coates, F. J. Crary, B. Magee, and J. Westlake, *Science* **316**, 870 (2007).
- C. Baker and D. W. Turner, *Proc. R. Soc. London, Ser. A* **308**, 19 (1968).
- M. Hochlaf, T. Baer, X.-M. Qian, and C. Y. Ng, *J. Chem. Phys.* **123**, 144302 (2005).
- S. Bell, *Chem. Phys. Lett.* **67**, 498 (1979).
- W. v. Niessen, L. S. Cederbaum, J. Schirmer, G. H. F. Dierksen, and W. P. Kraemer, *J. Electron Spectrosc. Relat. Phenom.* **28**, 45 (1982).

- ¹²E. Riaplov, M. Wyss, J. P. Maier, M. Hochlaf, and P. Rosmus, *Int. J. Mass. Spectrom.* **223–224**, 107 (2003).
- ¹³J. Fulara, S. Leutwyler, J. P. Maier, and U. Spittel, *J. Phys. Chem.* **89**, 3190 (1985).
- ¹⁴M. E. Jacox and W. E. Thompson, *J. Chem. Phys.* **126**, 054308 (2007).
- ¹⁵V. B. Dibeler and S. K. Liston, *J. Chem. Phys.* **47**, 4548 (1967).
- ¹⁶A. Dzhonzon, D. Gerlich, E. J. Bieske, and J. P. Maier, *J. Mol. Struct.* **795**, 93 (2006).
- ¹⁷D. Gerlich, *Adv. Chem. Phys.* **82**, 1 (1992).
- ¹⁸A. Dzhonzon, E. B. Jochnowitz, E. Kim, and J. P. Maier, *J. Chem. Phys.* **126**, 044301 (2007).
- ¹⁹T. Shimanouchi, *J. Phys. Chem. Ref. Data* **6**, 993 (1977).

6.6 $D^2\Pi_u, C^2\Pi_u \leftarrow X^2\Pi_g$ *Electronic Transitions*
of $NCCN^+$

$D^2\Pi_u, C^2\Pi_u \leftarrow X^2\Pi_g$ Electronic Transitions of $NCCN^+$

C. A. Rice, V. Rudnev, S. Chakrabarty, and J. P. Maier*

Department of Chemistry, University of Basel, Klingelbergstrasse 80, CH-4056 Basel, Switzerland

Received: July 16, 2009; Revised Manuscript Received: December 15, 2009

The electronic absorption spectrum of $NCCN^+$ in the gas phase was measured at ~ 15 K in a 22-pole ion trap. The spectra show two band systems assigned to the $C^2\Pi_u-X^2\Pi_g$ and $D^2\Pi_u-X^2\Pi_g$ transitions with origin band maxima at 17 363 (3) and 33 409 (5) cm^{-1} , respectively. Both absorptions show distinct vibrational structure with progressions in ν_2 as well as combinations of double quanta excitations in ν_4 and ν_5 . Rotational structure of the 0_0^0 bands could not be resolved, which indicates that the $C^2\Pi_u$ and $D^2\Pi_u$ states have a lifetime on the order of a hundred femtoseconds because of fast intramolecular processes.

1. Introduction

The major molecules that form the atmosphere of Saturn's moon, Titan, are nitrogen and methane.¹ Small traces of saturated and unsaturated hydrocarbons and cyano compounds were also found during the Cassini mission.^{1,2} Cyanogen is formed when nitrogen and acetylene are reacted by an electrical spark or discharge.³ In the outer atmosphere of Titan, sunlight and high energetic particles from Saturn's magnetosphere⁴ cause similar conditions. Cyanogen cation ($NCCN^+$) can be produced from the ionization of the neutral molecule.⁵ The centrosymmetric nature of $NCCN^+$ does not make it accessible to pure-rotational spectroscopy because it lacks a permanent dipole moment; however, its electronic and vibrational spectrum can be observed, making it of astrophysical interest.

In the inner regions of circumstellar envelopes, many neutral species have been observed through radio-astronomy; however, near the outer edges, UV radiation changes the chemistry, and some positive species are prevalent. This is also true in dark molecular clouds where only long wavelengths of light can penetrate. Small cations can be involved in many ion-neutral reactions to form larger molecules, making for a plethora of chemistry in molecular clouds and circumstellar envelopes.

$NCCN^+$ has a $X^2\Pi_{3/2,g}$ ground state with the $\sigma_g^2\sigma_g^2\pi_g^4\pi_g^3$ electronic configuration. Four excited states $A^2\Sigma_g^+$, $B^2\Sigma_g^+$, $C^2\Pi_u$, and $D^2\Pi_u$, have been known from photoelectron spectroscopy^{6,7} and theory.^{8–10} $NCCN^+$ has been investigated by matrix isolation spectroscopy, where its electronic^{10,11} and infrared¹² spectra have been measured. Transitions from the $X^2\Pi_g$ ground state to the $B^2\Sigma_g^+$, $C^2\Pi_u$, and $D^2\Pi_u$ states are dipole allowed. In neon matrices at 5 K,^{10,11} the observed $C^2\Pi_u-X^2\Pi_g$ and $D^2\Pi_u-X^2\Pi_g$ transitions are broadened by site effects and phonon side bands, making a determination of frequencies and assignments of smaller features difficult. The $D^2\Pi_u-X^2\Pi_g$ transition measured in neon matrices was overlapped by the absorption of CNC ($A^2\Delta_u \leftarrow X^2\Pi_g$), causing difficulties in the assignment of individual bands.¹⁰

Photoelectron⁶ and photoionization¹³ spectra of cyanogen are quite broad; however, well-resolved band systems have been observed by a pulsed-field ionization photoelectron (PFI-PE) measurement⁷ using a molecular beam and synchrotron radiation, although the resolution was still limited to ~ 12 cm^{-1} . In the PFI-PE study, three excited states, $A^2\Sigma_g^+$, $B^2\Sigma_g^+$, $C^2\Pi_u$, have

been recorded; the $D^2\Pi_u$ state has so far only been observed in a neon matrix.¹⁰ The most accurate study of the $B^2\Sigma_g^+$ excited state to date has been via its $B^2\Sigma_g^+-X^2\Pi_g$ transition using cryogenic ion-trapping technology and a 0.3 cm^{-1} resolution laser.¹⁴ The 0_0^0 band could still not be rotationally resolved due to fast intramolecular relaxation resulting in a picosecond lifetime. In the present work, the $C^2\Pi_u-X^2\Pi_g$ and $D^2\Pi_u-X^2\Pi_g$ electronic transitions of mass-selected $NCCN^+$ have been recorded in absorption at ~ 20 K in the gas phase and at a resolution of approximately 5 cm^{-1} . The width of the bands in the observed transitions is limited by lifetime broadening of the excited states. The method used a 22-pole trap to confine and collisionally cool the cyanogen cations to ~ 20 K prior to the measurement of the absorption of laser radiation using a resonant one-color, two-photon dissociation approach.

2. Method

The cyanogen cations were created using electron impact (15 eV) of the neutral molecular gas. The apparatus employed was described previously.¹⁴ The experiment incorporates a magnetic bender, which separates cations and neutrals after they exit the source from a 0.5 mm pinhole. The bender also serves as a kinetic energy selector from the wide energy distribution of an electron impact source. The ions were passed into a hexapole, subsequently mass-selected by a quadrupole filter and then injected into a 36 mm long 22-pole ion trap, based on the design given in ref 15. The mass resolution was set to ± 2.5 u. The trap was filled with approximately 3000 ions in 20 ms. There the ions undergo collisions with cryogenically cooled helium gas (ca. 8 K) for 60 ms, thermalizing their rotational and vibrational degrees of freedom.

The ions were probed using a one-color, two-photon technique. In this the ions were first excited by one photon from a tunable optical parametric oscillator (OPO) laser and subsequently fragmented by a second photon. The laser beam was directed through the center of the trap. After resonance excitation, the dissociation products were released from the ion trap by lowering the exit potential. A second quadrupole mass filter analyzes and detects fragment ions. The $C^2\Pi_u-X^2\Pi_g$ and $D^2\Pi_u-X^2\Pi_g$ transitions were obtained by monitoring CN^+ and C_2^+ mass channels as a function of photon energy. The power curve of the OPO laser was fitted to a higher order polynomial, and the intensities of the recorded absorption features are scaled accordingly. The laser bandwidth was 5 cm^{-1} within the visible

* Corresponding author. E-mail: j.p.maier@unibas.ch.

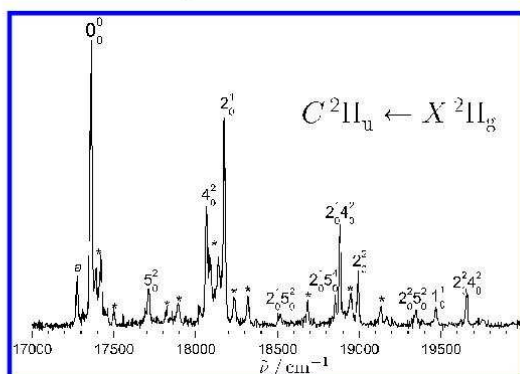


Figure 1. The origin band and assigned vibrational excitations within the C²Π_u–X²Π_g transition of NCCN⁺.

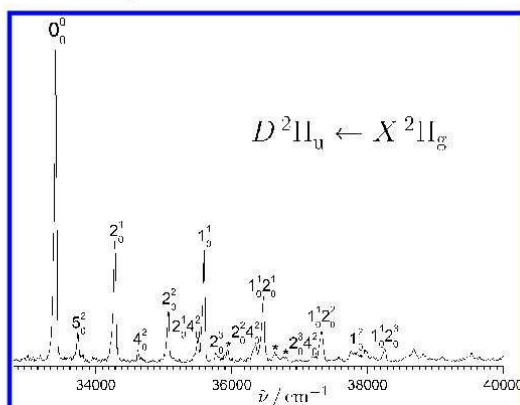


Figure 2. The electronic spectrum of the D²Π_u–X²Π_g transition of NCCN⁺ with the assignments of vibrational excitations.

region, while in the UV it was 8 cm⁻¹. The 0₀⁰ band of the C²Π_u–X²Π_g transition was also recorded with a 0.15 cm⁻¹ bandwidth dye laser, without resolving the rotational structure further.

3. Results and Discussion

The absorption spectra are the C²Π_u–X²Π_g and D²Π_u–X²Π_g transitions of NCCN⁺ presented in Figures 1 and 2. Because the temperature of the ion is ca. 15 K, the population of the Ω = 1/2 spin-orbit component in the ground state is negligible as A_{so} = -57.2 cm⁻¹;⁷ therefore, all photoinduced excitations occur from Ω = 3/2, and ΔΩ = 0 transitions (Hund's case a) are observed. Both C²Π_u and D²Π_u excited states are Renner–Teller active, resulting in a complex pattern.

Using the PFI-PE⁷ and photoionization¹³ data, the photofragmentation dynamics in NCCN⁺ are deduced. The lowest thermodynamic process is NCCN⁺ + hν → C₂⁺ + N₂ (4.09 ± 0.02 eV), and there is also an energetically higher fragmentation channel, NCCN⁺ + hν → CN⁺ + CN (7.05 ± 0.02 eV). In the N₂ loss pathway, the energy required for dissociation is slightly below the D²Π_u–X²Π_g transition of NCCN⁺; however, sequential absorption of two photons from the laser radiation in the C²Π_u–X²Π_g system is energetically sufficient to produce fragmentation products.

3.1. C²Π_u–X²Π_g Transition. The C²Π_u–X²Π_g transition arises from the excitation of a bonding π_u electron to the π_g

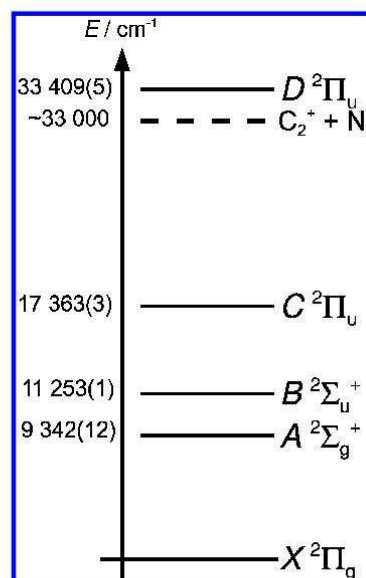


Figure 3. Energy level diagram of NCCN⁺ giving the ν = 0 levels of the states inferred from the electronic transition (B,¹⁴ C, and D) and from the PFI-PE study (A).⁷ Thermodynamic threshold is at ~33 000 cm⁻¹.

(HOMO) orbital, giving a σ_g²σ_g²π_u²π_g⁴ electronic configuration. The most intense peak farthest to the red at 17 363 ± 3 cm⁻¹ is the origin band (Figure 1). This is outside the error limit of the PFI-PE value of 17 393 ± 12 cm⁻¹.⁷ There is a small absorption feature at 17 276 cm⁻¹ (a in Figure 1) to the red of the 0₀⁰ band, which is most probably due to a symmetry-allowed transition to the vibrational manifold in the B²Σ_u⁺ state. In the absorption spectrum in a 5 K neon matrix, a band red-shifted by ~100 cm⁻¹ from the 0₀⁰ origin transition is also observed,¹¹ thus excluding the possibility that the peak a is a hot band. In the PFI-PE data, it is wrongly assigned to the C²Π_{(3/2),u}–X²Π_{3/2,g} transition, and, in the same study,⁷ the doublet structure was assumed to be a vibrational progression in ν₂ (C–C stretch) of the C²Π_u state caused by the spin-orbit components, Ω' = 1/2 and 3/2. The origin bands of the B²Σ_u⁺–X²Π_g and C²Π_u–X²Π_g systems are separated by ~6000 cm⁻¹ (Figure 3), making vibronic coupling probable for the absorption band a in Figure 1. This is similar to that in the B²Σ_u⁺–X²Π_g transition, where the B²Σ_u⁺ excited-state lifetime is on the order of picoseconds,¹⁴ presumably due to internal conversion to the nearby A²Σ_g⁺ (Figure 3).

The next most intense peak in the C²Π_u–X²Π_g system is the 2₀¹ transition at 18 174 cm⁻¹. This corresponds to a vibrational frequency of 811 ± 3 cm⁻¹ for the ν₂ C–C stretch in the C²Π_u state (Table 1). This differs significantly from the neon matrix value of 740 ± 10 cm⁻¹,¹¹ whereas in the PFI-PE a tentative assignment of 788 ± 10 cm⁻¹ was made.⁷ If the assignment of the transitions 2₀¹ and 4₀² in the neon matrix spectrum is interchanged, ν'₂ = 844 ± 10 cm⁻¹ is obtained, although still outside the error limits with the ν'₂ inferred here.

The two peaks to the red of the 2₀¹ transition are assigned to double excitations in ν₄ and ν₅ (bending modes); 4₀² is centered around 18 065 cm⁻¹ and 5₀² at 17 710 cm⁻¹. From these frequencies, ν'₄ = 351 cm⁻¹ and ν'₅ = 173.5 cm⁻¹ are inferred.

TABLE 1: Band Maxima (± 3 cm⁻¹) Observed in the C²Π_u-X²Π_g Transition of NCCN⁺ and the Assignments Made

assignment	$\bar{\nu}/\text{cm}^{-1}$	$\Delta\bar{\nu}/\text{cm}^{-1}$	assignment	$\bar{\nu}/\text{cm}^{-1}$	$\Delta\bar{\nu}/\text{cm}^{-1}$
<i>a</i>	17 276			18 236	
0 ₀ ⁺	17 363			18 320	
	17 390		2 ₀ 5 ₀ ⁺	18 517	1154
	17 423			18 683	
	17 500		2 ₀ 5 ₀ ⁺	18 852	1489
5 ₀ ⁺	17 710	347	2 ₀ 4 ₀ ⁺	18 884	1521
	17 821			18 948	
	17 891		2 ₀ ⁺	18 995	1632
	18 026			19 137	
4 ₀ ⁺	18 065	702	2 ₀ 5 ₀ ⁺	19 344	1981
	18 085		1 ₀ ⁺	19 468	2105
	18 140		2 ₀ 4 ₀ ⁺	19 659	2296
2 ₀ ⁺	18 174	811			

TABLE 2: Experimentally Determined Vibrational Frequencies (in cm⁻¹)

	NCCN ⁺					
	X ¹ Σ _g ⁺	X ² Π _g ^b	A ² Σ _g ⁺ ^b	B ² Σ _u ⁺ ^c	C ² Π _u ^d	D ² Π _u ^d
ν_1	2330(3)	2262(10)	1860(40)	2287(1)	2105(3)	2188(5)
ν_2	846(6)	956(10)	838(10)	1066(1)	811(3)	870(5)
ν_3	2158(1)	1818(20)				
ν_4	503(6)			390 ^e	351 ^e	607 ^e
ν_5	234(3)		277 ^e	273 ^e	174 ^e	164 ^e

^aReference 16. ^bReference 7. ^cReference 14. ^dThis work. ^eObtained from double quanta excitations. Calculated¹⁰ X²Π_g state frequencies are: ν_1 (σ_g^+ : C≡N sym. str.) = 2300, ν_2 (σ_g^+ : C-C str.) = 808, ν_3 (σ_g^+ : C≡N asym. str.) = 1789, ν_4 (π_g^- : deform.) = 537, and ν_5 (π_u^- : deform.) = 240.

Using the interchanged values of 4₀⁺ and 2₀⁺ bands in the neon matrix, ν_4 of ~ 370 cm⁻¹ is obtained. There is also a progression in 2₀⁺4₀⁺ and 2₀⁺5₀⁺, where $\nu' = 1$ and 2 (Figure 1). The 1₀⁺ (C≡N symmetric stretch) can be clearly associated with the 19 468 cm⁻¹ absorption peak, $\nu'_1 = 2105$ cm⁻¹ thus changing only by 7% from that of the ground state of NCCN⁺ (Table 2). Several weaker bands within the electronic spectrum, marked as “*”, are apparently due to the complicated nature of this Renner-Teller state. These weak transitions are artificially enhanced by the power of the laser used in the two-photon experiment. An assignment of these features will require a high-level ab initio treatment.

3.2. D²Π_u-X²Π_g Transition. In the D²Π_u-X²Π_g transition, electronic excitation occurs from the π_g (HOMO) to the π_u (LUMO) orbital with the $\sigma_u^2\sigma_g^2\pi_u^2\pi_g^2\pi_u^1$ electronic configuration dominating the D²Π_u state. The strongest peak to the red at 33 409 cm⁻¹ is the origin band of the $\Omega' = \Omega'' = 3/2$ spin-orbit component (Figure 2). In the absorption spectrum in a 5 K neon matrix,¹⁰ the 0₀⁺ band is at 33 522 ± 5 cm⁻¹, blue-shifted by ~ 110 cm⁻¹ relative to the gas phase. The origin band in the gas phase has a full-width half-maximum of ~ 30 cm⁻¹, which is broadened due to a fast internal process and/or predissociation as the fragmentation threshold for the dissociative product formation is exceeded.

The next two strongest features present in the D²Π_u-X²Π_g system are assigned to the 2₀⁺ (C-C stretch) and the 1₀⁺ (C≡N symmetric stretch) transitions, which are located at 34 279 and 35 597 cm⁻¹ (Table 3). There is a clear vibrational progression in ν_2 , where $\nu' = 1, 2,$ and 3 are observed (Figure 2). Treating this as a diatomic vibration, one obtains ω_e and $\omega_e x_e$ in the D²Π_u excited state to be 952 ± 5 and 42 ± 3 cm⁻¹, respectively. In the gas-phase spectrum, there are two weak bands to the red and blue of the 2₀⁺ transition, which have been tentatively

TABLE 3: Vibrational Band Maxima (± 5 cm⁻¹) Observed in the D²Π_u-X²Π_g Transition of NCCN⁺ and the Suggested Assignments

assignment	$\bar{\nu}/\text{cm}^{-1}$	$\Delta\bar{\nu}/\text{cm}^{-1}$
0 ₀ ⁺	33 409	
5 ₀ ⁺	33 736	327
2 ₀ ⁺	34 279	870
4 ₀ ⁺	34 623	1214
2 ₀ ⁺	35 060	1651
2 ₀ 4 ₀ ⁺	35 496	2087
1 ₀ ⁺	35 597	2188
2 ₀ ⁺	35 762	2353
	35 929	2520
2 ₀ 4 ₀ ⁺	36 334	2925
1 ₀ 2 ₀ ⁺	36 466	3057
	36 627	3218
	36 788	3379
2 ₀ 4 ₀ ⁺	37 212	3803
1 ₀ 2 ₀ ⁺	37 324	3915
1 ₀ ⁺	37 832 ^a	4423
1 ₀ 2 ₀ ⁺	38 251	4842

^a ±50 cm⁻¹.

attributed to the 5₀⁺ (33 736 cm⁻¹) and 4₀⁺ (34 623 cm⁻¹) vibrational excitations. The present data show that the assignment of the 5₀⁺ and 4₀⁺ bands in a neon matrix is not correct.¹⁰ In the latter, the system is overlapped by the A²Δ_u ← X²Π_g transition of CNC. Therefore, the gas-phase values are the reliable ones: $\nu'_4 = 607$ (5) cm⁻¹ and $\nu'_5 = 164$ (5) cm⁻¹. In Table 2 are collected the best values for the vibrational modes with error limits determined for the cation in its different electronic states by different techniques. There are also two combination progressions in the gas-phase spectrum (Figure 2), one with 2₀⁺4₀⁺ and the other in 1₀⁺2₀⁺, where $\nu' = 1, 2,$ and 3.

4. Conclusions

The centrosymmetric cyanogen and its cation occur in the interstellar medium or terrestrial environments; however, they cannot be probed by mm-wave spectroscopy. The presently measured gas-phase electronic transitions provide the means of identifying the cation spectroscopically in such inaccessible media. The C²Π_u-X²Π_g and D²Π_u-X²Π_g absorption spectra of NCCN⁺ in the gas phase have been observed with 0₀⁺ bands at 575.9 and 299.3 nm, respectively. The absorption features yield the vibrational frequencies of several of the fundamental modes in the excited states. Because of the short lifetimes in the C²Π_u and D²Π_u excited states, the 0₀⁺ bands could not be rotationally resolved; the bandwidths imply lifetimes of a hundred femtoseconds. The short lifetimes are attributed to fast intramolecular processes, made feasible due to the presence of several low-lying excited electronic states.

Acknowledgment. This work is supported by the Swiss National Science Foundation (Project No. 200020-124349/1).

References and Notes

- (1) Waite, J. H., Jr.; Niemann, H.; Yelle, R. V.; Kasprzak, W. T.; Cravens, T. E.; Lüthmann, J. G.; McNutt, R. L.; Ip, W.-H.; Gell, D.; De La Haye, V.; Müller-Wordag, I.; Magee, B.; Borggren, N.; Ledvina, S.; Fletcher, G.; Walter, E.; Miller, R.; Scherer, S.; Thorpe, R.; Xu, J.; Block, B.; Arnett, K. *Science* **2005**, *308*, 982.
- (2) Waite, J. H., Jr.; Young, D. T.; Cravens, T. E.; Coates, A. J.; Cray, F. J.; Magee, B.; Westlake, J. *Science* **2007**, *316*, 870.
- (3) Strutt, R. J. *Proc. R. Soc. London, Ser. A* **1911**, *85*, 219.
- (4) Sagan, C.; Thompson, W. R. *Icarus* **1984**, *59*, 133.
- (5) Bézard, B. *Philos. Trans. R. Soc. London, Ser. A* **2009**, *367*, 683.

- (6) Baker, C.; Turner, D. W. *Proc. R. Soc. London, Ser. A* **1968**, 308, 19.
- (7) Hochlaf, M.; Baer, T.; Qian, X.-M.; Ng, C. Y. *J. Chem. Phys.* **2005**, 123, 144302.
- (8) Bell, S. *Chem. Phys. Lett.* **1979**, 67, 498.
- (9) Niessen, W. v.; Cederbaum, L. S.; Schirmer, J.; Dierksen, G. H. F.; Kraemer, W. P. *J. Electron Spectrosc. Relat. Phenom.* **1982**, 28, 45.
- (10) Riaplov, E.; Wyss, M.; Maier, J. P.; Hochlaf, M.; Rosmus, P. *Int. J. Mass Spectrom.* **2003**, 223, 107.
- (11) Fulara, J.; Leutwyler, S.; Maier, J. P.; Spittel, U. *J. Phys. Chem.* **1985**, 89, 3190.
- (12) Jacox, M. E.; Thompson, W. E. *J. Chem. Phys.* **2007**, 126, 054308.
- (13) Dibeler, V. H.; Liston, S. K. *J. Chem. Phys.* **1967**, 47, 4548.
- (14) Rudnev, V.; Rice, C. A.; Maier, J. P. *J. Chem. Phys.* **2008**, 129, 134315.
- (15) Gerlich, D. *Adv. Chem. Phys.* **1992**, 82, 1.
- (16) Shimanouchi, T. *J. Phys. Chem. Ref. Data* **1977**, 6, 993.

JP906722K

Conclusions

Five origin bands of higher excited states of polyacetylene cations have been observed by resonance two-colour, two-photon photodissociation spectroscopy for the first time in the gas-phase (*Chapter 6.2*). The observed cations have a rotational temperature in the range 15-25 K which allows for a direct comparison between experiment and astrophysical data. Although, no direct matches were found between the experimentally determined origin bands and any known DIBs, some conclusions were made. First, the FWHMs of the origin bands of higher excited states increase. This was illustrated for $C_{10}H_2^+$ cation, where the $A^2\Pi_g$, $B^2\Pi_g$ and $C^2\Pi_g$ states were considered. For $C_8H_2^+$ only two $B^2\Pi_u$ and $C^2\Pi_u$ excited states were measured and compared. The same behaviour was observed: the FWHM of the origin band of $C^2\Pi_u$ excited state is greater than the FWHM of the origin band of $B^2\Pi_u$ state (4 as compared to 8 cm^{-1}). Another conclusion is derived when the FWHMs of the origin bands of the same electronic state are considered for different cations ($HC_{2n}H^+$ $n=4,5$). In case of $C_8H_2^+$ and $C_{10}H_2^+$ the FWHMs of the origin band of the $B^2\Pi_{g/u}$ excited state are $\sim 4\text{ cm}^{-1}$, whereas for the $C^2\Pi_u$ excited state of $C_{10}H_2^+$ the FWHM is greater than in $C_8H_2^+$, 30 and 8 cm^{-1} . Thus, the bandwidth of the transition of the $C^2\Pi_{u/g}$ state increases with increasing number of carbon atoms in the molecule. In contrast, the observed bandwidths for $B^2\Pi_{g/u}$ state are the same and do not change or change slightly with increasing number of carbon atoms. Based on experimental FWHMs of $B^2\Pi_{g/u}$ states, argumentation that only these are DIB relevant was given.

During spectroscopic studies of $C_7H_2^+$ cation in the gas-phase, an unexpected transition was observed at 521 nm (*Chapter 6.3*). The parent ion mass in the experiment was 86 m/z. The origin band was rotationally resolved. Based on the K -structure of the band, it was concluded that a non-linear molecule was responsible for the observed origin band. It was assumed that the diacetylene precursor was contaminated because of the chemical preparation procedure, coming from the precursor of the synthesis. Accordingly, the presence of $C_4H_3Cl^+$ at the same mass 86 m/z was suggested. In order to explain the experimentally obtained data, ground state calculations at b3lyp/(6-311++G(d,p)) level of theory were performed, giving five isomers of C_s symmetry. Using the rotational constants for the ground state, it was possible to fit simulated bands with the experimental one for isomer A and linear isomer. The ${}^2A'-{}^2A'$ and ${}^2A''-{}^2A''$ electronic excitations of a-type rotational transition have matched with the observed 0_0^0 band.

Based on a MO diagram using DFT calculations, the argumentation that only ${}^2A'' \rightarrow {}^2A''$ electronic transition could be observed in the experiment was made.

R2C2PD spectroscopy, which was applied to linear carbon chains, was chosen to probe the electronic transitions of PAH⁺ cations (*Chapter 6.4*). The $D_2({}^2A_u) \leftarrow D_0({}^2B_{2g})$ electronic transition was observed at 708 nm with a FWHM of 5 nm. The conclusion that An⁺ cation is not DIB relevant, was given. The same spectroscopic method was not possible to realize for the Np⁺. Although, the second colour was varied in the wide range of energies 5.9-4.1 eV (210-300 nm) and the two laser pulses were overlapped in time and spatially. However, using multi-photon, one-colour photofragmentation spectroscopy it was possible to obtain the $D_2({}^2B_{3g}) \leftarrow D_0(X {}^2A_u)$ transition of Np⁺ at 672 ± 1.5 nm. The obtained FWHM of the transition was broad ~ 6.5 nm. From the spectra obtained using the REMD technique, it has been observed that there is a disadvantage of resonance multi-photon photofragmentation spectroscopy. The efficiency of this technique is strongly dependent on the laser power and several photons are needed to produce photodissociation channels. The photofragmentation rate for the naphthalene cation is calculated to be 10^3 s^{-1} at 7 eV internal energy and 10^5 s^{-1} at 8 eV for the C₂H₂ loss channel, whereas the critical energy to dissociate the cation is ca. 6.3 eV. In the case of the Np⁺ cation, this leads to the absorption of more than four photons. The absorption of multi-photons and high power leads to saturation of the recorded band. As a result the FWHM is broad and ~ 6.5 nm. Thus, it was concluded that multi-photon resonance photodissociation spectroscopy does not give a natural linewidth of the transition and the obtained data cannot be comparable with astrophysical observations.

Electronic spectra of three dipole-allowed transitions of NCCN⁺ cation are presented with vibrational assignments (*Chapter 6.5, 6.6*). The centrosymmetric cyanogen and its cation occur in the interstellar medium or terrestrial environments; however, they cannot be probed by rotational spectroscopy. The measured gas-phase electronic transitions provide the means of identifying the cation spectroscopically in such inaccessible media. The $B^2\Sigma_u^+ - X^2\Pi_g$, $C^2\Pi_u - X^2\Pi_g$ and $D^2\Pi_u - X^2\Pi_g$ absorption spectra of NCCN⁺ in the gas phase have been observed with 0_0^0 bands at 888.6 , 575.9 and 299.3 nm, respectively. Because of the short lifetimes in the $C^2\Pi_u$ and $D^2\Pi_u$ excited states, the 0_0^0 bands could not be rotationally resolved, implying lifetimes of a hundred femtoseconds, whereas the $B^2\Sigma_u^+$ excited state lifetime is on the order of 10 picoseconds.

Appendix

Time delay generator based on PCI-CTR20HD Card

The PCI-CTR20HD [114] is a high-performance counter/timer board for PCI bus-compatible computers. This board can be used in such applications as data acquisition, system timing, and industrial process control and laser systems. The PCI-CTR20HD board has four 9513-based counter/timer devices. Each 9513 [115] device has five 16-bit independent up-down counters (65,536 counts). An input source, dual count register, load register, hold register, alarm register, output, and gate are associated with each counter. All are selectable via software. The 9513 counter/timer device can be configured with software to perform event counting, pulse and frequency measurements, watchdog timing, alarm comparisons and other input functions. The 9513 counter/timer can generate frequencies with either complex duty cycles or with one-shot and continuous-output modes. Up to five counters can be chained together using software to enable a 32-, 48-, 64-, or 80-bit counter. The internal/external counter source, gate source, and gating functions are software-programmable. The functional block diagram and specification is shown in *Figure A.I*.

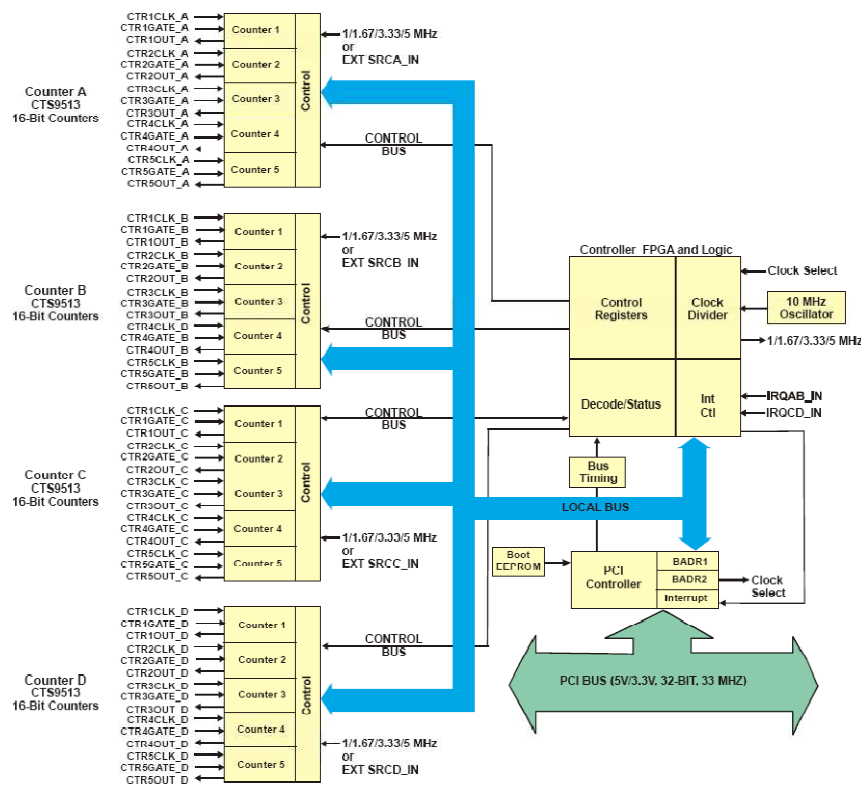


Figure A.I PCI-CTR20HD functional block diagram

The counter specification is shown in *Table A.1*

Parameter	Conditions
Counter type	9513
Configuration	Four 9513 devices. Five up/down counters per 9513, 16-bits each
Compatibility	5V/TTL
Each 9513 device is programmable for:	
Clock source	Software selectable: External: Counter 1-5 clock inputs Counters 1-5 gate inputs Internal: Terminal count of previous counter X2 clock frequency scyler
Gate	Software slectable source: External: Active high or low level or edge, counter 1-5 gates input Active high level previous gate or next gate All externall gate signals (CTR _x GAT _{EN}) individually pulled up through 10 K resistors to +5V. Internal: Active high previous counter terminal count No gating
Output	Software selectable: Always low High puls on terminal count Low pulse on terminal count Toggle on terminal count Inactive, high impedance at user connector # output
OscOut	Software selectable source: Counter #1-5 input Gate #1-5 input Prescaled clock source (X2 clock frequency scaler) Software selectable divider: Division by 1-16 Software selectable enable: On or low impedance to ground
Clock input frequency	6.8 MHz max (145 nS min period)
X2 clock input sources	Software selectable: (each counter individually) External (max = 7.0 MHz) EXT SRCA_IN, EXT_SRCB_IN, EXT SRCC_IN, EXT SRCD_IN 1.0 MHz (10 MHz Xtal divided by 10) 5.0 MHz (10 MHz Xtal divided by 2) 3.33 MHz (33 MHz PCI clock divided by 10) 1.67 MHz (33 MHz PCI clock divided by 20)
X2 clock frequency scaler	BCD scaling (X2 divided by 10,100,1000 or 1000) or Binary scaling (X2 divided by 16, 256,4096 or 65536)
High pulse width	70 ns min

(clock input)	
Low pulse width (clock input)	70 ns min
Gate with high	145 ns min
Gate width low	145 ns min
Input low voltage	-0.5 V min, 0.8 V max
Input high voltage	2.2 V min, Vcc max
Output low voltage @ IIL = 3.2 mA	0.4 V max
Output high voltage @ IIH = -200 μA	2.4 V min
Cristall oscillator frequency	10 MHz
Frequency accuracy	50 pm

Table A.I. Counter specification

For the programmable delay line generator based on a PCI-CTR 20HD card the physical connections of some pins had to be done as shown in *Figure A.II*. Channels CH1- CH10 are output channels of the delay line. The acronym EXT means an input for a trigger signal.

Delay line

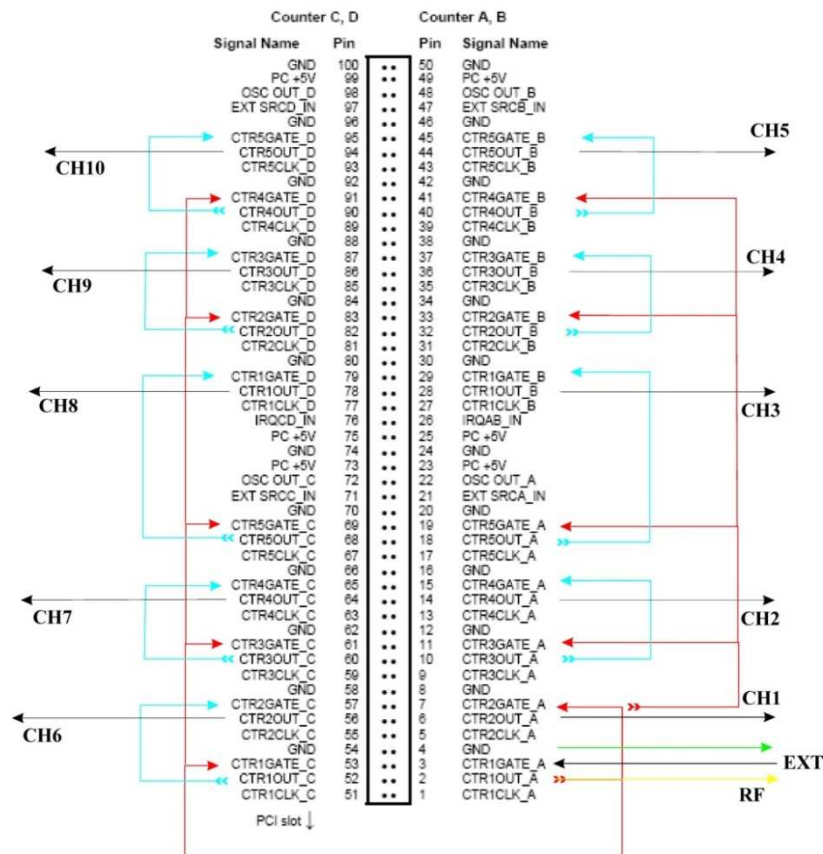


Figure A.II. The physical connection for the PCI-CTR 20HD card

The program was written in LabView. The front panel consists from three tabs. The first tab is used for the configuration purposes. The card can be triggered externally or internally (*Figure A.III*). When the card is triggered externally, one can choose the frequency. For each channel it is possible to choose delay time and pulse width (*Figure A.IV*).

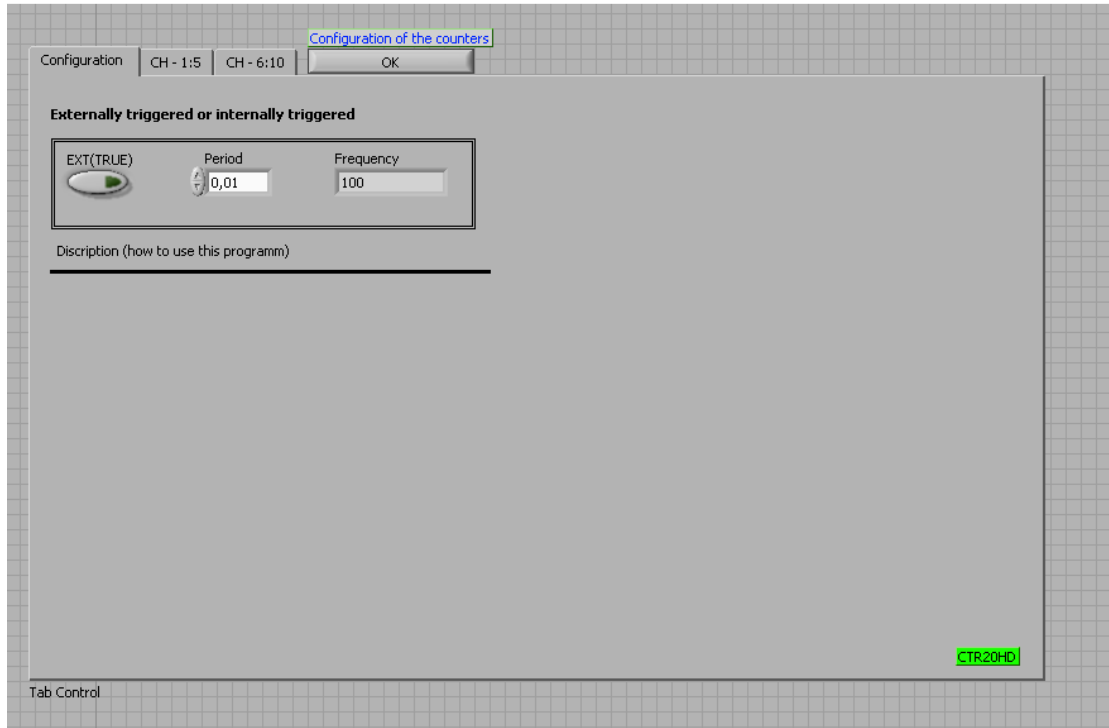


Figure A.III. Front panel of the program.

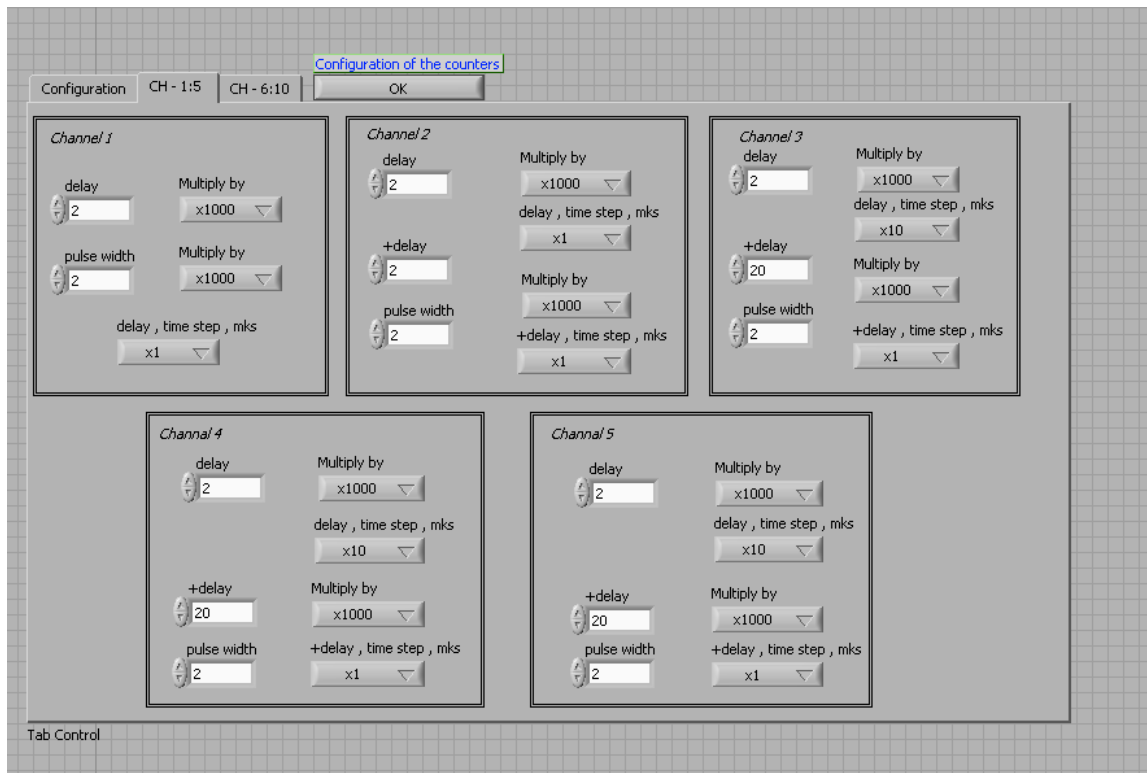


Figure A.IV. Configuration panel of the program.

Bibliography

1. H. Karttunen, P. Kroger, H. Oja, M. Poutanen, and K. J. Donner. *Fundamental Astronomy*. 5 ed. 2007, Berlin: Springer Verlag.
2. George F. R. Ellis- *Issues in the Philosophy of Cosmology*. Handbook in Philosophy of Physics, 2006, Elsevier.
3. B. Feuerbacher, and R. Scranton. *Evidence for the Big Bang*. Available from: [http://www.talkorigins.org/faqs/astronomy/bigbang.html#evidence]
4. F. Cain. *Star Classification*. Available from: [http://www.universetoday.com/guide-to-space/stars/star-classification/]
5. *Harvard classification system*. Available from: [http://www.britannica.com/EBchecked/topic/256286/Harvard-classification-system]
6. M. L. Heger. *Further study of the sodium lines in class B stars; The spectra of certain class B stars in the regions 5630A-6680A and 3280A-3380A; Note on the spectrum of γ Cassiopeiae between 5860A and 6600A*. 141-148. Lick Observatory bulletin, 1922, **337**:141-148.
7. P. W. Merrill. *Unidentified interstellar lines*. Publ. Astron. Soc. Pac., 1934. **46**.
8. G. H. Herbig. *The Diffuse Interstellar Bands*. Annu. Rev. Astron. Astrophys., 1995. **33**(1): 19-73.
9. J. Krelowski. *Diffuse interstellar bands - an observational review (Review)*. Astron. Nachr., 1989. **310**: 255-263.
10. S. Y. Tuairisg, J. Cami, B. H. Foing, P. Sonnentrucker, and P. Ehrenfreund. *A deep echelle survey and new analysis of diffuse interstellar bands*. Astron. Astrophys. Suppl. Ser., 2000. **142**(2): 225-238.
11. P. Jenniskens. *Diffuse Interstellar Bands*. Available from: [http://leonid.arc.nasa.gov/pjenniskens.html]
12. F. Y. Xiang, Sh. Liang, and A. Li. *Diffuse interstellar absorption bands*. Sci. China. Phys. Mech. Astron., 2009. **52**(4): 489-501.
13. A. McKellar, H. L. Welsh, and F. C. Stephenson. *The spectrum of solid oxygen a few degrees above absolute zero*. Astron. J., 1955. **60**: 170-171.
14. B. Vandenbussche, P. Ehrenfreund, A. C. Boogert, E. F. van Dishoeck, W. A. Schutte, P. A. Gerakines, J. Chiar, A. G. G. M. Tielens, J. Keane, D. C. B. Whittet, M. Breitfellner,

- and M. Burgdorf. *Constraints on the abundance of solid O₂ in dense clouds from ISO-SWS and ground-based observations*. *Astron. Astrophys.*, 1999. **346**: L57-L60.
15. N. C. Wickramasinghe. *Origin of the Diffuse Interstellar Bands*. *Nature*, 1968. **217**(5127): 412-415.
 16. H. C. Hulst. *Evolution and physics of solid particles*. Centennica Symposia (Harvard Observatory Monographs), 1948. **7**.
 17. W. W. Duley. *Vibronic origin for the diffuse band spectrum*. *Astrophys. Space Sci.*, 1983. **95**(1): p. 213-214.
 18. A. E. Douglas. *Origin of diffuse interstellar lines*. *Nature*, 1977. 269(5624): 130-132.
 19. G. F. Mitchell, and W. T. Huntress. *Long chain carbon molecules and diffuse interstellar lines*. *Nature*, 1979. **278**(5706): 722-723.
 20. J. Fulara, D. Lessen, P. Freivogel, and J. P. Maier. *Laboratory evidence for highly unsaturated hydrocarbons as carriers of some of the diffuse interstellar bands*. *Nature*, 1993. **366**(6454): 439-441.
 21. P. Freivogel, J. Fulara, D. Lessen, D. Forney, and J. P. Maier. *Absorption spectra of conjugated hydrocarbon cation chains in neon matrices*. *Chem. Phys.*, 1994. **189**(2): 335-341.
 22. F. Salama. *Molecular spectroscopy in astrophysics: the case of polycyclic aromatic hydrocarbons*. *J. Mol. Struct.*, 2001. **563-564**: 19-26.
 23. D. M. Hudgins, and L. J. Allamandola. *Steps toward Identifying PAHs: A Summary of Some Recent Results*. *Proc. Int. Astron. Union*, 2005. **1**(Symposium S231): 443-454.
 24. S. Iglesias-Groth. *Fullerenes as carriers of extinction, diffuse interstellar bands and anomalous microwave emission*. *Proc. Int. Astron. Union*, 2008. **4**(Symposium S251): 57-62.
 25. P. Ehrenfreund, and B. H. Foing. *Search for fullerenes and PAHs in the diffuse interstellar medium*. *Planet. Space Sci.*, **43**(10-11): 1183-1187.
 26. G. Herzberg. *Laboratory Studies of the Spectra of Interstellar Molecules*. *Highlights of Astronomy*, 1971. **2**: 415-520.
 27. P. P. Sorokin, and J. H. Glowina. *Nonlinear spectroscopy in astronomy: assignment of diffuse interstellar absorption bands to L(α) -induced, two-photon absorption by H₂ molecules*. *Chem. Phys. Lett.*, 1995. **234**(1-3): 1-6.
 28. L. Holmlid. *The diffuse interstellar band carriers in interstellar space: all intense bands calculated from He doubly excited states embedded in Rydberg Matter*. *MNRAS*, 2008. **384**: 764-774.

29. T. P. Snow. *Comments on two-photon absorption by H₂ molecules as a source of diffuse interstellar bands*. Chem. Phys. Lett., 1995. **245**(6): p. 639-642.
30. Laser-induced fluorescence. Available from:
[http://en.wikipedia.org/wiki/Laser-induced_fluorescence].
31. P. Zalicki, and R. N. Zare. *Cavity ring-down spectroscopy for quantitative absorption measurements*. J. Chem. Phys., 1995. **102**(7): 2708-2717.
32. D. Rolland, A. A. Specht, M. W. Blades, and J. W. Hepburn. *Resonance enhanced multiphoton dissociation of polycyclic aromatic hydrocarbons cations in an RF ion trap*. Chem. Phys. Lett., 2003. **373**(3-4): 292-298.
33. A. Dzhonson, D. Gerlich, E. J. Bieske, and J. P. Maier. *Apparatus for the study of electronic spectra of collisionally cooled cations: para-dichlorobenzene*. J. Mol. Struct., 2006. **795**(1-3): 93-97.
34. A. Dzhonson, E. B. Jochnowitz, E. Kim, and J. P. Maier. *Electronic absorption spectra of the protonated polyacetylenes HC_{2n}H₂⁺ (n = 3,4) in the gas phase*. J. Chem. Phys., 2007. **126**(4): 044301-5.
35. A. Dzhonson, E. B. Jochnowitz, and J. P. Maier. *Electronic Gas-Phase Spectra of Larger Polyacetylene Cations*. J. Phys. Chem. A, 2007. **111**(10): 1887-1890.
36. W. Paul. *Electromagnetic traps for charged and neutral particles*. Rev. Mod. Phys., 1990. **62**: 531.
37. H. Dehmelt. *Experiments with an isolated subatomic particle at rest*. Rev. Mod. Phys., 1990. **62**: 525.
38. Royal Swedish Academy of Sciences, P.R. 12 October 1989. 5.
39. P. H. Dawson. *Quadrupole mass spectrometry and its applications*. American Vacuum Society classics, 1995. New York: American Institute of Physics.
40. K. A. G. MacN. *Quadrupole mass spectrometry and its applications*. J. Mol. Struct., 1977. **42**: 277-278.
41. E. Raymond , J. F. T. March. *Quadrupole Ion Trap Mass Spectrometry*, ed. 2. 2005: Wiley-Interscience 392.
42. P. E. Kelley, G. C. Stafford, and D. R. Stephens. U.S. Patent 4 540 884, 10 September 1985
43. O. Asvany, and S. Schlemmer. *Numerical simulations of kinetic ion temperature in a cryogenic linear multipole trap*. Int. J. Mass spectrom., 2009. **279**(2-3): 147-155.
44. D. Gerlich. *Inhomogeneous RF Fields: A Versatile Tool for the Study of Processes with Slow Ions*, in Adv. Chem. Phys., 2007.

45. J. Mikosch. *Dynamics of anion-molecule reactions at low energy*. 2007, University of Freiburg: Freiburg.
46. J. Mikosch, H. Kreckel, R. Wester, R. Plasil, J. Glosik, D. Gerlich, D. Schwalm, and A. Wolf. *Action spectroscopy and temperature diagnostics of H_3^+ by chemical probing*. J. Chem. Phys., 2004. **121**(22): 11030-11037.
47. R. Otto, J. Mikosch, S. Trippel, M. Weidemuller, and R. Wester. *Nonstandard Behavior of a Negative Ion Reaction at Very Low Temperatures*. Phys. Rev. Lett., 2008. **101**(6): 063201.
48. O. V. Boyarkin, S. R. Mercier, A. Kamariotis, and T. R. Rizzo. *Electronic Spectroscopy of Cold, Protonated Tryptophan and Tyrosine*. J. Am. Chem. Soc., 2006. **128**(9): 2816-2817.
49. V. Rudnev, C. A. Rice, and J. P. Maier. $B^2\Sigma_u^+ \leftarrow X^2\Pi_g$ electronic spectrum of $NCCN^+$ in the gas phase. J. Chem. Phys., 2008. **129**(13): 134315-4.
50. I. Savic, and D. Gerlich. *Temperature variable ion trap studies of $C_3H_n^+$ with H_2 and HD* . PCCP, 2005. **7**(5): 1026-1035.
51. Y. S. Wang, C. H. Tsai, Y. T. Lee, H. C. Chang, J. C. Jiang, O. Asvany, S. Schlemmer, and D. Gerlich. *Investigations of Protonated and Deprotonated Water Clusters Using a Low-Temperature 22-Pole Ion Trap*. J. Chem. Phys.A., 2003. **107**(21): 4217-4225.
52. M. H. Friedman, A. L. Yergey, and J. E. Campana. *Fundamentals of ion motion in electric radio-frequency multipole fields*. J. Phys. E: Sci. Instrum., 1982. **15**(1): 53-56.
53. R. E. March. *An Introduction to Quadrupole Ion Trap Mass Spectrometry*. J. Mass Spectrom., 1997. **32**(4): 351-369.
54. P. H. Dawson, and N. R. Whetten. *Dynamic Mass Spectrometry* D. Price, Editor. 1971.
55. C. Hügg, and I. Szabo. *New ion-optical devices utilizing oscillatory electric fields. III. Stability of ion motion in a two-dimensional octopole field*. Int. J. Mass Spectrom. Ion Processes, 1986. **73**(3): 277-294.
56. D. B. Gordon, and M. D. Woods. *Certain theoretical aspects of ion trajectories in multipole systems*. Int. J. Mass Spectrom. Ion Processes, 1995. **148**(1-2): 31-44.
57. I. E. Dayton, F. C. Shoemaker, and R. F. Mozley. *The Measurement of Two-Dimensional Fields. Part II: Study of a Quadrupole Magnet*. Rev. Sci. Instrum., 1954. **25**(5): 485-489.
58. D. J. C. G. Vega. *Theory and numerical analysis of the Mathieu functions*. 2003, México.
59. F. A. Londry, R. L. Alfred, and R. E. March. *Computer simulation of single-ion trajectories in Paul-type ion traps*. J. Am. Soc. Mass. Spectrom., 1993. **4**: 687-705.
60. MatLab, MathWorks, Editor. 2008. numerical computing environment.
61. R. B. Moore. *Buffer gas cooling of ion beams*. 2002, CERN-EP.

62. J. Mikosch. *Dynamics of anion-molecule reactions at low energy*, Physics Department. 2007, University of Freiburg: Freiburg.
63. D. Manura. *Additional Notes on the SIMION HS1 Collision Model*. 2007, Scientific Instrument Services.
64. Y. Y. Lee, W. W. Lee, O. Cha-Hwan, and K. Pill-Soo. *Ion Trap Mass Spectrometer Simulation for Multi-Ions Based on an Exact Expression for the Collision Probability*. JKPC, 2001. **39**: 902-906.
65. L. D. Landau, and E. M. Lifshits. *Mechanics*. 1996, Oxford: Butterworth-Heinemann.
66. A. D. Appelhans, and E. M. Dahl. *SIMION ion optics simulations at atmospheric pressure*. Int. J. Mass spectrom., 2005. **244**(1): 1-14.
67. L. M. Matz, H. H. Hill, B. W. Luther, and I. Kanik. *Investigation of drift gas selectivity in high resolution ion mobility spectrometry with mass spectrometry detection*. J. Am. Soc. Mass. Spectrom., 2002. **13**(4): 300-307.
68. G. A. Eiceman, and Z. Karpas. *Ion mobility spectrometry*. 2005, Boca Raton: CRC Press.
69. A. B. Kanu, P. Dwivedi, M. Tam, L. Matz, and H. H. Hill. *Ion mobility-mass spectrometry*. J. Mass Spectrom., 2008. **43**(1): 1-22.
70. G. Kaur-Atwal, G. O'Connor, A. Aksenov, V. Bocos-Bintintan, P. C. Thomas, and C. Creaser. *Chemical standards for ion mobility spectrometry: a review*. Int. J. Ion Mobility Spectrom., 2009. **12**(1): 1-14.
71. G. Yuzhu, Y. Ling, B. A. Thomson, and K. W. Michael Siu. *Combined Ion-Mobility and Mass-Spectrometry Investigations of Metallothionein Complexes Using a Tandem Mass Spectrometer with a Segmented Second Quadrupole*, J. Am. Soc. Mass. Spectrom., 2005. **16**(11): 1787-1794.
72. M. D. Lunney, and R. B. Moore. *Cooling of mass-separated beams using an RFQ ion guide*. Int. J. Mass spectrom., 1999. **190**: 153.
73. C. Illenseer, and H. G. Lohmannsroben. *Investigation of ion-molecule collisions with laser-based ion mobility spectrometry*. PCCP, 2001. **3**(12): 2388-2393.
74. G. Herzberg. *The spectra and structures of simple free radicals; an introduction to molecular spectroscopy*. The George Fisher Baker non-resident lectureship in chemistry at Cornell University. 1971, Ithaca: Cornell University Press.
75. D. C. Harris, and M. D. Bertolucci. *Symmetry and Spectroscopy: An Introduction to Vibrational and Electronic Spectroscopy* 1989: Dover Publications 550.
76. D. Gerlich. *Ion-neutral collisions in a 22-pole trap at very low energies*. Phys. Scr. T., 1995. 59.
77. LabView. 2007, National Instruments. dataflow programming language.

78. A. Dzhonson. *An apparatus for the measurement of the electronic spectra of cold ions in a radio-frequency trap*. 2007, University of Basel: Basel.
79. J. H. Callomon, and F. Creutzberg. *The electronic emission spectrum of ionized nitrous oxide*. Philos. Trans. R. Soc. London, Ser. A, 1974: 157-189.
80. D. Klapstein, R. Kuhn, J. P. Maier, M. Ochsner, and W. Zambach. *Emission and laser excitation spectra of the $\tilde{A}^2\Pi_g \leftrightarrow \tilde{X}^2\Pi_u$ transition of rotationally cooled triacetylene cation*. J. Phys. Chem., 1984. **88**(22): 5176-5180.
81. R. Frey, R. Kakoschke, and E. W. Schlag. *Spectroscopy of molecular ions: Laser-induced fragmentation spectra of N_2O^+ , $A^2\Sigma^+ \leftarrow X^2\Pi$* . Chem. Phys. Lett., 1982. **93**(3): 227-231.
82. M. Larzilliere, and C. Jungen. *Fast ion beam laser spectroscopy of N_2O Effects of orbital angular momentum and vibrational anharmonicity*. Mol. Phys., 1989. **67**(4): 807-837.
83. R. G. Orth, and R. C. Dunbar. *Photodissociation of nitrous oxide cation*. J. Chem. Phys., 1977. **66**(4): 1616-1620.
84. P. Gopher. 2009. Simulates Rotational, Vibrational and Electronic Structure of Spectra.
85. A. L. Betz. *Ethylene in IRC +10216*. ApJL, 1981. **244**: L103-L105.
86. E. B. Jochnowitz, and J. P. Maier. *Electronic Spectroscopy of Carbon Chains*. Annu. Rev. Phys. Chem., 2008. **59**(1): 519-544.
87. P. Cias, O. Vaizert, A. Denisov, J. Mes, H. Linnartz, and J. P. Maier. *Electronic Gas-Phase Spectrum of the Pentaacetylene Cation*. J. Phys. Chem. A, 2002. **106**(42): 9890-9892.
88. J. Lecoultre, J. P. Maier, and M. Rosslein. *Geometric structure of diacetylene cation in the $\tilde{X}^2\Pi_g$ and $\tilde{A}^2\Pi_u$ electronic states*. J. Chem. Phys., 1988. **89**(10): 6081-6085.
89. D. Klapstein, R. Kuhn, J. P. Maier, M. Ochsner, and W. Zambach. *Emission and laser excitation spectra of the $\tilde{A}^2\Pi_g \leftrightarrow \tilde{X}^2\Pi_u$ transition of rotationally cooled triacetylene cation*. J. Phys. Chem., 1984. **88**(22): 5176-5180.
90. W. E. Sinclair, D. Pfluger, H. Linnartz, and J. P. Maier. *Rotationally resolved $\tilde{A}^2\Pi_g \leftarrow \tilde{X}^2\Pi_u$ electronic spectrum of triacetylene cation by frequency modulation absorption spectroscopy*. J. Chem. Phys., 1999. **110**(1): 296-303.
91. D. Pfluger, W. E. Sinclair, H. Linnartz, and J. P. Maier. *Rotationally resolved electronic absorption spectra of triacetylene cation in a supersonic jet*. Chem. Phys. Lett., 1999. **313**(1-2): 171-178.
92. D. Pfluger, T. Motylewski, H. Linnartz, W. E. Sinclair, and J. P. Maier. *Rotationally resolved $A^2\Pi_u \leftarrow X^2\Pi_g$ electronic spectrum of tetraacetylene cation*. Chem. Phys. Lett., 2000. **329**(1-2): 29-35.

93. M. J. S. Dewar, and H. C. Longuet-Higgins. *The Electronic Spectra of Aromatic Molecules I: Benzenoid Hydrocarbons*. Proc. Phys. Soc. London, Sect. A, 1954. 67(9): 795-804.
94. T. Bally, W. Tang, and M. Jungen. *The electronic structure of the radical cations of butadiene, vinylacetylene and diacetylene: similarities and differences*. Chem. Phys. Lett., 1992. 190(5): 453-459.
95. Z. Cao, and S. D. Peyerimhoff. *Electronic spectra of linear isoelectronic species HC_6H^+ , C_6H , HC_5N^+* . PCCP, 2001. 3(8): 1403-1406.
96. N. Komiha, P. Rosmus, and J. P. Maier. *Low lying quartet states in diacetylene, triacetylene and benzene radical cations*. Mol. Phys., 2006. **104**(20): 3281 - 3285.
97. J. Zhang, X. Guo, and Z. Cao. *Electronic spectra of the linear polyynes cations $HC_{2n}H^+$ ($n = 2-8$): An ab initio study*. J. Chem. Phys., 2009. 131(14): 144307.
98. J. Fulara, M. Grutter, and J. P. Maier. *Higher Excited Electronic Transitions of Polyacetylene Cations $HC_{2n}H^+$ $n = 2-7$ in Neon Matrixes*. J. Phys. Chem. A, 2007. **111**(46): 11831-11836.
99. B. Meyer. *Low Temperature Spectroscopy* 1971, New York.
100. M. A. Eljashevich. *Atomic and molecular spectroscopy* 2008, Moskow.
101. M. Allan, E. Kloster-Jensen, and J. P. Maier. *Emission spectra of the radical cations of diacetylene ($\tilde{A}^2\Pi_u \rightarrow \tilde{X}^2\Pi_g$), triacetylene ($\tilde{A}^2\Pi_g \rightarrow \tilde{X}^2\Pi_u$), and tetraacetylene ($\tilde{A}^2\Pi_u \rightarrow \tilde{X}^2\Pi_g, O_o$), and the lifetimes of some vibronic levels of the \tilde{A} states*. Chem. Phys., 1976. **17**(1): 11-18.
102. J. P. Maier, and F. Thommen. *Radiative and nonradiative decay rates of state selected $H - (C \equiv C)_{-2}H^+$, $D - (C \equiv C)_{-2}D^+$, $\tilde{A}^2\Pi_u$ determined by a photoelectron-photon coincidence technique*. J. Chem. Phys., 1980. **73**(11): 5616-5619.
103. Privat communication with Dr. A. Dzhonson.
104. P. Jenniskens, and F. -X. Desert. *A survey of diffuse interstellar bands (3800-8680 A)*. Astron. Astrophys., 1994. **106**: 39-78.
105. N. L. J. Cox, L. Kaper, B. H. Foing, and P. Ehrenfreund. *Diffuse interstellar bands of unprecedented strength in the line of sight towards high-mass X-ray binary 4U 1907+09*. Astron. Astrophys., 2005. **438**(1): 187-199.
106. A. G. G. M. Tielens and T.P. Show. *The diffuse interstellar bands*. 1995. **415**.
107. NIST, Available from:
[<http://webbook.nist.gov/cgi/cbook.cgi?ID=C7439909&Units=SI&Mask=200#Mass-Spec>].

108. O. Sukhorukov, A. Staicu, E. Diegel, G. Rouille, Th. Henning, and F. Huisken. *D₂ - D₀ transition of the anthracene cation observed by cavity ring-down absorption spectroscopy in a supersonic jet*. Chem. Phys. Lett., 2004. **386**(4-6):259-264.
109. H. W. Jochims, E. Ruhl, H. Baumgartel, S. Tobita, and S. Leach. *Size effects on dissociation rates of polycyclic aromatic hydrocarbon cations: Laboratory studies and astrophysical implications*. Astrophys. J., 1994. **420**(1):307-317.
110. Y. Gotkis, M. Oleinikova, M. Naor, and Ch. Lifshitz. *Time-dependent mass spectra and breakdown graphs. 17. Naphthalene and phenanthrene*. J. Phys. Chem., 1993. **97**(47):12282-12290.
111. V. Page, T. P. Snow, and V. M. Bierbaum. *Hydrogenation and Charge States of PAHs in Diffuse Clouds. I. Development of a Model*. Astrophys. J. Suppl. Ser., 2001. **132**(2):233-251.
112. E. R. Micelotta, A. P. Jones, and A. G. Tielens. *PAH processing in a hot gas*. Astron. Astrophys. manuscript no. 11683, 2009.
113. L. Biennier, F. Salama, M. Gupta, and A. O'Keefe. *Multiplex integrated cavity output spectroscopy of cold PAH cations*. Chem. Phys. Lett., 2004. **387**(4-6):287-294.
114. Documentation. *CIO-CTR10HD & CIO-CTR20HD*, Measurement Computing. 2001.
115. Documentation. *CTS9513-2*, Celeritous Technical Services Corp. 2000.

Curriculum Vitae

Personal information:

Name: Vitaly S. Rudnev

Day of birth: 26.01.1980

Place: Lesozavodsk, Russia

Nationality: Russian

Marital status: Single

Education:

1987 – 1997 Primary and secondary school No. 162, Novosibirsk

1997 – 2001 Novosibirsk State University, Physics Department, Novosibirsk, Russia. B.Sc. in Physics.

2001 – 2003 Novosibirsk State University, Physics Department, Novosibirsk, Russia. M.Sc. in physics. Specialization: *Physics of Optical Phenomenons*.

2005 – 2010 University of Basel, Department of Chemistry, Switzerland, Ph.D. work in the group of Prof. John. P. Maier

E-mail: vitaly.rudnev@gmail.com

Professional skills

- Lasers: nanosecond OPO solid state lasers, nanosecond dye lasers, CO₂ laser, picoseconds OPO solid state lasers and solid state continues lasers
- RF devices (radio frequency devices): quadropoles (mass spectrometers), hexapole ion guide , 22 pole trap
- High vacuum systems: membrane pumps, diffusion pumps, turbopumps, vacuum chambers
- Furie spectroscopy, Raman spectroscopy
- IR/UV spectroscopy
- Automation of the experiment, Data processing and analysis
- Numerical calculations